MOLECULAR IMAGING IN NONINVASIVE ASSESSMENT OF DIABETES

PROGRESSION

APPROVED BY SUPERVISORY COMMITTEE

Xiankai Sun, PhD.

Robert Lenkinski, Ph.D.

Orhan K. Oz, M.D. Ph.D.

Ildiko Lingvay, MD.

Jung-Mo Ahn, Ph.D.

DEDICATION

I want to thank my mentor, Dr. Xiankai Sun. I am fortunate to have completed my graduate research under his supervision. He has been with me through every step of this journey and I cannot thank him enough for his patience and inspirations. I would like to thank Dr. Jer-Tsong Hsieh and Dr. Orhan K. Öz for building my critical scientific thinking skills. I also would like to thank my dissertation committee members, Drs. Robert Lenkinski, Ildiko Lingvay and Jung-Mo Ahn, for their advice and encouragement. I would like to thank Mai Lin and Eunice N. Murage for building up the foundation of the project. This research would not have been possible without the help from Koji Sagiyama in Dr. Misaya Takahashi's lab, and Bikash Manandhar in Dr. Jung-Mo Ahn's lab at the University of Texas in Dallas. All of the members of Sun/Öz lab have contributed to make the lab a wonderful place to work.

A number of friends, Hector Perez Montoya, Lorena Espinar, Zhou Gan, Jun Xie, Lilja Kjalarsdóttir, Svavar Sigursteinsson, Patrick Hare, Lien Dang, Jean de Vogüé, Tolga Cagatay, Benjamin Pavie, and Violaine Mottier, have provided immense support and encouragement while making a foreign city like home for me.

Finally, I dedicate this work to my family, Yongyoot Wichaidit, Ubon Wichaidit, Guy Wichaidit, and U-Ging Lo, Chin-Chu Tien and Jem-Mau Lo for their support and encouragement. I am fortunate to have the foundation for all my successes from my parents, Chin-Chu Tien and Jem-Mau Lo. Last, I would like to thank my wife, Chonlarat Wichaidit, for being with me throughout this journey.

MOLECULAR IMAGING IN NONINVASIVE ASSESSMENT OF DIABETES

PROGRESSION

by

SU-TANG LO

DISSERTATION

Presented to the Faculty of the Graduate School of Biomedical Sciences

The University of Texas Southwestern Medical Center at Dallas

In Partial Fulfillment of the Requirements

For the Degree of

DOCTOR OF PHILOSOPHY

The University of Texas Southwestern Medical Center at Dallas

Dallas, Texas

August, 2013

MOLECULAR IMAGING IN NONINVASIVE ASSESSMENT OF DIABETES PROGRESSION

Publication No. _____

SU-TANG LO M.S. B.S.

The University of Texas Southwestern Medical Center at Dallas, 2013

Mentor: XIANKAI SUN Ph.D.

Molecular imaging is a recently emerged multidisciplinary scientific field comprised of diverse technologies. The goal of this branch of science is to understand molecular mechanism of diseases and facilitate drug development, namely the interplay of non-invasive imaging techniques with molecular biology and medicine. The goal of this dissertation is to reflect the roles of molecular imaging in biomedical applications by longitudinal and non-invasive detection of the initiation and progression of diabetes. Diabetes is a chronic disease caused by a gradual loss of pancreatic β-cell mass (BCM). The current clinical diagnosis measures the parameters of the β-cell function (BCF) post the onset of the disease, which cannot accurately reflect the BCM loss during the initiation and progression of the disease. Therefore, a non-invasive imaging technique that enables the direct assessment of BCM change would be highly desirable. In this dissertation, Positron Emission

Tomography (PET) imaging was conducted to non-invasively and longitudinally monitor the change of glucagon-like peptide 1 receptor (GLP-1R), a specific biomarker of pancreatic β-cell, during disease progression. Through a two-fold screening method, a modified bicyclic GLP-1 analog, which enhances biological stability while maintaining the receptor binding affinity, was selected. An imaging probe was therefore developed based on this selected stable GLP-1 analog for noninvasive imaging assessment of BCM. *In vivo* evaluation was carried out to determine the BCM targeting properties of the probe followed by *ex vivo* PET imaging and histology. Further, a reliable and reproducible multimodality imaging technique was developed by combining PET imaging with the GLP-1R targeted probe with anatomical imaging techniques including $BaSO_4$-enhanced CT and MRI for quantitative analysis of BCM imaging in mouse models. To test the potential of the imaging technique for longitudinal monitoring of BCM change during the diabetes initiation and progression, a serial PET/CT imaging was performed in a streptozotocin (STZ)-induced diabetic mouse model. With the successful development of the BCM imaging probe, a valid imaging technique has been established for noninvasive assessment of the progression of diabetes, which may find applications in early diagnosis of diabetes and monitoring therapeutic interventions of the disease.

TABLE OF CONTENTS

PRIOR PUBLICATIONS

Research article

1. Chen, W.J., Yen, C.L, **Lo, S.T.,** Chen, K.T., Lo, J.M., "Direct ^{99m}Tc labeling of Herceptin (trastuzumab) by [99m]Tc(I)-tricarbonyl Ion." *Applied Radiation and Isotopes,* 2008, Vol. 66, 340-345.

2. Mi, W.T., Wanjie, S., **Lo, S.T.,** Gan, Z., Pickl-Herk, B., Ober, R., Ward, E.S., "Targeting the Neonatal Fc Receptor for Antigen Delivery using Engineered Fc Fragments." *Journal of Immunology,* 2008, Vol. 181, 7550-7561. (PubMed # 19017944)

3. Lim, J., Chouai, A., **Lo, S.T.,** Liu, W., Sun, X., Simanek, E.E, "Design, Synthesis, Characterization, and Biological Evaluation of Triazine Dendrimers Bearing Paclitaxel Using Ester and Ester/Disulfide Linkages." *Bioconjugate Chemistry*. 2009, Vol. 20, 2154-2161. (PubMed # 19877601)

4. **Lo, S.T.,** Stern, S., Clogston, J.D., Zheng, J., Adiseshaiah, P.P., Dobrovolskaia, M., Lim, J., Patri, A.K., Sun, X., Simanek, E.E., "Biological Assessment of Triazine Dendrimers: Toxicological Profiles, Solution Behavior, Biodistribution, Drug Release and Efficacy in a PEGylated, Paclitaxel Construct." *Molecular Pharmaceutics*, 2010, Vol. 7, 993-1006. (PMC2914493)

5. Yen, C.L., Chen, W.J., **Lo, S.T.,** Chen, K.T., Yao, C.L., Lee, T.W., Lo, J.M., "Biodistribution of Tc-99m(I)-Tricarbonyl Labeled Trastuzumab as an Imaging Agent for Breast Cancer with HER2 Overexpression in Animal Model." *Annals of Nuclear Medicine and Molecular Imaging*, 2011, Vol. 24, 119-122.

6. *Lim J., **Lo, S.T.,** Hill, S., Pavan, G.M., Sun, X., Simenek, E.E.,"Antitumor Activity and Molecular Dynamics Simulation of Paclitaxel-laden Triazine Dendrimers." *Molecular Pharmaceutics*, 2012. Vol. 9, 404-412. (*co-first author) (PubMed# 22260328)

7. **Lo, S.T.,** Kumar, K., Hsieh, J.T., Sun, X., "Dendrimer Nanoscaffolds for Potential Theranostics of Prostate Cancer with a Focus on Radiochemistry" *Molecular Pharmaceutics,* 2013, Vol. 10, 793-812. (PubMed# 23294202)

8. Huang, F.Y., Chen, W.J., Lee, W.Y., **Lo, S.T.**, Lee, T.W., Lo, J.M., "*In vitro* and *In vivo* Evaluation of Lactoferrin-Conjugated Liposome as a Novel Carrier to Improve the Drug Delivery to the Brain" *International Journal of Molecular Sciences*, 2013, Vol. 14, 2862-2874.

9. Lee, C., **Lo,S.T.**, Lim, J., da Costa, V., Pavan, M.G., Annunziata, O., Sun, X., Simanek, E.E., "Design, Synthesis and Biological Assessment of a Triazine Dendrimer with 16 Paclitaxel Groups and 8 PEG Groups." 2013, *Molecular Pharmaceutics*, submitted

10. **Lo, S.T.,** Lin, M., Manandhar, B., Sagiyama, K., Long, M., Hill, S., Murage, E., Takahashi, M., Öz, K.O., Ahn, J.M., Sun, X., "Longitudinal PET Imaging of Pancreatic β-cell Mass Changes in a Mouse Model." 2013, in preparation.

11. **Lo, S.T.,** Murage, E., Ahn, J.M., Öz, K.O., Sun, X., "SPECT imaging of GLP-1R for the assessment of β- cell mass (BCM) change in a diabetic mouse model" 2013, in preparation.

12. **Lo, S.T.,** Ahn, J.M., Öz, K.O., Sun, X., "PET imaging of insulinoma using a ^{68}Ga-labeled GLP-1 analog" 2013, in preparation.

Meeting paper

1. Simanek, E.E., Sun, X., **Lo, S.T.,** and Lim, J., "Paclitaxel-triazine dendrimer constructs: Efficacy, toxicity and characterization," Abstracts of Papers, 240th ACS National Meeting, Boston, MA, United States, August 22-26, 2010 , PMSE-131 (2010)

2. **Lo, S.T.,** Murage, E., Ahn, J.M., Sun, X., "PET Imaging of Pancreatic β-cell Mass Changes in a Mouse Model." *J. Nucl. Med.* MEETING ABSTRACTS, 2011, Vol. 52, 86.

3. **Lo, S.T.,** Sagiyama, K., Ahn, J.M., Takahashi, M., Sun, X., "MRI-aided PET Imaging of Pancreatic β-cell Mass Changes in Mice." *J. Nucl. Med.*, 2012, Vol. 53, 1583.

4. **Lo, S.T.,** Thomas, P., Ahn, J.M., Öz, K.O., Sun, X., "SPECT Imaging of GLP-1R for the Assessment of Beta Cell Mass (BCM) Change in a Diabetic Mouse Model." *J. Nucl. Med.*, 2013, Vol. 54, 117.

5. Kumar, A., Lubag, A.J., Hao, G., **Lo, S.T.,** Whitener, L.A., Öz, K.O., Kovacs, Z., Sun, X., "A Bimetallic Complex System for Dual-modality Imaging of PET/MRI." *J. Nucl. Med.*, 2013, Vol. 54, 230.

6. **Lo, S.T.,** Manandhar, B., Ahn, J.M., Öz, K.O., Sun, X., "PET Imaging of Insulinoma using A ^{68}Ga-labeled GLP-1 analog." *J. Nucl. Med.*, 2013, Vol. 54, 249.

7. Guo, J., **Lo, S.T**., Sun, X., Öz, K.O., "Pancreatic Uptake of a Beta-cell Specific ^{68}Ga-labeled GLP-1 Peptide Analog in A Murine Model of Islet Amylod-associated Diabetes." *J. Nucl. Med.*, 2013, Vol. 54, 265.

LIST OF FIGURES

LIST OF TABLES

LIST OF SCHEMES

LIST OF EQUATION

LIST OF APPENDIX

LIST OF DEFINITIONS

%CV – Coefficient of Variation

%ID/g – The Percentage of Injected Dose per Gram

A1C – Hemoglobin A1C Test

AADC – Aromatic Amino Decarboxylase

ADA – American Diabetes Association

Ahx – 6-aminohexanoic Acid

BCM – Pancreatic B- Cell Mass

BFC – Bifunctional Chelator

BLI – Bioluminescence Imaging

BMI – Body Mass Index

BSA – Bovine Serum Albumin

CCD – Charged Couple Device

CB-TE2A – 4,11-bis(carboxymethyl)-. 1,4,8,11-tetraazabicyclo[6.6.2]hexadecane

CEST –Chemical Exchange Saturation Transfer

CHI – Cognitive Hyperinsulinism

CLSM – Confocal Laser Scanning Microscopy

CT – Computed Tomography

CTLA-4 – Cytotoxic T-lymphocyte Antigen 4

DCM – Dichloromethane

L-DOPA – L-3,4-Dihydroxyphenylalanine

DOTA –1,4,7,10-Tetraazacyclododecane-1,4,7,10-Tetraacetic Acid

DMF – Dimethylformamide

DMSO – Dimethyl Sulfoxide

DTBZ – Dihydrotetrabenazine

DTPA – Diethylenetriamine Pentaacetic Acid

DPP-IV – Dipeptidyl Peptidase-IV

Fab – Fragmented Antibody

FACS – Fluirescence-activated Cell Sorting

^{18}F-FBA – 4-[^{18}F]-fluorobenzaldehyde

^{18}F-FBBO – [^{18}F]-fluorobenzaldehyde-butylmaleimide

^{18}F-FBEM – [^{18}F]-fluorobenzamide-ethylmaleimide

^{18}F-FBT – [^{18}F]-fluorobenzyltrozamicol

FBS – Fetal Bovine Serum

^{18}F-FDOPA – L-3,4-dihydroxy-6-[^{18}F]-fluorophenylalanine

^{18}F-FDG – 2-Deoxy-2-[^{18}F]-fluoro-D-glucose

^{18}F-FE-DTBZ – [^{18}F]-fluoroethyl-dihydrotetrabenazine

^{18}F-FP-DTBZ – [^{18}F]-fluoropropyl-dihydrotetrabenazine

FPG – Fasting Plasma Glucose Test

^{18}F-SFB – N-succinimidyl-4-[^{18}F]-fluorobenzoate

GAD65 – Glutamic Acid Decarboxylase

GDM – Gestational Diabetes Mellitus

GELO – Gelatin-based Plasma Expander

GI tract – Gastrointestinal Tract

GIP – Glucose-dependent Insulinotropic Polypeptide

GlcNAc – N-acetylglucosamine

GLP-1 – Glucagon-like Peptide-1

GLP-1R – Glucagon-like Peptide-1 Receptor

GLUT2 – Glucose Transporter 2

H/E stain – Hematoxylin and Eosin Stain

HEK293 cells – Human Embryonic Kidney 293 cells

HLA – Histocompatibility Complex

HPLC – High Performance Liquid Chromatography

HYNIC – Hydrazinonicotinic

IAA – Insulin Autoantibody

IBMX – 3-Isobutyl-1-methylxanthine

IC50 – 50% Inhibitory Concentration

ICA – Islet Cell Autoantibody

IDDM – Insulin-dependent Diabetes Mellitus

IFG – Impaired Fasting Glucose

iTCL – Instant Thin Layer Chromatography

L-DOPA – L-3,4-dihydroxyphenylalanine

Log K – Stability Constant

Log P – Partition Coefficient

MALDI-TOF MS – Matrix-Assisted Laser Desorption/Ionization Mass Spectrometry

MRI – Magnetic Resonance Imaging

NEP 24.11 – Neutral Endopeptidase

NOTA – 1,4,7-triazacyclononane-1,4,7-triacetic Acid

OGTT – Oral Glucose Tolerance Test

OI – Optical Imaging

OND – Obese Non-Diabetes

OSEM – Ordered Subsets Expectation Maximization

PANIC ATTAC model – Pancreatic Islet β-cell Apoptosis through Targeted Activation of Caspase 8

PBS – Phosphate Buffered Saline

PCNA – Proliferating Cell Nuclear Antigen

PET – Positron Emission Tomography

PGA – Polyglutamic Acid

PP cells – Polypeptide Cells

PRRT – Peptide-receptor Radionuclide Therapy

PTPN22 – Protein Tyrosine Phosphatase Nonreceptor 22

RCP – Radiochemical Purity

RCY – Radiochemical Yield

RES – Reticuloendothelial System

RP-HPLC – Reverse Phase High Performance Liquid Chromatography

SNR – Signal to Noise Ratio

SOP – Standard Operating Procedure

SPECT – Single Photon Emission Computed Tomography

STZ – Streptozotocin

SUR – Sulfonylurea Receptor

SUV – Standard Uptake Value

T1D – Type 1 Diabetes

T1AD – Type 1A Diabetes

T1BD – Type 1B Diabetes

T2D – Type 2 Diabetes

T2D-GENES – Type 2 Diabetes Genetic Exploration by Next-generation Sequencing in multi-Ethnic Samples

TACN – 1,4,7-triazacyclononane

TFA – Trifluoroacetic Acid

TUNEL – Terminal Deoxynucleotidyl Transferase dUTP Nucleic End Labeling

US – Ultrasound Imaging

VAChT – Vesicular Acetylcholine Transporter

VGCC – Voltage-gated Ca^{2+} Channel

VMAT2 – Vesicular Monoamine Transporter Type 2

WHO – World Health Organization

DECLARATION OF ACADEMIC ACHIEVEMENT

All the experiments and data analysis were performed by myself in the entire dissertation except: In Chapter 3: Eunice N. Murage and Bikash Manandhar performed peptide synthesis, receptor potency, and enzymatic stability of GLP-1 analogs (**Fig 16 and 20**); In Chapter 4: Amit Kumar synthesized the multimeric EM2198 conjugates (**Scheme 3**). Mai Lin performed the synthesis of DOTA-GLP-1 analogs (**Scheme 4, Table 12**), the ^{64}Cu-radiolabeling of DOTA-GLP-1 analogs (**Scheme 5**), biodistribution (**Fig. 23**), and *ex vivo* stability (**Fig. 24**) studies; In Chapter 5, Koji Sagiyama performed the MRI (**Fig. 35**); In Chapter 7: Shiuhwei Chen performed the internalization study on confocal laser scanning microscope (**Fig. 45**). Risheng Ye developed the PANIC ATTAC model and performed the immunohistochemical staining for insulin (**Fig. 48**). William Silver, Jianfei Guo, Amit Kumar and myself performed the Ossabaw pig imaging study. Saleh Ramezani, William Silver, and Jianfei Guo helped the imaging analysis of pig project (**Fig. 51**).

CHAPTER ONE

BACKGROUND AND SIGNIFICANCE

1.1 Impact of Diabetes

1.1.1 Burden of diabetes

Diabetes mellitus had minor significance to the world populations less than a century ago. However, it became a main threat to human health in the 21st century[1]. Due to the population growth, increased life expectancy, urbanization, and most importantly the increasing prevalence of obesity, the number of people with diabetes in developing countries (Latin America, Africa, and Asia) is increasing[2, 3]. The past decade alone observed an explosive increase of the number of people diagnosed with this disease (**Table 1**)[4]. Based on the data from the 2011 Diabetes Fact Sheet, over 25.8 million people were affected by diabetes with an estimated 1.9 million newly diagnosed cases. The global diabetes prevalence in 2030 is projected to approach 439 million[5] of which people with type 2 diabetes (T2D) are the main factor. On the other hand, the growth rate of cases affected by type 1 diabetes (T1D) has been relatively slow. Both forms of diabetes approximately double the death rate due to the health issues compared to the non-diabetic persons[6]. Although diabetes ranks only the 7th cause of deaths in the United States (USA), it increases the risk of long-term health complications, one of which is the damage of blood vessels. The blood vessel pathology may have played a critical role in the doubling of cardiovascular diseases, the leading cause of deaths in the USA, such as ischemic heart disease (angina and myocardial infarction), stroke and peripheral vascular disease [7, 8]. Diabetes also causes retinopathy, nephropathy, and neuropathy.

Table 1. Global treat of Diabetes

Numbers of people with diabetes in 2000 and 2010 (in million)

Region	2000	2010	Increase (%)
North America	14.2	17.5	23
Latin America	15.6	22.5	44
Europe	26.5	32.9	24
Africa	9.4	14.1	50
Asia	84.5	132.3	57
Australasia	1.0	1.3	33
Total	151	221	46

1.1.2 Economic impact

In 2010, the average global expenditure on diabetes was 12% of the healthcare budget and varies by region and country's income level[9]. For example, the mean health expenditure per person with diabetes in the USA was $5,751, which is above 50- and 3-fold greater than the average in African and European regions, respectively. Based on the Economic Costs of Diabetes in the USA, the total cost of diagnosed diabetes cases increased 41% from $174 billion in 2007 to $245 billion in 2012. The latter total cost includes the direct medical costs ($176 billion: costs for hospital and emergency care, office visits, and medications) and the indirect costs ($69 billion: costs for absenteeism, reduced productivity, unemployment caused by diabetes-related disability, and loss of productivity due to early mortality). With the projection of 439 million people affected with this disease in 2030, the economic burden will severely affect the national health care systems worldwide. To reduce this coming economic burden, more effective prevention and monitoring efforts are needed.

1.2 Types of Diabetes

Diabetes mellitus can be categorized into three types: T1D, T2D, and gestational diabetes mellitus (GDM). Type 1 diabetes is also known as juvenile-onset diabetes or insulin-dependent diabetes mellitus (IDDM), which is usually seen in genetic susceptible children and young adults. The primary cause of T1D is the T-cell-mediated autoimmune response, which specifically attacks pancreatic β-cells. T1D can be further separated two sub-types: immune-mediated (autoimmune) (type 1A diabetes: T1AD) and idiopathic (type 1B diabetes: T1BD)[10]. In patients with T1AD, the rate of β-cell destruction varies from one person to another[11]. In this type of T1D, autoimmune markers such as autoantibodies to islet cell (ICA), insulin (IAA), glutamic acid decarboxylase (GAD65), and tyrosine phosphatases IA-2, are detectable in 85–90% of individuals when hyperglycemia initially occurs[12]. According to its different onset rates, T1AD can be defined in two forms: rapid- or slow-onset (**Fig. 1**). The rapid-onset form of T1AD is commonly seen in children[13] whereas the slow-onset form occurs mostly in adults. On the other hand, idiopathic T1D (T1BD) lacks markers relating to autoimmune attack on β-cells[10].
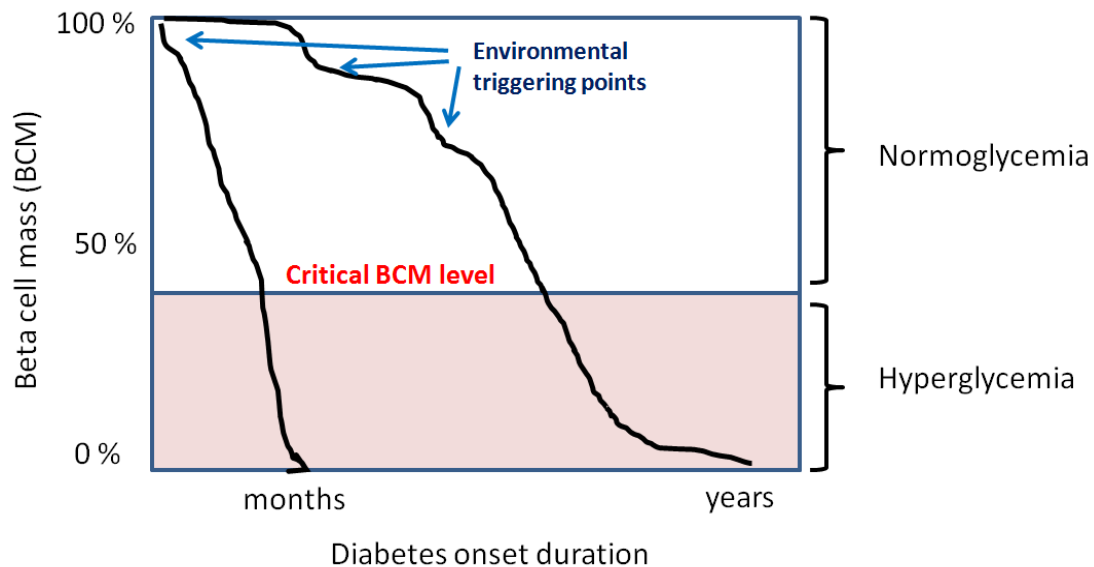
Figure 1. Schematic time course T1D development in human. Genetic markers are present in genetically susceptible subject from birth. Immune markers develop at the presence of the environmental factors that trigger the autoimmune response. The subject develops hyperglycemia after critical BCM loss[14].

While T-cell-mediated autoimmune response is known to be the direct cause of T1D, the genetic and environmental factors still remain unclear. Patients with T1D are born with one or more genes, which are known to increase the risk of diabetes, such as certain major histocompatibility complex (HLA isoforms: HLA-Dqα, HLA-Dqβ, and HLA-DR[15, 16]), protein tyrosine phosphatase non-receptor type 22 (PTPN22)[17], or cytotoxic T-lymphocyte antigen 4 (CTLA-4)[18]. In addition, viral infection also has been found to trigger this disease. To date, multiple viral pathogens have been recognized in this regard including rubella, coxsackievirus B4, retrovirus, rotavirus, cytomegalovirus, and Epstein-Barr virus[19]. The autoimmune response is then triggered by one or more environmental factors[20]. After an autoimmune response is elicited, autoantibodies that specifically recognize pancreatic β-cells develop. Patients can maintain normoglycemia until the critical number of functional β-cells is lost (**Fig. 1**). After the onset of

hyperglycemia, T1D is often characterized by the appearance of one or more autoantibodies[21]. Ultimately, most or all β-cells have been destroyed by the time the diagnosis has been made.
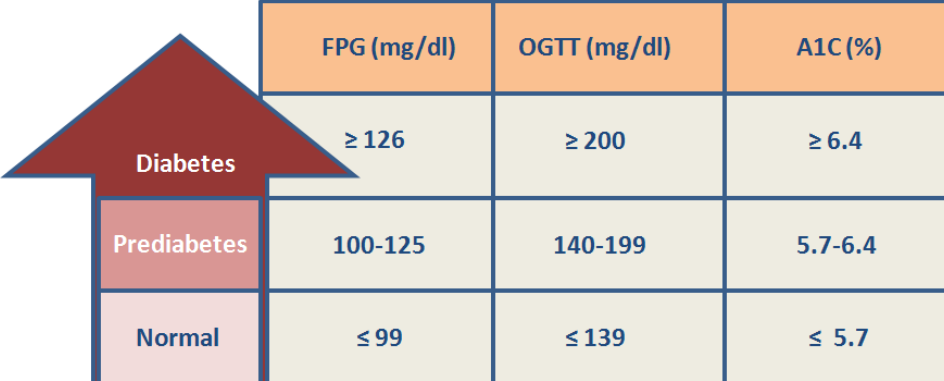
Type 2 diabetes is often known as adult-onset or noninsulin-dependent diabetes mellitus (NIDDM). It is the most frequently diagnosed form of diabetes and contributes over 90% to the overall diabetes cases[10]. The cause of T2D is a combination of multiple metabolic abnormalities which include increased hepatic glucose production, impaired insulin-mediated glucose disposal (insulin resistance) in multiple tissues, and inadequate production of insulin by pancreatic β-cells[22]. Surprisingly, genetic factors also play an important role in the onset of T2D. This has been demonstrated in a twin pair study, in which one of the twins was known to have T2D[23]. By monitoring the non-diabetic twin, the study showed that 91% of them also had T2D while 9% developed abnormal glucose tolerance or impaired fasting blood glucose level. In addition, several ethnic groups have been shown to be more susceptible to T2D[24-26]. As of 2011, 36 genes had been identified that relate to T2D[27]. Recently, the T2D-GENES (Type 2 Diabetes Genetic Exploration by Next-generation sequencing in multi-Ethnic Samples) project has been initiated to screen through the exome in a range of diverse ethnic groups for the identification of T2D-prone genes. However, T2D is a slowly progressing disease and its onset rate is determined by not only genetic factors but also the lifestyle, age, and gender of each individual patient. The most problematic issue with the current clinical methods for T2D diagnosis, is that β-cells have a reserved capacity of insulin production which can compensate for the increased metabolic demands[28]. Eventually, an impaired β-cell function occurs when more than 50% of β-cell mass (BCM) is lost.

Gestational diabetes mellitus (GDM), a common medical complication during pregnancy, can be diagnosed by glucose intolerance with varying degree[29]. Gestational diabetes is observed in 2 – 10% of pregnancies especially at the second and third trimesters. These two stages are characterized by insulin resistance due to the high metabolic demands of the fetus while maintaining the euglycemia in the mother[30]. The increasing number of pre-existing T2D also contributes the rising number of GDM. As a result, the number of pregnant woman with GDM doubled from 1994 to 2002[31]. In most of the cases (90%), diabetic symptoms disappear after pregnancy[32]. However, 15 – 60% of women who have had gestational diabetes may develop T2D within 5 – 15 years[33].

1.3 Clinical Relevancy of Diabetes Onset versus BCM Loss

While the hyperglycemic level in T1D is caused by the absolute deficiency of insulin secretion due to the autoimmune destruction of pancreatic β-cells[34], the development of T2D is more related to the prevalence of insulin resistance resulting from the progressive declination of β-cell function and/or mass[35]. However, the number of live and functional β-cells at the onset of T1D or T2D in a wide range varies with individual patients. In addition, there exist limited methods for the accurate quantification of BCM[36]. Currently, the BCM estimation in patients with diabetes solely depends on biopsy. Unfortunately, a repetitive sampling procedure is impractical in spite of the fact that a longitudinal monitoring of BCM changes in the same pre-diabetic/diabetic patient would add value to the diagnosis and treatment of diabetes. Therefore, BCM is usually indirectly assessed by determining glucose tolerance and insulin stimulation tests. Current clinical diagnostic methods, such as fasting plasma glucose test (FPG), oral glucose tolerance test (OGTT) or measuring A1C levels for both T1D and T2D patients, reflect β-cell

function (BCF)[37](**Fig. 2**), although, these are clinical manifestations of diabetes are seen after more than 50% of BCM is lost (e.g. 70 - 100% β-cell loss in T1D[38]; 65% β-cell loss in T2D[39])[40-43]. Currently, it is not possible to know the degree of BCM loss at the disease onset which is defined as the clinical transition point (**Fig. 3**), leading to a need for a sensitive noninvasive method to quantify the BCM *in vivo*[41]. The BCF parameters usually underestimate the BCM loss given the fact that the insulin production in individual β-cells can be increased to compensate the BCM loss. Therefore, lack of correlation is often observed between BCM and the BCF parameters (**Fig. 3**).

	FPG (mg/dl)	OGTT (mg/dl)	A1C (%)
Diabetes	≥ 126	≥ 200	≥ 6.4
Prediabetes	100-125	140-199	5.7-6.4
Normal	≤ 99	≤ 139	≤ 5.7

Figure 2. Clinical staging of diabetes. Fasting plasma glucose test (FPG); oral glucose tolerance test (OGTT); hemoglobin A1C test (A1C).
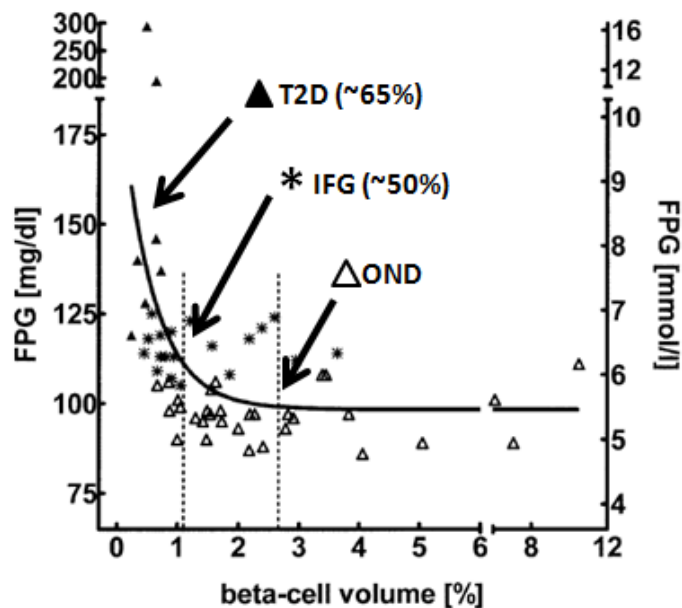
Figure 3. Relationship between percentage β-cell volume in pancreas and fasting plasma glucose level during T2D progression. The dashed vertical lines indicate the mean β-cell volume in obese nondiabetic subjects (Δ: OND) (right) and the impaired fasting glucose subjects (∗: IFG). The levels of BCM loss in the subjects of T2D (~65%) and IFG (~50%) were from autopsy. Reprinted from Ritzel R.A. et al.[44]. Copyright 2013 American Diabetes Association.

1.4 Unmet Clinical Needs in the Diagnosis of Diabetes

Current clinical glucose measurements only detect the abnormality when the functional β-cells are reduced below a critical threshold. Through the genetic typing of the HLA isoforms and measurement of specific antibodies in peripheral blood, it is now possible to identify those individuals with high risk of T1D[45]. However, these methods are limited by their low predictive values[46]. On the other hand, T2D-prone people can be identified through family history, measurements of insulin resistance, and body mass index (BMI). However, the majority of obese people are non-diabetic which indicate the current methods are not sensitive enough to define the actual level of the disease progression.

1.5 The Value of *In vivo* Assessment in Diabetes Research

Given the limitations of the current clinical methods, a noninvasive imaging technique is highly desirable for the accurate quantification of BCM changes during the diabetes progression or monitoring of the metabolic fate of islet transplants. Indeed, recently published noninvasive imaging methods have shown great potential in this regard[47-51]. The success of developing such a noninvasive method would: i) provide biological insight into the pathogenesis of diabetes, ii) facilitate the diagnosis of the disease, iii) enable the monitoring of therapeutic interventions, iv) provide a predictive biomarker during the progression of diabetes, and v) potentially monitor islet transplants prior to the occurrence of rejection[41].

1.6 Molecular Imaging

To fulfill the needs of noninvasive imaging of BCM for diabetes research and management, newly emerged molecular imaging methodology may offer opportunities. Compared to the conventional biological assay, molecular imaging is capable of providing visualization, characterization, and quantification of a biological event at cellular/subcellular levels within a live subject. Given the noninvasive nature of molecular imaging techniques, longitudinal monitoring a disease stage in the same individual becomes possible, which may lead to an efficacious therapeutic intervention. Commonly used molecular imaging techniques and their main features are summarized in **Table 2**[52, 53]. The basic physical concepts of these imaging techniques will be discussed in later sections.

Table 2. Characteristics of imaging modalities[52, 53]

Imaging technique	Spatial Resolution	Temporal resolution	Depth	Sensitivity (mole/L)
PET	1-2 mm	10 sec – min	no limit	$10^{-11} – 10^{-12}$
SPECT	1-2 mm	min	no limit	$10^{-10} – 10^{-11}$
MRI	25-100 µm	min – hour	no limit	$10^{-3} – 10^{-5}$
CT	50-200 µm	min	no limit	-
US	50-500 µm	sec – min	mm – cm	-
OI-BLI	3-5 mm	sec – min	1 – 2 cm	-

PET: Positron Emission Tomography, SPECT: Single Photon Emission Computed Tomography;
MRI: Magnetic Resonance Imaging; CT: Computed Tomography; US: Ultrasound;
and OI-BLI: Optical Imaging-Bioluminance Imaging

1.6.1 Radionuclide imaging

1.6.1.1 Positron Emission Tomography (PET)

PET is a tomographic imaging technique that is enabled by the administration of an imaging probe, or PET tracer, which carries a radioisotope that emits positrons (antimatter of electrons). The annihilation of a positron and electron pair gives off a pair of 511 keV gamma rays parting at opposite directions, which will be registered as a coincidence by a ring of detectors (**Fig. 4**) for imaging reconstruction. The emitted positrons travel a short distance in media before the annihilation happens. The physical distance of primarily sets the spatial resolution of PET is determined by the kinetic energy of the positrons. Commonly used PET radioisotopes are listed in **Table 3**[54].
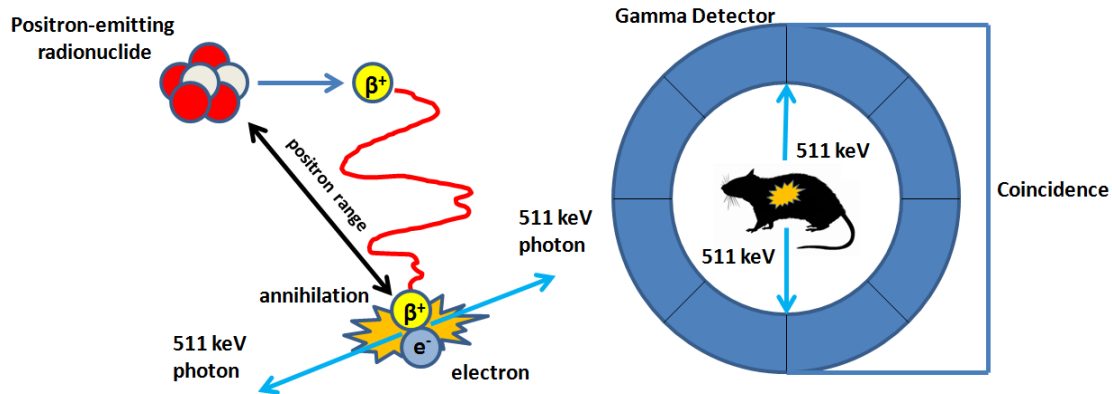
Figure 4. Schematic principle of PET

Table 3. Decay properties of common PET radioisotopes[54]

Radionuclide	Half-life	Positron Energy (MeV)	Positron (%)
C-11	20.3 min	0.9608	99
N-13	9.97 min	1.190	100
O-15	122.2 sec	1.723	100
F-18	109.8 min	0.635	97
Cu-64	12.701 h	0.65	17.4
Ga-68	1.130 h	1.89	89
Y-86	14.74 h	1.20	33
Zr-89	3.27 day	0.90	100
I-124	4.18 day	2.14	23

1.6.1.2 Single Photon Emission Computed Tomography (SPECT)

Similar to PET, SPECT relies on the detection of gamma rays directly emitted from a radioisotope. As its name indicates, SPECT imaging quantifies single photons registered as events by the detectors. In order to locate the photon source, a collimator, which is usually made of a tungsten or lead plate (adequate thickness to block incoming photons) with pinholes or septa, is mounted to the surface of the detectors (**Fig. 5**). Therefore, the spatial resolution of SPECT is primarily determined by the collimators' design. However, while in some cases the pinhole can

be made smaller to improve the imaging resolution, it reduces the imaging sensitivity by blocking

more of the incoming photons. Commonly used SPECT radioisotopes are listed in **Table 4**.
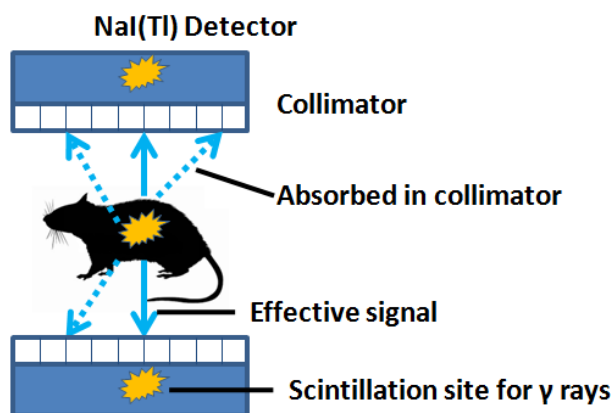
Figure 5. Schematic principle of SPECT

Table 4. Radiation decay properties of SPECT radionuclides

Radionuclide	Half-life	Energy (MeV)(abundance%)	Decay Mode
Ga-67	3.26 day	0.09332 (37%)	EC
		0.18459 (20%)	
		0.30024 (17%)	
Tc-99m	6.01 h	0.142 (100%)	I.T.
In-111	2.81 day	0.1712 (90%)	EC
		0.2453(94%)	
I-123	13.2 h	0.1590 (83.4%)	EC
I-125	59.4 day	0.0355 (7%)	EC
Tl-201	3.04 day	0.13528 (2.7%)	EC
		0.16740 (10%)	

I.T. = isomeric transition from upper to lower isomeric state; EC=orbital electron capture.
Data is adapted from Handbook of Chemistry and Physics[54] and Radionuclide Safety Data Sheets of Stanford University.

In general, a SPECT camera consists of 1 – 4 detector heads. By rotating the detectors,

the signal events are collected over the entire 360°path around the target of interest (**Fig. 5**).

Because of the need for collimation, SPECT is usually 2- to 3-orders of magnitude less sensitive

than PET. However, SPECT can be utilized to simultaneously detect photons with different

gamma energies, a unique feature to enable the imaging of multiple biological events at the same time, which is an impossible task for PET[55, 56].

1.6.2 Magnetic Resonance Imaging (MRI)

More mathematically and physically intriguing than radionuclide imaging, MRI is an aesthetic application of modern physics in biology and chemistry. Simply put, the basic concept of MRI is based on: i) when put into a strong magnetic field, nuclei with unpaired spins or magnetic dipoles are more aligned with than against magnetic field, ii) once the aligned nuclei are irradiated with different frequencies of radiofrequency (RF) energy, nuclear magnetic resonance (low energy parallel state excited to a high energy anti-parallel state) happens at the Larmor frequency that depends on the nature of the chemical bonding and its surrounding biochemical environment; iii) when the RF energy is turned off, the energy state reversion gives off a spectrum of frequencies as MR signals. An MRI scanner records the differential relaxation rates of the magnetic dipoles in the tissue being observed, protons in most of cases under different biochemical conditions, to their original states prior to the RF irradiation. For example, the relaxation rate of the protons in fat or a hydrocarbon-rich tissue is significantly shorter than in a water-rich environment. Because of its physical imaging mechanism and the fact that protons are abundantly present in soft tissues, MRI has exquisite spatial resolution and soft tissue contrast superior to PET or SPECT. However, the sensitivity of MRI is approximately 3 to 6 orders of magnitude lower than that of PET or SPECT when a biological event must be interrogated with a contrast agent.

1.6.3 Computed Tomography (CT)

Computed tomography is a tomographic imaging technique that affords anatomical images of internal organs based on the tissue differential attenuation coefficients of X-rays transmitted through a live subject[57]. Given the fact that calcified or dense tissues intrinsically have high X-ray attenuation coefficients, CT is a well-suited imaging technique for bone and solid masses. With the aid of iodine- or barium-based contrast agents, CT is capable of visualizing vasculature (CT angiography) and the gastrointestinal tract. Although the resolution of CT is physically limited by pixel sampling rate, X-ray source, and blurring in the phosphor screen[58], it can reach a few microns in *ex vivo* assays or post-mortem scans. However, for *in vivo* imaging, the bottle-neck limiting factor is the radiation dose, which the imaging procedure may impart to a live subject.

1.6.4 Optical Imaging (OI): Bioluminescence Imaging (BLI)

Bioluminescence imaging (BLI) contains two major components namely luciferase as biological reporter and ultra-sensitive low light charged coupled device (CCD) camera. Luciferase, can be genetically engineered and expressed within a live subject. By injection of the substrate (luciferin) of the luciferase, the visible light (560 nm for American firefly luciferase) is generated by oxidation reaction of luciferase which can be recorded by the CCD camera. BLI has the advantage of lower cost instruments compared to MRI, PET, and SPECT. However, this device also has several limitations. First, the transmission of light varies with tissue types depending on their hemoglobin content. The higher the hemoglobin content surrounding the reporter, the more the light transmission is reduced by hemoglobin absorbance of the emitted photon. For example, organs with high hemoglobin content such as liver and spleen have much

lower transmission than skin and muscle where hemoglobin levels are low. Second, the light signal attenuates 10-fold for every centimeter of tissue it travels[59]. Therefore, the tissue penetration depth of light and the water absorption are the major limiting factors of an optical imaging technique

1.6.5 Ultrasound Imaging (US)

Ultrasound is an imaging technique that has been widely used in clinical application. The US images are acquired when a high frequency (>20 kHz) sound wave is applied on the skin and the wave is reflected back from the internal organs. The image quality depends on the imaging algorithm used, back scattering, frequency and attenuation of the sound, and the operator. One positive attribute for US is it can be performed with a portable device at low cost. However, US is limited in the tissue with high air and bone content.

1.7 Current Status and Challenges of β-cell Imaging

The rapid advancement of imaging technologies has made molecular imaging a valuable tool with ever increasing importance in both clinical and basic biomedical research. Specific to diabetes, molecular imaging can provide information on β-cell function and mass during disease progression. However, the first challenge of β-cell imaging is the unique presentation of β-cells in the pancreas. Beta-cells locate in the islets of Langerhans of pancreas. The islets are sparsely and heterogeneously distributed throughout pancreas. Islets have a wide range of size (20 to 600 μm)[60] and only contribute to less than 3% of total pancreas mass. In addition, it has been reported that there is inter-species variation in islet structure and the percentage of β-cells in single islet (**Fig. 6**)[61]. For example, in human pancreatic islets, the β-cells share the whole islet space with other cell type and contribute to 60% of the total cell population. On the other hand, mouse β-

cells occupy the interior space of the islet and contribute more than 87% of total endocrine cell population[62] (**Table 5**). Therefore, the inter-species variation of islet heterogeneity may impact imaging assessments. Comparatively interpreting imaging data from species to species must be done cautiously.
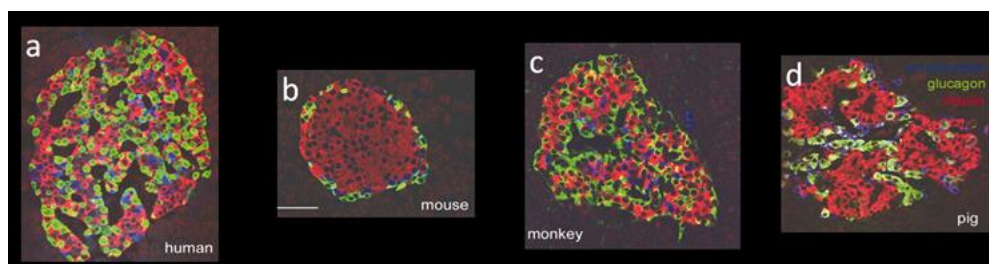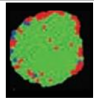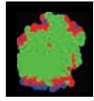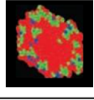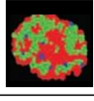
Figure 6. Inter-species differences of pancreatic islet construction. Confocal images of pancreatic sections containing islets of Langerhans from (a) human,(b) monkey, (c) mouse, and (d) pig were stained with insulin (red), glucagon (green), and somatostatin (blue) for β, α, and δ cells, respectively. Human and monkey islets showed random distribution of these cell types. By contrast, β-cells were located in the core, and α, and δ cells in the peripheral of mouse islets. Pig islets, on the other hand, are formed of subunits (three, in this case) with similar organization as individual mouse islets. (Scale bar, 50 μm). Reprinted from Cabrera, O. et al. [61]. Copyright 2006 National Academy of Sciences, U.S.A.

Table 5. Distribution of pancreatic endocrine cells in rodent, pig, nonhuman primate, and human[63]

Species	Morphology	α	β	δ	PP
Rodent		7% Periphery	87% Core	5% Periphery	rare Periphery
Pig		Periphery	Core	Few	Few
Nonhuman Primate		Core	Periphery	Core Periphery	Periphery
Human		36% Core Periphery	54% Core Periphery	10% Core Periphery	< 5% Core Periphery

α: α-cells; β: β-cells; δ: δ-cells; PP: polypeptide cells

The second challenge for β-cell imaging is that the imaging signal of β-cells is gradually decreased. In the early onset of T1D, β-cells are destroyed by autoimmune attack resulting in a rapid reduction of BCM. On the other hand, although BCM hyperplasia happens in the early stage of T2D, BCM is likely to reduce in the later stage[64]. Therefore, the imaging signal for β-cells in the progression of either T1D or T2D is decreased compared to the baseline.

Because of these two challenging issues, it is essential to develop an imaging technique with high sensitivity and superior resolution to quantify the small β-cell population with the negative of uptake signal during diabetes progression[65]. However, there is no molecular imaging technique. Among all molecular imaging techniques, PET and SPECT are the imaging modalities which have the high sensitivity. With the combination of specific targeting probes, both imaging modalities might provide great detection sensitivity. However, the imaging quantification might be affected by partial volume effect due to the limited resolution of PET and SPECT and the small and diffused β-cell population in pancreas[66]. On the other hand, conventional MRI and CT provide good spatial resolution in soft tissue contrast and skeleton, respectively, but their contrast agents lack specificity and have poor sensitivity. Therefore, the recently emerged multimodality imaging technique might provide better opportunity to imaging β-cells. In the following session, several advanced molecular imaging techniques are discussed to show the potential of β-cell imaging.

1.7.1 MRI for imaging β-cells

Conventional MRI- based imaging approaches are capable of locating the pancreas in live subjects; however, their roles in the imaging of endogenous β- cell islets are quite limited due to the poor sensitivity and lack of specificity of MRI contrast agents. One study attempted to improve the specificity and sensitivity by combining the targeting molecules for the GLUT 2 transporter on β-cells (G80BP) and contrast agent (Gd^{3+}) on MRI imaging of β-cells. By tagging the targeting molecules of β-cells with MRI contrast agents, the imaging specificity can be enhanced [67]. In addition, most preclinical MRI approaches are related to islet transplant imaging by pre-labeling islet graft with superparamagnetic iron oxide (SPIO)[68-71]. Moreover, MRI also can be used to image the aspects that are related to BCF. One of the targets is the high concentration of Zn^{2+} in the insulin granule released during the insulin secretion by using a Gd-based zinc sensor[72]. The other is to utilize the increasing Ca^{2+} influx rate in β-cells during glucose stimulation by using Mn^{2+} to mimic Ca^{2+} activity[73]. Both approaches showed enhanced MRI contrast within pancreas[74, 75].

1.7.2 PET and SPECT for imaging β-cells

PET and SPECT with their inherent superior sensitivity, relative ease to clinical translation and capability of absolute imaging quantification has shown its advantages in the imaging and noninvasive assessment of endogenous BCM in rodents[76, 77] and humans[48, 78]. The efforts in the PET and SPECT imaging of BCM have been mainly focused on the development of β-cell targeted imaging probes. Based on the targeting, mechanisms, to date, five major groups of

agents have been tested for BCM imaging: (1) Saccharide-based agents, (2) Sulfonylurea-receptor-targeted agents, (3) Antibody-based agents, (4) Neural imaging agents, and (5) Glucagon-like peptide 1 receptor (GLP-1R)-targeted agents [79]

1.7.2.1 Saccharide-based probes

An ^{18}F labeled glucose analog, 2-deoxy-2-^{18}F-fluoro-D-glucose (^{18}F-FDG) is the most widely used PET tracer in clinical PET procedures. It provides a noninvasive measure of the cellular glucose consumption primarily for cancer detection and staging. Based on the retention mechanism of ^{18}F-FDG and the observed glycogen accumulation in the β-cells[80], ^{18}F-FDG was among the first probes that had been tested for imaging the pancreas. Although ^{18}F-FDG was reported with high uptake in rat endocrine pancreas[81], this was not observed in humans[82]. D-mannoheptulose, a monosaccharide analog, was also explored as a potential candidate for β-cell imaging probes based on the finding that D-mannoheptulose is transported into the cells through glucose transporter 2 (GLUT-2), which is mainly expressed in hepatocytes and β-cells. However, the early effort of developing D-mannoheptulose-based β-cell imaging probes, such as 1-^{11}C-D-mannoheptulose, 3-deoxy-3-^{18}F-fluoro-D-mannoheptulose, and 1-deoxy-^{125}I-iodo-D-mannoheptulose[83] failed due to the low expression level of GLUT2 on human β-cells.

1.7.2.2 Sulfonylurea-receptor-targeted probes

Sulfonylurea-receptors (SUR1, SUR2A, or SUR2B) are essential subunits of inward-rectifier potassium ion channels Kir6.x (6.1 and 6.2) [84] in the plasma membrane of various cell types including pancreatic β-cells[85]. The association of four SUR1 and four Kir6.1 subunits forms

the potassium channel, K_{ATP}, which controls the membrane potential for the regulation of insulin secretion from β-cells[86]. Therefore, SUR-bound molecules have the potential to serve as not only antidiabetic agents but also imaging probes for pancreatic β-cells. Currently, sulfonylurea derivatives such as glyburide, tolbutamide, and repaglinide are antidiabetic agents, which stimulate insulin secretion in β-cells due to the high binding affinity to SURs [87-89].

An ^{18}F-labeled glyburide analog (glibenclamide) was one of the first SUR-targeted agents developed for β-cells imaging[90]. Indeed, the initial *in vitro* evaluation of the ^{18}F-labeled glyburide was positive. However, the *in vivo* evaluation showed that the compound had low and non-specific uptake in the pancreas and high uptake in liver and intestines. This can be attributed to the similar binding affinities of glyburide to SUR1 and SUR2. While only SUR1 was identified in pancreatic β-cells, it is known that SUR2 is expressed in cardiac, skeletal, and smooth muscles[91, 92], which would increase the nonspecific uptake of any glyburide-based agents. In addition, the glyburide analogs are highly lipophilic, which is not a desired feature for β-cell imaging because of the high liver uptake. Repaglinide anaologs labeled with ^{18}F or ^{11}C have also been tried for β-cell imaging. Interestingly, [^{11}C]-repaglinide was found to have higher binding affinity and specificity to SUR1 than [^{18}F]-repaglinide indicating that the fluoroethyl group decreases the specific binding affinity to SUR1. However, the specific uptake of either of the tracers in the pancreas was too low to afford them practical application in β- cell imaging[93].

1.7.2.3 Radiolabeled antibodies

As shown in the failed trials of using a glyburide derivative for β-cell imaging, high binding affinity to a specific biomarker which is uniquely expressed on the surface of β-cells is

the key to probe development. Due to their high specificity towards certain antigens, antibodies have the potential to meet this requirement. Among the monoclonal antibodies identified with binding specificity to the membrane proteins of β-cells[94] the IgM kappa monoclonal antibody (IC2, generated from a β-cell hybridoma that targets a zinc transporter [94, 95]) had been regarded as the best candidate for the β-cell imaging.

Direct modification of IC2 with diethylene triamine pentaacetic acid (DTPA) enables the antibody to be labeled with ^{111}In (a radioisotope used in SPECT imaging) and has been used to image the pancreas in normal and diabetic mouse models[95]. While the radiolabeled antibody showed significantly lower uptake in the pancreas of diabetic mice as expected, the main drawback of using an intact monoclonal antibody as an imaging probe was obvious: slow blood clearance and high liver uptake. To overcome this hurdle, antibody fragments (Fabs) or engineered fragments could be used if the desired high specific binding is not compromised. Indeed, such efforts are represented by using another existing β-cell specific antibody (K14D10) and showed promising results[96]. However, the nonspecific uptake in liver remains problematic and the specific pancreas accumulation must be further enhanced for the practical application of β-cell imaging in future.

1.7.2.4 Neural imaging probes

In spite of the differences in the embryological development, β-cells and neural cells share similarities in gene and translational profile[97]. In both cell types, common proteins that have been found include dopamine β-hydroxylase [98], glutamate receptor [99], aromatic amino decarboxylase (AADC), glutamic acid decarboxylase [100], tyrosine hydroxylase [101], type II

voltage-dependent sodium channel [102], neurofilament proteins [103], receptors for neurotrophins[104], thyrotropinreleasing hormone [105], dopamine D_2-like receptor [106], and vesicular monoamine transporter (VMAT2)[107-109]. In addition, it is known that both parasympathetic and sympathetic innervations tightly control the pancreatic endocrine and exocrine functions [110]. Hence, the targets of the well validated neural imaging probes may very well be expressed in β-cells[97, 111] allowing commonly used neural imaging agents to be directly used for β-cell imaging.

L-3,4-dihydroxyphenylalanine (L-DOPA) is a drug for the treatment of Parkinson's disease. It can be efficiently converted into dopamine by AADC. Based on this, L-DOPA has been modified with ^{18}F to produce a PET imaging tracer (L-3,4-dihydroxy-6-^{18}F-fluorophenylalanine, ^{18}F-FDOPA) to monitor the density of dopaminergic neurons for the diagnosis of neurodegenerative diseases. Given the fact that AADC is also expressed in the insulin granules of β-cells[112], it has been observed that dopamine levels increase in these granules after administering L-DOPA[113]. Hence, ^{18}F-FDOPA labeling has become widely used to detect neuroendocrine disorders especially cognitive hyperinsulinism (CHI)[114]. Cognitive hyperinsulinism is a leading cause of severe hypoglycemia in the infancy. Imaging ^{18}F-FDOPA offers precise pre-operative localization of the medically unresponsiveness focal lesion, thus assisting the extent of surgical removal[112, 113].

Targeting the D_2 receptor, found in the insulin granules of β-cells, ^{18}F-Fallypride has also been tested to image β-cells. Indeed, the pancreatic uptake of ^{18}F-Fallypride was observed with a significant decrease in the diabetic mice, which likely reflects the β-cell loss during the disease progression. However, the low pancreas uptake of ^{18}F-Fallypride (0.05 percentage of injection dose per gram (% ID/g)) [115] limits its application in β-cell imaging.

As implied in the above two cases of using neural imaging agents for β-cell imaging, the biomarker expression density or level is critically important when considering a targeting moiety to assess the β-cell declination in the progression of diabetes. Another important issue of concern is the specificity of the biomarker expression. For instance, the vesicular acetylcholine transporter (VAChT), whose expression is significantly higher in isolated islets than in the exocrine tissues[116], has been targeted by ^{18}F-fluorobenzyltrozamicol (^{18}F-FBT). Positive imaging results of ^{18}F-FBT were observed in the pancreas of three mammals (mouse, monkey, and human) [117]. However, recently it was found that the VAChT expression in the pancreatic islets is species-dependent[116]. While in mouse islets, the VAChT is mainly expressed in β-cells, over 80% of VAChT positive cells in human islets are glucagon positive, indicative of α-cells, and few VAChT positive cells secrete somatostatin (δ-cell) or insulin (β-cell). Hence, the early imaging results of ^{18}F-FBT might not truly reflect the population of β-cells in the mammals.

To date, ^{11}C- or ^{18}F-labeled dihydrotetrabenazine (^{11}C-/^{18}F-DTBZ), a neural imaging agent[118-120], still remains the most promising ligand for imaging endogenous β-cells. The DTBZ agents target the VMAT2[121-124], which is presumably expressed in β-cells with high specificity. Indeed, the gradual reduction of BCM was impressively captured by PET imaging with [^{11}C]-DTBZ in a longitudinal diabetes progression study in rodents[77, 122, 125] and humans[121]. However, in the published reports and our own observation (**Fig. 7**), VMAT2 is also expressed in the small population of PP cells[108, 126]. In other words, [^{11}C]-DTBZ-PET may have an inherent nonspecific uptake background, which impedes the accurate imaging interpretation in patients with nearly complete loss of β-cells. Two ^{18}F analogs of tetrabenazine, 9-[^{18}F]fluoropropyl-(+)- and 9-[^{18}F]fluoroethyl-(+)-dihydrotetrabenazine ([^{18}F]-FP- and [^{18}F]-FE-(+)-DTBZ) have also been

tested for β-cell imaging[123, 127]. However, these results indicate that [^{18}F]-FP-(+)-DTBZ has potential to identify the differences between normal and diseased subjects. Though, dehalogenation and nonspecific binding of exocrine tissue make [^{18}F]-FE-(+)-DTBZ not practical for β-cells imaging[126]. Most recently, a negative imaging report appeared that [^{18}F]-FP-DTBZ) and its derivatives did not bind specifically to β-cells in an inducible selective β-cell ablation mouse model[128]. One of the explanations for the confusing imaging interpretation is that the inter-species differences of the VMAT2 expression[129]. Indeed, based on a recent published report, VMAT2 is expressed in human and pig but not in experimental rodent models[107]. However, we cannot ignore the fact of VMAT2 expression in the PP cells, which are significantly expressed in the pancreas head region in human[124, 125]. Although VMAT2 might be questionable to detect β-cells in a mouse model, it is still a valuable imaging technique for β-cells imaging in human by avoiding imaging quantification in the region with nonspecific expression of VMAT2.
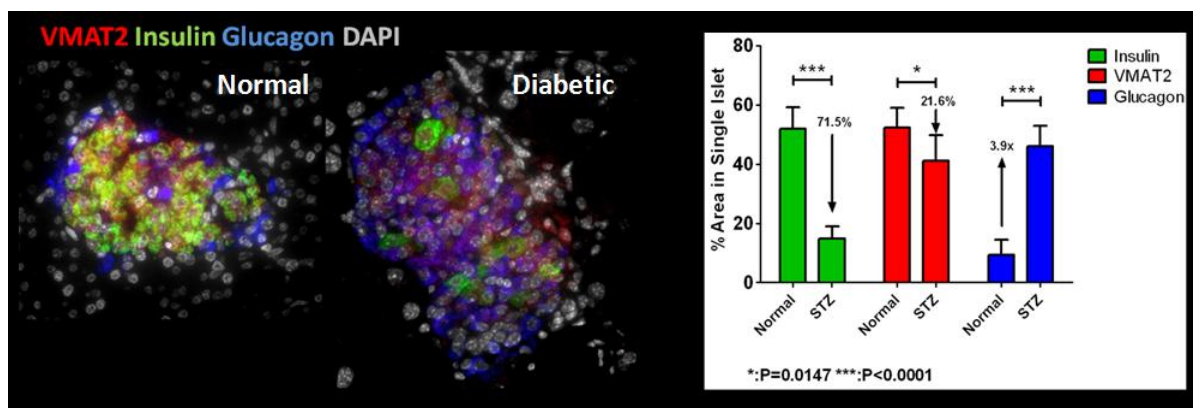
Figure 7. Triple immunofluorescence staining for VMAT2, Insulin, and Glucagon in normal and diabetic mouse islet. VMAT2 (red), insulin (green), and glucagon (blue). Right panel indicates the differences between the expression levels of VMAT2, insulin, and glucagon.

1.7.2.5 Glucagon-like peptide 1 receptor (GLP-1R)-targeted probes

Glucagon-like peptide 1 receptor (GLP-1R) is another target that can be exploited for β-cells imaging. Indeed, GLP-1R is specifically expressed in the endocrine tissues but exocrine tissues of the pancreas of humans and rodents[132, 133] are devoid of this receptor. The expression level of GLP-1R in β-cells might be down-regulated under diabetic hyperglycemic conditions[130]. This may add complexity to the imaging methods that use the GLP-1R density as the surrogate marker of BCM.

Due to the short biological half life (~2 min) of the endogenous ligand for glucagon-like peptide-1 (GLP-1) in rodents[131] and human subjects[132, 133]most published work used a stable GLP-1R agonist, exendin-4, and its derivatives to image insulinoma[136, 137], transplanted human islets[134], or BCM [135, 136]. *In vivo* SPECT imaging using an ^{111}In-labeled exendin-4 agent, ^{111}In-DTPA-Lys40-exendin-4, demonstrated the tracer's specific uptake in GLP-1R-positive tissues such as lung, pancreas, and the stomach antrum[137]. Recently, exendin-4 was labeled with ^{18}F and tested in normal mice to validate whether the GLP-1R can serve as a biomarker for β-cell imaging by a biodistribution study and *in vivo* PET imaging[138]. The biodistribution study revealed that the pancreas had the second highest uptake next to the lungs[139]. The *in vivo* PET imaging evaluation further demonstrated the promising potential of exendin-4 and its analogs for β-cell imaging.

1.8 Development of Peptide-based Radiopharmaceuticals for Molecular Imaging

In the previous section, several potential β-cells targets were described. Among all, only GLP-1R imaging is targeted by radiolabeled peptide such as [18]F-, [64]Cu-, [99m]Tc-, and ^{111}In-labeled

exendin[138, 140-144]. For more than 20 years, radiolabeled peptides have been widely used in targeted diagnostics and therapeutics[145-147] especially in oncology. Peptide-based radiopharmaceuticals have distinctive advantages over other biologically active molecules such as proteins and antibodies. For example, peptides can be easily synthesized and modified using a peptide synthesizer. They have a rapid pharmacokinetic profile or fast blood clearance due to its relatively smaller size than proteins and antibodies. Also, they can tolerate the harsh condition of radiolabeling procedures in terms of either high temperature or non-biocompatible pH values. Additionally, structural elements of the peptides can be modified to optimize their binding affinity toward particular receptors. With the positive properties, peptides have high affinity to specific receptors which are overexpressed in numerous cancers, compared to the low density in physiological organs[148]. Combining peptide-based radiopharmaceutical with molecular imaging provides the potential to understand diseases at the cellular and molecular levels.

There are several key elements for the development of a successful receptor targeting peptide-based radiopharmaceutical: i) Target. The molecular target (receptor) of the peptide can be identified by receptor autoradiography or immunohistochemistry. ii) Biological half life and receptor affinity. The peptide analog system can be developed based on the structure of the endogenous peptide. This system can be designed to enhance metabolically stability while maintaining high receptor binding affinity through modifications. iii) Radiolabeling. The peptide analog can be labeled with radiometals, radioiodine, or ^{18}F. For radiometal labeling, the peptide analog can be covalently conjugated, *via* a spacer, to a chelator which can form a complex with radiometals. On the other hand, the peptide analog carries a prosthetic group which can be labeled with radioiodine or ^{18}F. The radiolabeled peptide analog should allow high labeling yield and radiochemical purity. Most importantly, it is ideal to maintain the high specific activity of the

peptide with peptide-based imaging probes, which can increase the specificity of the probe and reduce any adverse pharmacologic effects. iv) *In vitro* characterization. The radiolabeled peptide can be characterized with *in vitro* binding study in cells or tissue homogenate to evaluate the binding affinity. v) *In vivo* evaluations. Biodistribution of the radiolabeled peptide can be evaluated in animal model. Studies such as tissue distribution, pharmacokinetics, *in vivo* stability are used to characterize the pharmacological behavior of the peptide analog. Moreover, the *in vivo* imaging is conducted to evaluate the specificity of the radiolabeled peptide to the target to help determine the ratio of uptake into the target area with respect to surrounding organs.

1.8.1 Labeling of radionuclide on peptide

^{18}Fluorine-18 (^{18}F) and ^{99m}Tc are the two popular choices of isotope in PET and SPECT imaging, respectively, due to the favorable nuclear physical characteristics (**Tables 3 and 4**). For ^{18}F labeling, direct labeling methods with either electrophilic addition or nucleophilic substitution on aromatic containing units on peptide residues have been investigated[153, 154]. However, this approach might compromise the functionality and stability of the peptide. Therefore, fluorination of peptides is often performed by ^{18}F-labeled prosthetic groups through fluroalkylation, fluoroacylation and fluoroamidation on –NH$_2$, -SH, -OH, or –COOH functional groups. Among all the prosthetic groups, the N-succinimidyl 4-[^{18}F]flurobenzoate ([^{18}F]SFB) is used because it provides high radiochemical yield and high *in vivo* stability of the product[149]. However, multiple steps are involved in the synthesis. This limitation has been improved through single-step fluorination by 4-[^{18}F]fluorobenzaldehyde ([^{18}F]FBA)[150]. Other ^{18}F-labeled prosthetic groups such as 4-[^{18}F]fluorobenzamide-ethylmaleimide ([^{18}F]FBEM), and 4-[^{18}F]fluorobenzaldehyde-

butylmaleimide ([^{18}F]FBBO) are used to specifically label –SH group in peptides[151]. Moreover, the click reaction also can be applied on the fluorination using [^{18}F]fluoroethylazide and [^{18}F]-glycosyl-azide[152]. Recently, new ^{18}F-labeling methods using fluorides of silicon, boron, and aluminum have also been explored[153-155]. These methods provide a higher yield and shorter synthesis processing time for fluorination. In particular, the bifunctional chelator (BFC) 1,4,7-triazacyclononane-1,4,7-triacetic acid (NOTA) has been utilized in the formation of a stable complex with Al^{18}F^{2+} and showed the potential to be developed for ^{18}F labeling[156]. This BFC chelating strategy is widely used in the labeling of radiometals including ^{99m}Tc, M^{3+} radiometals (^{111}In, $^{86/90}$Y, ^{177}Lu, $^{67/68}$Ga) and $^{64/67}$Cu. To perform the radiometal labeling on peptide through BFC, there are four major components need to be taken consideration: (1) Targeted peptide, (2) spacer or linker, (3) BFC and (4) the radiometal (**Fig. 8**)
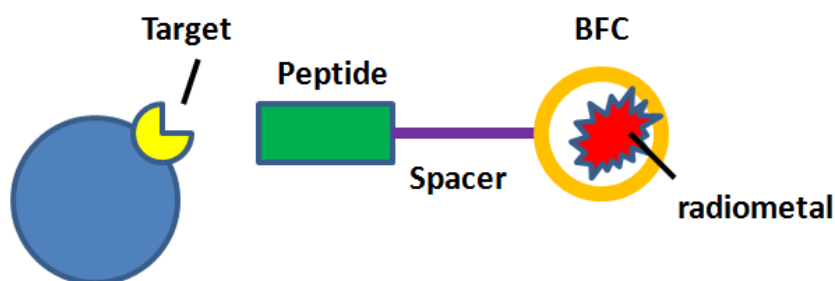
Figure 8. Key components for designing a radiometal-labeled peptide-based radiopharmaceutical for receptor targeting.

While targeted peptides can be identified by either phage display screening [157]or synthesized based on the target, the spacer is determined by the pharmacokinetics. Also, spacers can be a separator between the peptide and the bifunctional chelator to minimize the possibility of reducing receptor affinity of the peptide. The bifuctional chelator is determined by the nature of

the radiometal. For example, when ^{99m}Tc is eluted from a ^{99}Mo generator in saline solution, it is formed as ^{99m}TcO$_4^-$(VII). ^{99m}TcO$_4^-$(VII) is relatively chemically inert, as such, it has to be reduced to a lower oxidation state (I-V) to allow it to be complexed with a BFC to meet the requirement of high specific activity of a peptide-based radiopharmaceutical. It has to be thermodynamically and kinetically inert to survive *in vivo*. Several BFCs such as diamidedithiols (N$_2$S$_2$)- , triamidethiols (N$_3$S)-, tetraamines (N$_4$)-based [158-160] or hydrazinonicotinic acid (HYNIC) [143, 161] have been evaluated upon conjugation to a peptide to test this goal.

CHAPTER TWO

RATIONALE AND AIMS

2.1 Project Rationale

Diabetes is a metabolic disorder characterized by β-cell loss (or exhaustion) and insulin deficiency. Current diagnostic methodologies of diabetes are limited by sensitivity and specificity. As a result, patients with diabetes were diagnosed when over 50% of BCM is lost. Therefore, a reliable and reproducible noninvasive imaging technique that enables direct assessment of BCM would be highly desirable. It has been reported that Glucagon-like Peptide-1 Receptor (GLP-1R) is specifically expressed in pancreatic β-cells. GLP-1R would be a plausible target to develop PET imaging probe for BCM. However, the endogenous GLP-1R ligand, GLP-1 undergoes rapid enzymatic degradation, hence is not feasible for probe development. Therefore, a series of modified GLP-1 analog with enhanced enzymatic stability and receptor potency was developed. The goal for this dissertation has been set to develop a GLP-1-based PET imaging probe based on the stable GLP-1 analog to imaging BCM. **We hypothesize GLP-1-based PET imaging probes can specifically bind to β-cell GLP-1R for noninvasive monitoring of diabetes progression.** To accomplish the goal and test the hypothesis, four specific aims were proposed:

2.2 Specific Aims
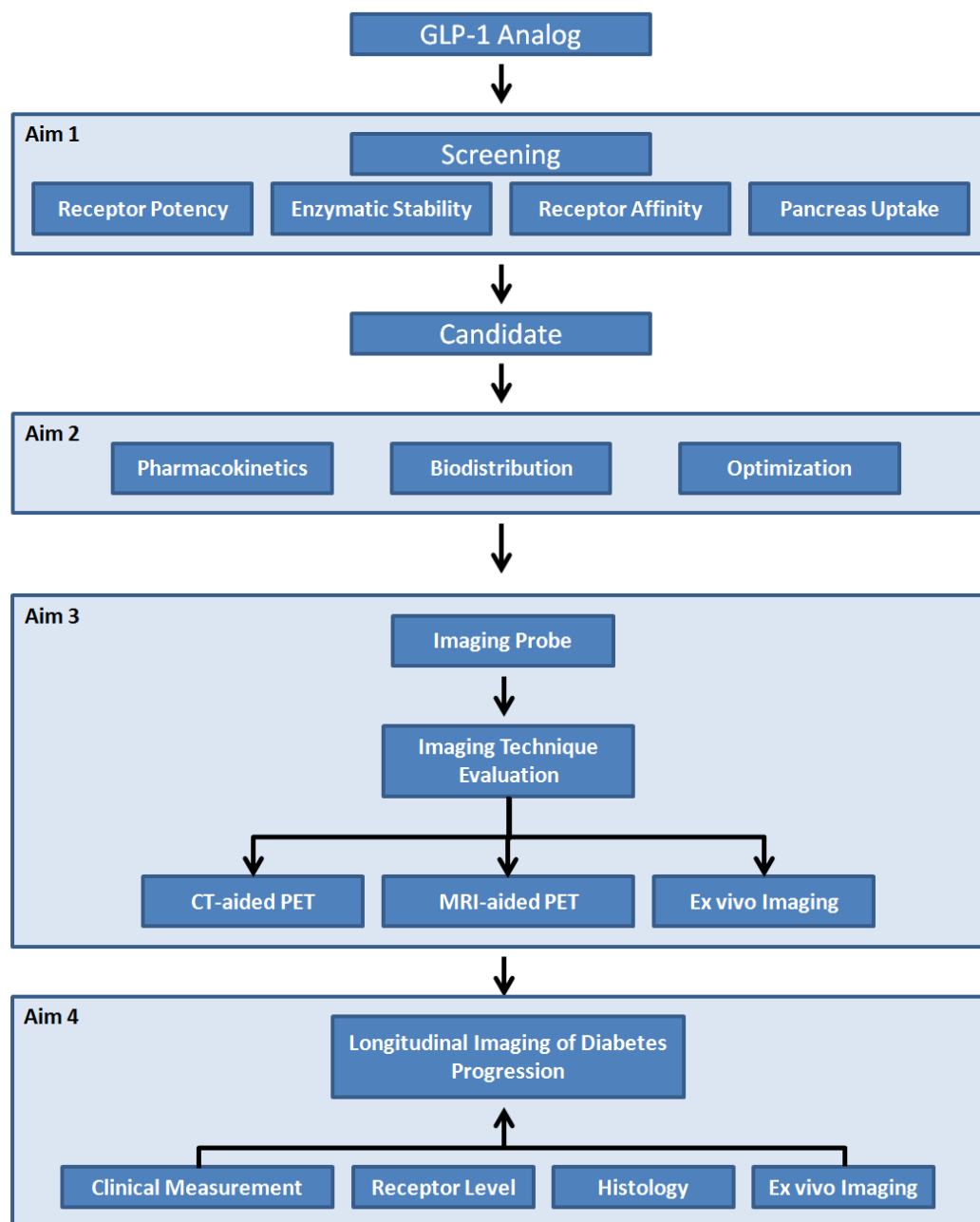
Figure 9. Project flow chart with specific aims

Aim 1: Evaluation of GLP-1 analogs as BCM imaging probe candidates.

To select the candidate for probe development, two distinct sub-aims were arranged:

Aim 1A: To evaluate the receptor binding affinity of GLP-1 analogs by a competitive receptor binding assay. Competitive receptor binding assay was performed with GLP-1R-positive mouse insulinoma cells (β-TC6) in the presence of ^{125}I-exendin and GLP-1analog. The GLP-1R binding affinity of a GLP-1 analog was determined by IC50 (half maximal inhibitory concentration) value.

Aim 1B: To evaluate the pancreas uptake of the GLP-1 analogs by *ex vivo* PET imaging. GLP-1analogs were radiolabeled with a PET isotope, ^{68}Ga, through NOTA bifunction chelator (BFC). PET imaging of excised pancreas was conducted in normal mice that had received an intravenous injection of ^{68}Ga-radiolabeled GLP-1 analogs before sacrifice. Tracer uptake level in pancreas was determined by percentage injected dose per gram (%ID/g).

Aim 2: Evaluations of the PET probe derived from selected GLP-1 analog, EM2198

Two distinct sub-aims were arranged:

Aim 2A: To evaluate the biodistribution profiles and *in vivo* metabolism of radiolabeled EM2198 conjugate. The biodistribution studies were performed to evaluate the tissue accumulation and the blood clearance of the radiolabeled peptide conjugate. The

blood from the mice that were injected with the radiolabeled peptide was analyzed by HPLC for *in vivo* peptide stability.

Aim 2B: To optimize receptor binding affinity of the imaging probe by using multivalent effect. A series of EM2198-based imaging probes were developed on the mono-, di-, and trivalent NOTA BFC scaffold by labeling with ^{68}Ga. The multivalent probes were injected in normal C57BL/6 mice. Probe distribution in whole body was analyzed by *in vivo* PET imaging.

Aim 3: PET imaging evaluation of radiolabeled EM2198: BCM imaging and quantification.

Three strategies were employed to evaluate the imaging potential and to improve the imaging quantification of radiolabeled EM2198 on *in vivo* PET.

- BaSO$_4$-aided CT imaging: To facilitate anatomical delineation of pancreas *via* BaSO$_4$-enhanced CT contrast in gastrointestinal tract.
- MRI: To assist the identification of pancreas *via* high soft tissue resolution of MRI
- *Ex vivo* PET imaging: To validate the tracer uptake in excised pancreas.

The excised pancreas was examined by histology and/or immunohistochemical staining of pancreatic endocrine cell-specific biomarkers and correlated to imaging results. Imaging reproducibility was determined by coefficient of variation (%CV) which was analyzed from *in vivo* PET imaging data set.

Aim 4: Longitudinally monitoring the dynamic changes of BCM in a STZ-induced diabetic mouse model

STZ-induced T1D mouse model was used to monitor the dynamic changes of BCM over time. *In vivo* PET imaging was performed on 0, 6, 9, 15, 18, and 35 days after the STZ treatment. At each time point, three mice were randomly selected and pancreas was excised for *ex vivo* PET imaging. The pancreas tissues were collected for histological staining of β-cell markers as BCM parameters. The β-cell function (BCF) of the mice was measured by the fasting blood glucose level. GLP-1R expression level was evaluated by Western blots. The imaging readouts of BCM change during the STZ-induced T1D progression were then correlated with the receptor density, conventionally measured BCM, and BCF parameters

2.3 General Research Strategy

2.3.1 Radiochemistry

2.3.1.1 Choice of radiometal

In this dissertation, we used several different radiometals to label with the GLP-1 analog. In the Aim 1, ^{68}Ga was chosen to label a large number of GLP-1 analogs for *ex vivo* PET screening. In the Aim 2, ^{67}Ga and ^{64}Cu were favorable over ^{68}Ga because of their longer half lives (^{67}Ga: 3.26 day; ^{64}Cu: 12.7 h) which was suitable for pharmacokinetics, biodistribution, and *in vivo* imaging evaluation. In the Aim 3, ^{64}Cu and ^{68}Ga were used. Due to the favorable nuclear physical characteristics of ^{64}Cu (positron energy: 0.65 MeV), a better imaging quality and more accurate imaging image quantification was feasible compared to ^{68}Ga (1.89 MeV). In the later study, we used ^{68}Ga for the evaluation due to eventual goal of longitudinal imaging in Aim 4. ^{68}Ga is available on as-needed basis from a benchtop ^{68}Ge/^{68}Ga generator system without the requirement of an onsite cyclotron.

2.3.1.2 Choice of BFC for radiometal labeling

The conventional radiometal bifunctional chelator, 1,4,7,10-tetraazacyclododecane-1,4,7,10-tetraacetic acid (DOTA), was first conjugated with selected GLP-1 analog for ^{64}Cu labeling and used for *in vivo* evaluation and PET imaging. Cu-DOTA complex forms a pseudo-octahedral geometry (**Fig. 10**). The Cu is significantly distended from the chelator cavity, which may account for its significantly lower inertness compared to Ga-NOTA. Indeed, compared to the Ga-NOTA complex, the stability of Cu-DOTA is much lower (log K= 22.3) [162] and often leads to the transchelation of Cu^{2+} from DOTA to serum proteins resulting in higher non-specific binding in liver and kidneys [163-165].
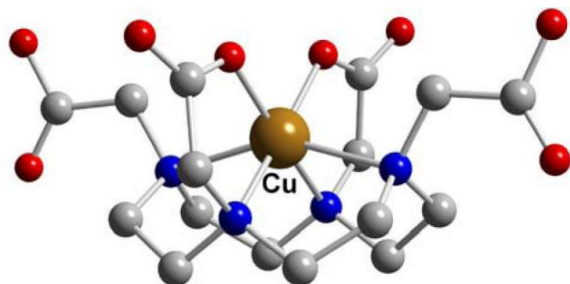
Figure 10. Structure of Cu-DOTA complex. The DOTA chelator transforms into a distorted *pseudo*-octahedral N_4O_2 envelopment to chelate the Cu^{2+}[166]. The color indicates different atom: Copper (brown), carbon (grey), nitrogen (blue), and oxygen (red).

To improve the instability of Cu-DOTA complex formation, an alternative chelator is required for development of a stable ^{64}Cu-labled imaging probe. Based on the published reports, the complex of Cu^{2+} and cross-bridged cyclam chelator, 4,11-bis(carboxymethyl)-1,4,8,11-

tetraazabicyclo[6.6.2]hexadecane (CB-TE2A) has better kinetic inertness compared to the Cu-DOTA complex[167, 168]. Cu-CB-TE2A has been found to be much stable than Cu-DOTA complex.

Ga^{3+} forms a highly stable complex with the tris-acetate pendant armed 1, 4, 7-triazacyclononane (TACN) derivative, NOTA [169] (**Fig. 11**), with the log K of 30.1[170]. This Ga-NOTA complex can remain intact in 5M HNO$_3$ for over 6 months. Therefore, NOTA was chosen in the study for labeling with $^{68/67}$Ga.
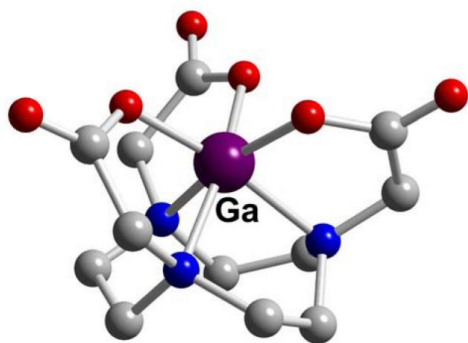
Figure 11.   Structure of Ga-NOTA complex. The NOTA chelator transforms into a distorted octahedral N$_3$O$_3$ envelopment to chelate the gallium cation[166]. The color indicates different atom: Gallium (purple), carbon (grey), nitrogen (blue), and oxygen (red).

2.3.1.3 $^{68/67}$Ga radiolabeling

In the aqueous condition, gallium is a hard Lewis acid in 3+ form as their major oxidation state. It can form a stable complex with hard Lewis bases. Radiometal chelators such as NOTA has donor groups such as oxygen and nitrogen from carboxylate and amine which can form a stable complex with gallium[166]. Ga^{3+} can hydrolyze to insoluble colloidal particle Ga(OH)$_3$ at pH around 5 which is dependent on the concentration. At physiological pH, Ga^{3+} has better solubility due to the formation of [Ga(OH)$_4$]$^-$ ions. In general, pH level between 2 to 4 is the suitable

condition for ^{68}Ga labeling. Given the high tolerance of peptides for harsh conditions such as low pH or high temperature, the labeling condition of ^{68}Ga has less effect on the peptide.

2.3.2 Choice of diabetes animal model

Streptozotocin (STZ)-induced diabetes mouse model was the disease model in my dissertation. It has been widely used in diabetes research[171] due to the disease development mechanism after STZ treatment, which is similar to human T1D and T2D[172-175]formation. In brief, streptozotocin (2-deoxy-2-(3-(methyl-3-nitrosoureido)-D-glucopyranose) is a glucosamine derivative with structural similarity to N-acetylglucosamine (GlcNAc) [176] (**Fig. 12**). Therefore, it can enter β-cells through the glucose transporter, GLUT-2.

N-Acetylglucosamine   Streptozotocin
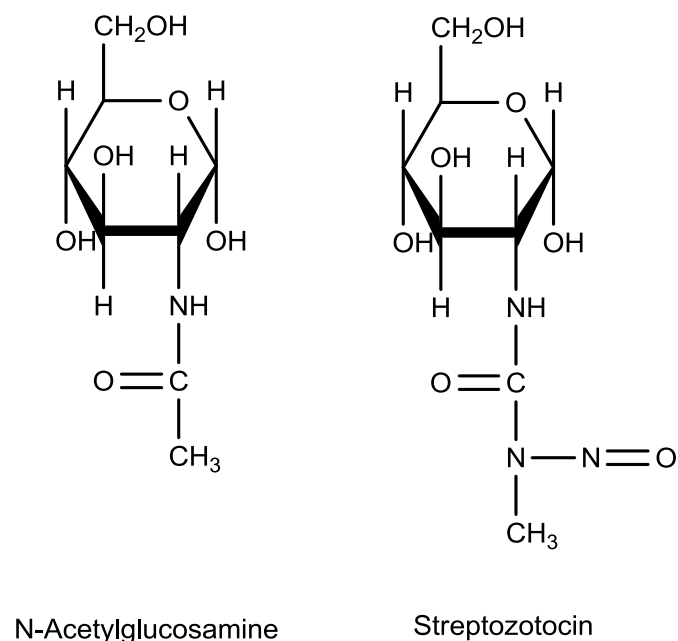
Figure 12. The chemical structure of GlcNAc and STZ

As shown in **Figure 13**, after entering β-cells, STZ induces DNA alkylation at the O^6 position of guanine by its nitrourea moiety[177, 178]. DNA alkylation further activates poly ADP-ribosylation [179] which further depletes cellular NAD (+) and ATP. Also, the islet mitochondrial aconitase activity is inhibited. As a result, the DNA of the β-cells is severely damaged[180]. The enhanced ATP dephosphorylation supplies the substrate of xanthine oxidase and leads to the production of superoxide radicals. Consequently, the oxidative stress induced by superoxide radicals, hydrogen peroxide and hydroxyl radicals further triggers β-cells apoptosis, leading to diabetes[181-184].
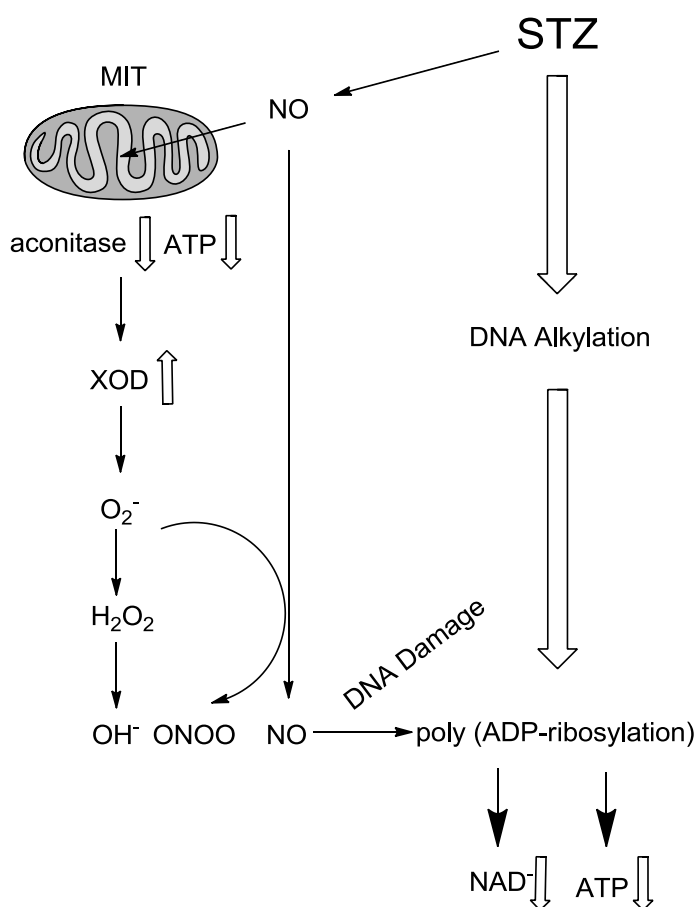
Figure 13.   The mechanism of streptozotocin (STZ)-induced diabetes which induced by the cytotoxic events in β-cells[172]. MIT: mitochondria; XOD: xanthine oxidase; NO: nitric oxide

CHAPTER THREE

TARGETING GLP-1R FOR NONINVASINVE ASSESSMENT OF BCM:

DESIGN AND EVALUATION OF GLP-1 ANALOGS (AIM 1)

In response to nutrient ingestion, naturally occurring GLP-1 is released from enteroendocrine L-cells of gastrointestinal tract and stimulates the insulin secretion in a glucose-dependent manner[185]. This phenomenon is called the incretin effect[186, 187], in which glucose-dependent insulinotropic polypeptide (GIP) also plays an important role. The incretin effect of GLP-1 is triggered by its specific binding to GLP-1R, which is specifically expressed on the pancreatic β-cells[143, 144] but not in human pancreatic α and δ cells[139](**Fig. 14**). Moreover, it has been found that both mRNA and protein levels of GLP-1R are downregulated on β-cells under the hyperglycemia condition[130]. Based on these two reasons, GLP-1 has the potential to develop as a molecular imaging probe especially to monitor the β-cell faith during diabetes. However, the main drawback for pursuing such goal is because of its short biological half life, which is not suitable for imaging application.
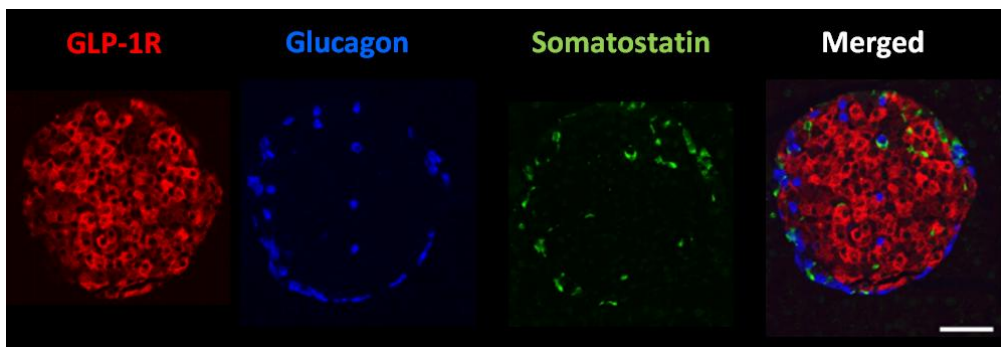
Figure 14. GLP-1R is not expressed in human pancreatic α and δ cells. Figure is adapted from Tornehave, D.[139]

The hypothesis of our work is: the expression level of GLP-1R on β-cells can serve as a surrogate of BCM for the noninvasive monitoring of diabetes progression. In order to noninvasively read out the GLP-1R expression in live subjects, a stable ligand system must be developed. In this part of my dissertation, this development is centered on the design and evaluation of novel GLP-1 analogs. Our research strategy is two-fold. We need: i) to develop a stable GLP-1 analog system without compromising the specific binding affinity to GLP-1R and ii) to minimize the nonspecific *in vivo* binding of the GLP-1 analogs in the surrounding tissues of pancreas.

3.1. Research Strategy

3.1.1. Development of a stable GLP-1 analog system without compromising the specific binding affinity of GLP-1 to GLP-1R

Endogenous GLP-1 undergoes a rapid degradation after being released from L-cells by peptidases, such as dipeptidyl peptidase-IV (DPP-IV) [188, 189]and neutral endopeptidase 24.11 (NEP 24.11) [190]. The biological half-life of GLP-1 is $2 - 3$ min in either rodents[131, 191, 192] or humans[133, 134]. Dipeptidyl peptidase-IV (DPP-IV) is a ubiquitous cell surface and circulating enzyme found in abundance at the brush border of kidney epithelium[193]. It is a serine protease that targets the substrates with Pro or Ala at the penultimate N-terminal position[194]. Consequently, it rapidly inactivates the endogenous GLP-1 by cleaving the peptide bond between Ala^8 and Glu^9 [131, 147] (**Fig. 14**) resulting degraded form of GLP-1 as shown in **Figure 15a**. To overcome the rapid metabolic degradation by DPP-IV, strategies have been reported including the substitution of Arg^{34} to Lys and addition a C16 acyl chain *via* a glutamoyl spacer to Lys^{26} as in liraglutide [195],

replacement of Ala8 and Gly35 with Aib (α-aminoisobutyric acid) as in taspoglutide[196] and glycosylation by sialyl LacNAc [197]. As the result, liraglutide has a plasma half-life between 10 and 14 h[195]. On the other hand, taspoglutide has improved the plasma half-life to 9.8 h[196]. In our work, we took a simple approach by substituting the L-Ala at 8th position to D-Ala to minimize the DPP-IV degradation.

Figure 15. Degradation sites of DPP-IV and NEP 24.11 on sequence of L-GLP-1

In addition to the DPP-IV degradation, GLP-1 is vulnerable to another peptidase, neutral endopeptidase 24.11 (NEP 24.11), which is also known as neprilysin. NEP 24.11 is a membranebound zinc metallopeptidase which targets a broad range of substrates. Specifically, it acts on the N-terminal side of aromatic or hydrophobic amino acids[198]. It is an enzyme with wide-spread distribution and particularly found in the kidney[199]. Hence, NEP 24.11 plays a critical role in the renal clearance of peptide hormones including GLP-1. In the GLP-1 sequence, NEP 24.11 targets multiple sites: Asp^{15}-Val^{16}, Ser^{18}-Tyr^{19}, Tyr^{19}-Leu^{20}, Glu^{27}-Phe^{28}, Phe^{28}-Ile^{29}, and Trp^{31}-Leu^{32} bonds[200] (**Fig. 15**) resulting fragmented metabolites. As shown in **Figure 16b**, more than 50% of L-GLP-1 was fragmented after 4 h incubation with NEP 24.11 and no intact L-GLP-1 was found after overnight incubation.
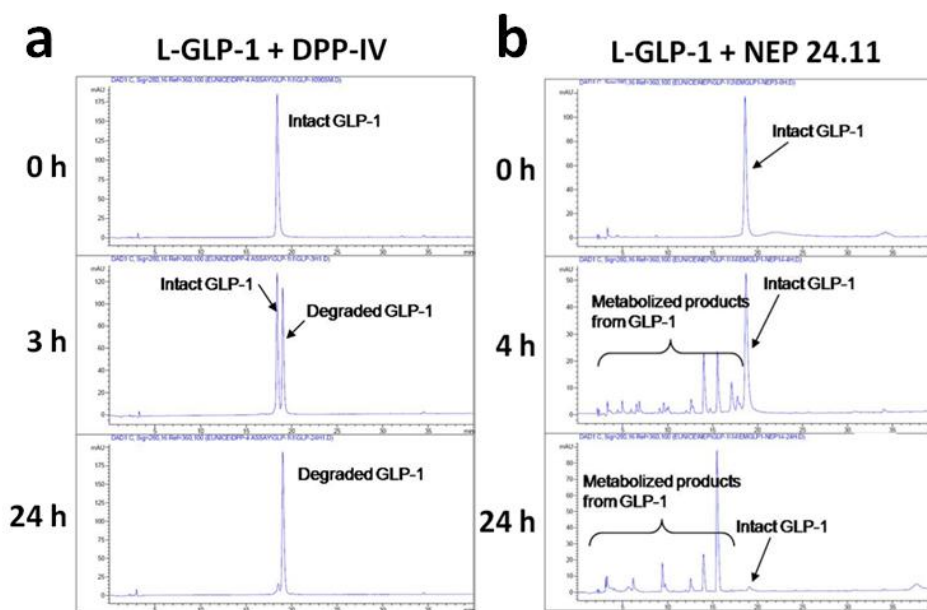
Figure 16. *In vitro* stability of L-GLP-1 against DPP-IV and NEP 24.11. The degraded of L-GLP-1 is observed after short period of incubation with either (a) DPP-IV or (b) NEP 24.11. No intact L-GLP-1 remains after 24 h of incubation. Reprinted from Murage E.N.,(2010). Copyright 2010 American Chemical Society.

Given that NEP 24.11 targets multiple sites in the GLP-1 sequence, several strategies were applied to enhance the enzymatic stability while maintaining the potency in our study. In the first design, GLP-1 analogs were introduced one, two, or three Glu^i/Lys^{i+4} lactam bridges at varies positions as conformational constraint to minimize the NEP 24.11 degradation[201]. The second design was replaced Ala^8 to D-Ala to avoid the DPP-IV degradation[202]. The other strategy was enhanced helicity by replacing certain amino acid residues with one, two, or three Aib molecules to stabilize the α-helix structure of GLP-1[203]. Based on the alanine mutagenesis study, placement of lactam bridge was avoided at the positions of 7, 10, 12, 13, 15, 28, and 29 which has the crucial role in maintaining receptor binding affinity[204]. Initially, the helicity and receptor potency were evaluated on four Glu^i/Lys^{i+4} or Lys^i/Glu^{i+4} lactam bridge positions: Val^{16}/Leu^{20}, Ser^{18}/Gly^{22}, Gly^{22}/Lys^{26}, and Ala^{30}/Lys^{34}, by circular dichroism (CD) spectroscopy and cAMP

levels measurement. As shown in **Table 5(a)**, Glu^i/Lys^{i+4} lactam bridge on Ser^{18}/Gly^{22} position (peptide: **2**) showed the most profound changes in both helicity and receptor potency whereas slightly increased in receptor potency was found on the placements of Val^{26}/Leu^{20} and Gly^{22}/Lys^{26}. In contrast, the reduced potency was observed when Glu^i/Lys^{i+4} lactam bridge placed on Ala^{30}/Lys^{34} (peptide: **4**). These results indicated the significance of N-terminal helix in receptor activation[201].

To achieve stronger interaction with the receptor, two lactam bridges were placed in the N- and C-terminal regions. Therefore, enhanced receptor potency was observed in the GLP-1 analogs with two lactam bridges. However, a negative effect on receptor potency was found when placing the reverse orientated lactam bridge (Lys^i/Glu^{i+4}) on α-helix region in N- and C-terminals (peptide: **r-1+4**). This might due to the lesser stability in α-helix regions that was provided by Lys^i/Glu^{i+4} lactam bridges. However, if the lactam bridge was placed on flexible region of GLP-1 sequence, the receptor potency would be rescued. This indicated that the flexible region constraint was the crucial for receptor activation (peptide: **r-2+4** and **r-3+4**).

Table 6. Receptor potency and enzymatic stability of GLP-1 analog with lactam bridge

Peptide	Sequence	Modification	(a) Receptor Potency		(b)NEP 24.11
			EC50 (nM)	(%)[a]	$t_{1/2}$ (h) [b]
L-GLP-1	HAEGTFTSDVSSYLEGQAAKEFIAWLVKGR	none	4.6	100	3.5±0.7
1	------------------E----K ---------------------------	Val16-Leu20	3.8	120	3.2±0.4
2	----------------------E----K---------------------	Ser18-Gly22	0.6	770	18±3.5
3	----------------------------E----K -------------------	Gly22-Lys26	2.8	160	4.7±0.5
4	--E----K ------	Ala30-Lys34	5.3	90	6.9±0.04
1+4	----------E----K -------------E----K-------	Val16-Leu20 Ala30-Lys34	3.3	140	9.7±1.9
2+4	------------------E----K------------E----K-----	Ser18-Gly22 Ala30-Lys34	1.9	240	>96
3+4	------------------------E----K-----E----K-----	Gly22-Lys26 Ala30-Lys34	1.6	290	3.6±0.9
r-1+4	----------K----E -------------K----E------	Val16-Lys22 Ala30-Lys34	7.0	70	18±5.0
r-2+4	------------------K----E------------K----E------	Ser18-Gly22 Ala30-Lys34	1.0	460	18±2.2
r-3+4	-------------------------------K----E-----K----E-----	Gly22-Lys26 Ala30-Lys34	2.2	210	1.2±0.3

E: Glutamic acid, K: Lysine   ⌐¬ : Glu^{i}/Lys^{i+4} lactam bridge. ⌐¬ :Lys^{i}/Glu^{i+4} lactam bridge
Area highlighted in yellow indicates the main α-helix conformation in the GLP-1 sequence. Underlined area indicates the critical location for receptor binding[204].
[a]Evaluation for the receptor potency compared to L-GLP-1. + indicates the enhancing receptor potency. – indicates the decreasing receptor potency.
[b] $t_{1/2}$: denotes 50% of GLP-1 analog degrades by the time (in hours) based on the area of the HPLC
Table is modified from Murage, E.N. et al.,[201]

To evaluate which lactam bridge locations in GLP-1 sequence can enhance enzymatic stability against NEP 24.11, GLP-1 analogs were incubated with recombinant NEP 24.11. The degradation profile of GLP-1 analogs was monitored using reverse phase high performance liquid chromatography (RP-HPLC). As shown in **Table 6(b)**, all of the GLP-1 analogs with single lactam constrant showed increasing tolerance against NEP 24.11, except peptide **1** displayed a similar stability as L-GLP-1. Interestingly, placement of Glu^i/Lys^{i+4} lactam bridge on Val^{16}/Leu^{20} position (peptide: **1**) showed similar stability against NEP 24.11 compared to L-GLP-1. Surprisingly, better stability was observed when shifting of lactam bridge placement from Val^{16}/Leu^{20} to Ser^{18}/Gly^{22} position (peptide: **2**).

GLP-1 analogs with double lactam bridge placed on Val^{16}/Leu^{20} and Ala^{30}/Lys^{34} (peptide: **1+4**) showed 3-fold increase and a minimal NEP 24.11degradation was observed when Glu^i/Lys^{i+4} lactam bridges were placed on Ser^{18}/Gly^{22} and Ala^{30}/Lys^{34} (> 96 h)(peptide: **2+4**). In contrast, there was no enhancement in stability observed if lactam bridge was placed on Gly^{22}/Lys^{26} (peptide: **3, 3+4**, and **r-3+4**). Hence, it further confirmed that the specific positioning lactam bridge on the GLP-1 sequence could enhance not only the receptor potency but also the enzymatic stability against NEP 24.11.

Based on these results, we further designed modification and evaluated the effect of α-helix conformation on receptor affinity and tissue distribution. Detailed placements of lactam bridge-modified GLP-1 candidates are summarized in **Table 7**. In addition to the lactam bridge design mentioned previously, the replacement of Ala8 with D-Ala was applied on the lactam bridge-based GLP-1 analogs.

In the second design, the α-aminoisobutyric acid (Aib) was introduced and replaced certain residue(s) to enhance the helicity of GLP-1. The selection of replacing residue was inspired by the design of taspoglutide which the Aib residues were located at 8th and 35th positions[203]. The Aib-modified GLP-1-based candidates are listed in **Table 8**.

Table 7. Lactam bridge-based GLP-1 analogs

Peptide	Sequence	Modification
L-GLP-1	HAEGTFTSDVSSYLEGQAAKEFIAWLVKGR	none
D-GLP-1	--A------------------------------	[d-Ala]
EM3110	--A----------E----K------------------	[d-Ala8],c[E16,K20]
EM4041	--A--------------------------E---K-----	[d-Ala8],c[E30,K34]
Isu-154	--A---------E---K----E----K------------	[d-Ala8],c[E16,K20],c[E22,K26]
BM2136	--A----------E---K-----E----K----------	[d-Ala8],c[E16,K20],c[E23,K27]
Isu-149	--A---------E--K--------E----K---------	[d-Ala8],c[E16,K20],c[E26,K30]
EM2131	--A---------E---K----------E---K-----	[d-Ala8],c[E16,K20],c[E30,K34]
BM2046	--A------------E----KE----K------------	[d-Ala8],c[E18,K22],c[E23,K27]
BM2035	--A----------E---K-----E---K----------	[d-Ala8],c[E18,K22],c[E26,K30]
EM2198	--A----------E--K-------------E---K----	[d-Ala8],c[E18,K22],c[E30,K34]
BM2125	--A----------E---K------------K----E---	[d-Ala8],c[E18,K22],c[K30,E34]
EM2198r	--A------------K----E--------K----E---	[d-Ala8],c[K18,E22],c[K30,E34]
EM2196	--A--------------------E---K-----E---K---	[d-Ala8],c[E22,K26],c[E30,K34]
EM4003	--A---------E---K----E---K-----E---K----	[d-Ala8],c[E16,K20],c[E22,K26],c[E30,K34]

E: Glutamic acid, K: Lysine, c: cyclization with lactam bridge, d-Ala: D form Alanine
⌐ :lactam bridge. . ⌐ :Lys^i/Glu^{i+4} lactam bridge
Area highlighted in yellow indicates the main α-helix conformation in the GLP-1 sequence. Underlined area indicates the critical location for receptor binding[204].

Table 8. Aib-based GLP-1 analogs

Peptide	Sequence	Modification
L-GLP-1	HAEGTFTSDVSSYLEGQAAKEFIAWLVKGR	none
EM4025	--A---	[Aib-8]
Aib 24	--------------------------------A----------------------	[Aib-24]
Aib 30	--------------------------------------A-------------	[Aib-30]
Aib 32	--A--------	[Aib-32]
Aib 33	---A------	[Aib-33]
Isu-166	--A--A------	[Aib-8] [Aib-33]
Isu-168	--A-------------------------------------A-----A------	[Aib-8] [Aib-30] [Aib-33]

Aib: α-aminoisobutyric acid

3.1.2 Radiolabeled GLP-1 analogs with ^{68}Ga for ex vivo PET imaging

3.1.2.1 Conjugation of the GLP-1 analog with NOTA moiety for ^{68}Ga labeling

To further evaluate the tissue distribution, GLP-1 analogs were designed to enable labeling of the GLP-1 analogs with radiometals. A cysteine handle was introduced to the C-terminal for further conjugation with bifunctional chelator. In order to conserve the binding affinity of the GLP-1 analogs, a spacer, aminohexanoic acid (ahx), was also introduced between the GLP-1 sequence and the cysteine handle. Maleimide-functionalized NOTA was synthesized from S-2-(4-isothiocyanatobenzyl)-NOTA ((S)-*p*-SCN-Bn-NOTA) due to their commercial availability. GLP-1 analogs were then conjugated with NOTA-maleimide through maleimide-thiol reaction *via* the free sulhydryl-group on the C-terminal (**Scheme 1**). The successful synthesis was verified by RP-HPLC. Purified NOTA-conjugated GLP-1 analogs was ready for ^{68}Ga labeling.
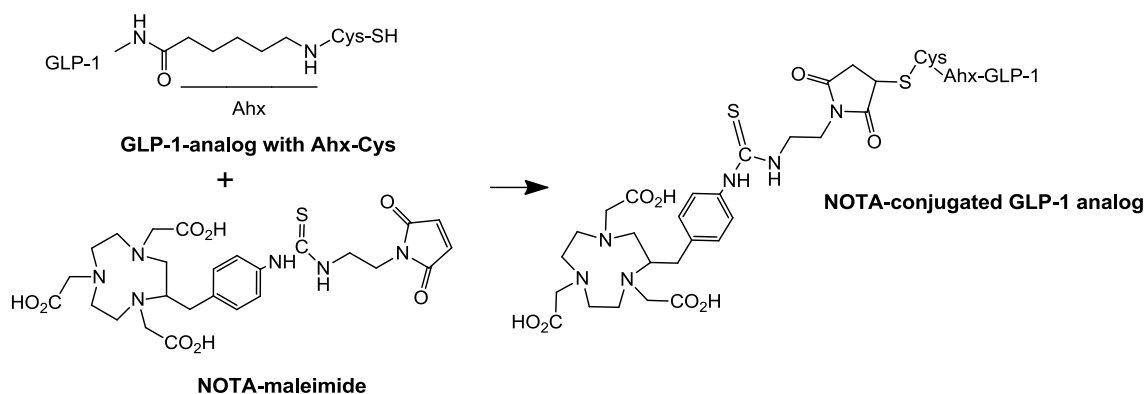
Scheme 1. Synthesis scheme of NOTA-conjugated GLP-1 analogs

3.1.2.2 ^{68}Ga labeling

In our study, ^{68}Ga^{3+} was eluted from a bench-top ^{68}Ga/^{68}Ge generator *via* acidic solution (0.6 N HCl) and it was in ^{68}GaCl$_3$ form. By adjusting the pH to 3-4, the NOTA-GLP-1 analogs were labeled at 75°C for 15 min (**Scheme 2**). Further separation was performed on a reverse phase cartridge and unlabeled ^{68}Ga^{3+} was removed from cartridge by passing through excess amount of H$_2$O. The labeled product was remained in cartridge until eluting with ethanol/saline solution (80% ethanol in saline). The product was then ready for study.
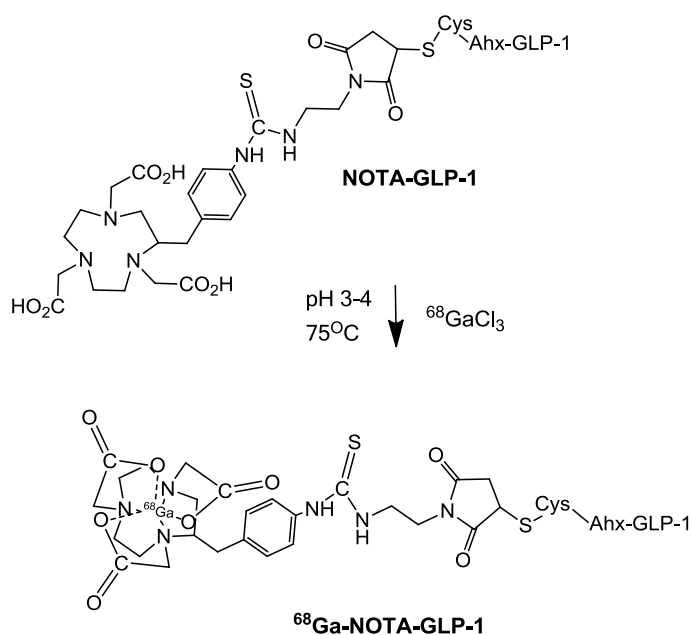
Scheme 2. Radiosynthesis of ^{68}Ga-NOTA-GLP-1 analog

3.1.3 Evaluation methods

3.1.3.1 Receptor binding assay for evaluation of receptor affinity

To evaluate the receptor affinity of the GLP-1 analogs, receptor binding assay is a straightforward technique. It is involved a labeled ligand and a targeted receptor. The ligand can be labeled in various ways such radiolabeling with an isotope (^{3}H, ^{125}I, or ^{35}S)[205-207] or tagged with a fluorescent moiety[208]. The receptor can be localized in a homogenized tissue, histological specimen, or in cultured cells that either have an endogenous expression of the receptor or have been transfected with a cloned receptor gene.

In the present study, GLP-R-positive cells were used as receptor source and the ^{125}I labeled GLP-1R agonist was served labeled ligand. To determine the two elements, receptor source and the labeled ligand, of the receptor binding assay, three GLP-1R positive cells and two ^{125}I-labeled ligands were evaluated. After evaluation of the binding assay conditions, series dilution of a GLP-1 analog was used to compete with ^{125}I-labeled ligand for binding with receptor. The labeled ligand bound and unbound fractions were then collected and radioactivity was detected by a gamma counter. The GLP-1R binding affinity of a GLP-1 analog was determined by sigmoidal curve fitting using the GraphPad Prism program (version 5.0, San Diego, CA) and expressed as half maximal inhibitory concentration (IC50).

3.1.3.2 *Ex vivo* PET scan for pancreas uptake of radiolabeled GLP-1 analogs

There were two rationales behind this study. The first one was to evaluate if a GLP-1 analog with higher *in vitro* receptor affinity can deliver better *in vivo* pancreas uptake. The second purpose was to evaluate which GLP-1 analog system can minimize the nonspecific *in vivo* binding of the GLP-1 analogs in the surrounding tissues of pancreas which would provide a better signal-to-noise ratio in the subsequent imaging study. For evaluation of the pancreas uptake level, normal C57BL/6 mice were administered i.v. with ^{68}Ga-labeled GLP-1 analogs. After 45 min post injection, animals were euthanized and the pancreas and adjacent organs were extracted, immediately scanned with a Siemens PET/CT scanner to evaluate the uptake level. The uptake level of a GLP-1 analog was determined by percentage of injected dose per gram (%ID/g) by Siemens Inveon workstation.

3.2 Results

3.2.1 Determination of the receptor binding assay condition

To be able to consistently evaluate the receptor affinity throughout the GLP-1 analogs, standard operating procedure (SOP) of the receptor binding assay was determined. Several key factors such as cell types, cell number, incubation duration, and labeled ligand were verified.

Firstly, due to the expression level of receptor varies from cell line to cell line, three types of cell lines including two insulinoma cells, INS-1 (rat) and β-TC6 (mouse) [209] which expressed endogenous GLP-1R and HEK293 cells (human embryonic kidney cells) which expressed human GLP-1R were used for the initial evaluation for the GLP-1R expression.Three cell lines were lysed and Western blotss was conducted. Based on Western blotss results (**Fig. 17**), the expression level of GLP-1R was similar. Even though β-TC6 cells showed slightly lower expression level of GLP-1R compared to INS-1 and HEK-293 cells, the difference was not significant.
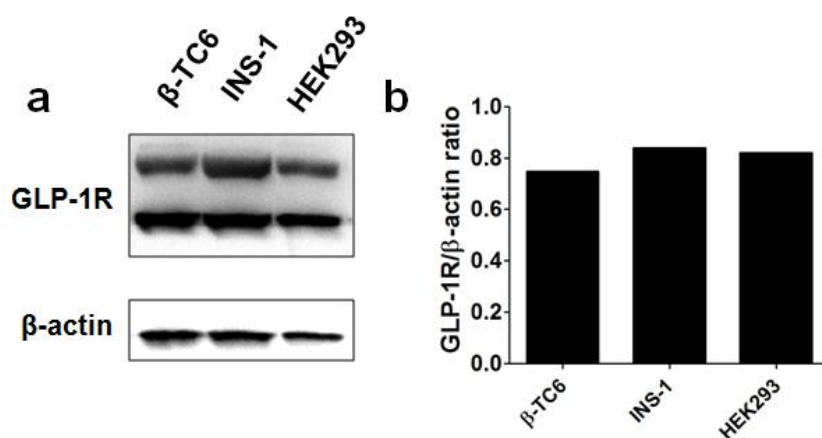
Figure 17. GLP-1R expression in β-TC6, INS-1, and HEK293-hGLP-1 cells. Representative Western blotss result of (a) GLP-1R and β-actin expression on β-TC6, INS-1 and HEK293-hGLP-1 cells. (b) The mean value of GLP-1R-to-β actin ratio.

Secondly, study was performed to determine the condition of the cell type and cell number along with incubation time. We used different cell numbers (0.125, 0.25, and 0.5×10^6) of all three cell lines and incubated with same amount of ^{125}I labeled exendin in 48-wells plate at 4°C. Bound and unbound fractions were collected after 4, 6, 8, and 12 h incubation. As expected, the higher uptake level was observed in higher cell number in all three cell lines. Among all three cell lines, the uptake level after 4 h incubation in INS-1 cell reached equilibrium stage but not in β-TC6 and Human Embryonic Kidney 293 (HEK293) cells. Surprisingly, β-TC6 cells showed significant higher binding level to ^{125}I-exendin compared to INS-1 and HEK293 cells (**Fig. 18**). Since all cell types have similar GLP-1R expression level, one possible explanation is the existing interspecies differences for the binding potential between exendin-4 and GLP-1R[210]. Further experiment should be done to explain the reason why β-TC6 cells showed 4 and 13 times higher uptake level compared to INS-1 and HEK293 cells.
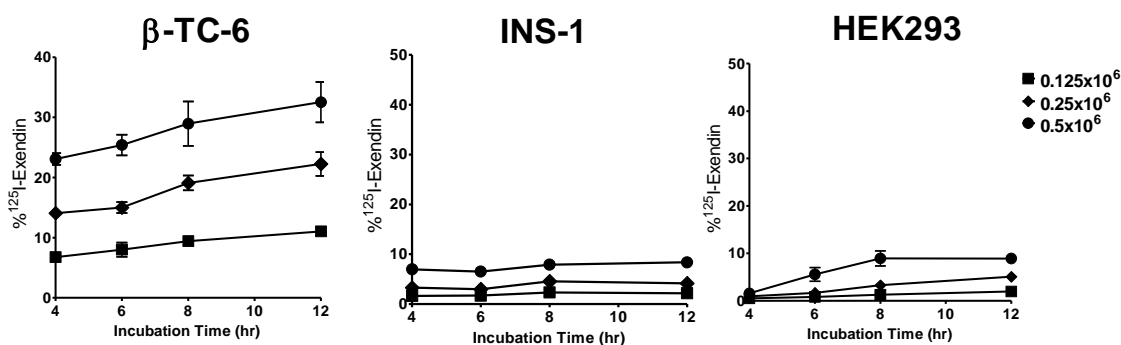
Figure 18. Binding potential of ^{125}I-exendin in β-TC6, INS-1, and HEK293 cells. Cell binding assay is performed under different cell number: 0.125, 0.25, and 0.5×10^6. (n = 3)

For the labeled ligand selection, we performed receptor binding assay based on the previous result. Half million of β-TC6 cells was used and incubated with either ^{125}I-exendin or ^{125}I-GLP-1 (Perkin Elmer) at 4°C for 4 h. Based on the specific activity provided by Perkin Elmer, the same concentration of radiolabeled ligands was used in the study. The binding potential of ^{125}I-exendin was 60% higher than ^{125}I-GLP-1 (**Fig. 19**). Hence, ^{125}I-exendin was selected as radioligand for the later receptor binding assay.
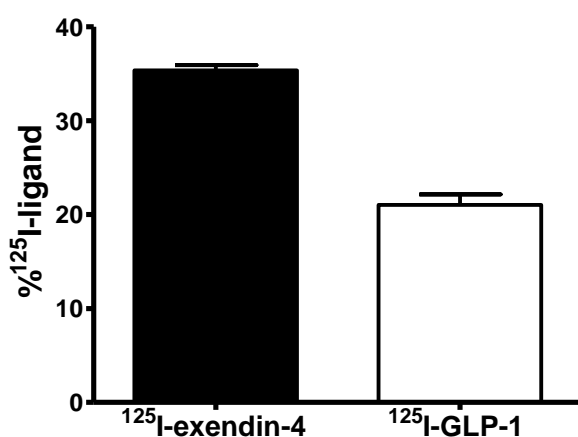
Figure 19. Binding potential of ^{125}I-exendin-4 and ^{125}I-GLP-1 in β-TC6 cells. Cell binding assay is performed with different radiolegands to evaluate the uptake level in β-TC6 cells. (n = 8).

3.2.2 Receptor binding assay

3.2.2.1 Receptor affinity of GLP-1 analogs with lactam bridge placement at Val^{16}/Leu^{20}

Five GLP-1 analogs with lactam bridge placement at Val^{16}/Leu^{20} including single bridge (EM3110) and double bridges (Isu-154, BM2136, Isu-149, and EM2131) were evaluated. EM3110 and EM2131 were not included in this evaluation with receptor binding assay due to the scheduled availability. With second lactam bridge on Gly^{22}/Lys^{26} (Isu-154) or

Gln^{23}/Glu^{27}(BM2136), a similar or better receptor affinity was observed compared to L-GLP-1. However, the receptor affinity was reduced when the second bridge in C-terminal α-helix region (Lys^{26}/Ala^{30})(Isu-149). This result indicated the placement of lactam bridge on flexible region of GLP-1 $(Gly^{22}-Gln^{23})$ might improve the receptor binding. This result was consistent to the previous receptor potency study (**Table 6**) and published results[211, 212].

3.2.2.2 Receptor affinity of GLP-1 analogs with lactam bridge placement at Ser^{18}/Gly^{22}

Four GLP-1 analogs with Ser^{18}/Gly^{22} lactam bridge including BM2046, BM2035, EM2198, and BM2125 were evaluated (EM2198r was not evaluated with receptor binding assay due to the scheduled availability) All of the GLP-1 analogs showed a similar or better receptor binding compared to L-GLP-1. By placing the lactam bridge on flexible region of GLP-1 $(Gly^{22}-Gln^{23})$, the receptor affinity was improved whereas the binding affinity was reduced when the second bridge is placed on Ala^{30}/Lys^{34} (EM2198). Interestingly, the receptor affinity was rescued when placing a switched orientated lactam bridge on Ala^{30}/Lys^{34} (BM2125). However, there was no complete conclusion for the effect of lactam bridge orientation to receptor binding affinity since the receptor binding affinity of EM2198r was not evaluated. Comparing to the lactam constraint on Val^{16}/Leu^{20}, GLP-1 analogs with lactam bridge on Ser^{18}/Gly^{22} showed better receptor binding affinity.

3.2.2.3. Receptor affinity of GLP-1 analogs with replacement of Aib

Seven GLP-1 analogs with Aib replacement including EM4025, Aib 24, Aib 30, Aib 32, Aib 33, Isu-166, and Isu-168 were evaluated. A mixed result was observed compared to L-GLP-

1. By replacing Aib on variable positions including Ala^8, Ala^{24}, Ala^{30}, Leu^{32}, and Val^{33}, the receptor affinity was improved when the Aib located at C-terminal α-helix region but not at the position close to flexible region of GLP-1 sequence. The receptor affinity was not improved by replacing multiple Aib residues.

3.2.3. *Ex vivo* PET scan for GLP-1 analogs to determine pancreas uptake

The *ex vivo* PET scans were used to determine which modifications of the GLP-1 analog system can provide maximal specific and minimal nonspecific binding of the GLP-1 analogs in pancreas and its surrounding tissues. For this purpose, GLP-1 analogs were labeled with a PET imaging isotope; ^{68}Ga. Native GLP-1 (L-GLP-1) was served as the control. Due to the availabilities of imaging schedule, three GLP-1 analogs were not included BM2136, BM2125, and EM2196.

3.2.3.1 Synthesis of NOTA-GLP-1 conjugates

For the labeling GLP-1 analogs with ^{68}Ga for *ex vivo* PET evaluation of pancrease uptake, NOTA-maleimide) was conjugated to the peptide, through a well-established maleimide-thiol reaction. NOTA-GLP-1 conjugates were obtained in high chemical yields (> 50 %) at pH 7 after reacting for 2 h at room temperature under inert atmosphere. All conjugates were then purified by a RP-HPLC and were further characterized by matrix-assisted laser desorption ionization-mass spectrometry (MALDI-MS)(**Table 9**).

Table 9. MALDI-MS characterization of NOTA-conjugated GLP-1 analogs

Peptide	calc'd m/z	found m/z
L-GLP-1	4104.00	4103.56
D-GLP-1	4104.00	4103.44
EM3110	4197.05	4196.85
EM4041	4144.02	4143.36
Isu-154	4185.03	4184359
BM2136	4113.01	4113.26
Isu-149	4171.00	4171.13
EM2131	4169.95	4169.55
BM2046	4181.17	4181.03
BM2035	4239.16	4239.54
EM2198	4237.05	4237.36
BM2125	4239..16	4239.23
EM2198r	4237.05	4237.55
EM2196	4236.20	4236.35
EM4003	4225.06	4225.13
EM4025	4118.03	4117.24
Isu-166	4104.00	4104.03
Isu-168	4118.00	4118.15

3.2.3.2 *Ex vivo* pancreas uptake of GLP-1 analogs with lactam bridge placement at Val^{16}/Leu^{20}

Five GLP-1 analogs with Val^{16}/Leu^{20} lactam bridge including single constraint (EM3110) and double constraint (Isu-154, Isu-149, and EM2131) were evaluated. BM2136 was not included due to the schedule availability. With second lactam bridge on Gly^{22}/Lys^{26} (Isu-154), Gly^{22}/Lys^{26}(Isu-149), Gln^{23}/Glu^{27}(EM2131) similar or worse pancreas uptake was observed compared to L-GLP-1. Even though Isu-154 showed much better receptor affinity compared to Isu-149, a similar low pancreas uptake was observed. Based on the current result, the placement of lactam bridge on Val^{16}/Leu^{20} affected not only the receptor binding affinity but also the pancreas uptake *in vivo*.

3.2.3.3 *Ex vivo* pancreas uptake of GLP-1 analogs with placement of lactam bridge at Ser^{18}/Gly^{22}

Four GLP-1 analogs with Ser^{18}/Gly^{22} lactam bridge including BM2046, BM2035, EM2198, EM2198r were evaluated. BM2125 was not evaluated due to the scheduled availability. Significant higher pancreas uptake was observed in all GLP-1 analogs compared to L-GLP-1. The pancreas uptake was not affected by the placement of the lactam bridge in this group. However, the nonspecific binding in liver was increased when the lactam bridge was placed on flexible region of GLP-1 (Gly^{22}-Gln^{23}) whereas the liver uptake was similar to L-GLP-1 when the second bridge was placed on Ala^{30}/Lys^{34} (EM2198). Interestingly, the liver uptake was increased when placing a switched orientated lactam bridge on both Ser^{18}/Gly^{22} and Ala^{30}/Lys^{34} (EM2198r). Surprisingly, this result was opposite to the receptor binding assay. Further study, such as

lipophilicity study to verify the cause of the nonspecific binding, should be done. Overall, comparing to the lactam constraint on Val^{16}/Leu^{20}, GLP-1 analogs with lactam bridge on Ser^{18}/Gly^{22} showed better pancreas uptake.

3.2.3.4 *Ex vivo* pancreas uptake of GLP-1 analogs with placement of triple lactam bridge

EM4003 was the only GLP-1 analog in this group. The design was to cover all three sections (N- and C- terminal α-helix and flexible region) on the GLP-1 sequence. The pancreas uptake was similar to EM3110 (single bridge on Val^{16}/Leu^{20}). However, the liver uptake was relatively high compared to L-GLP-1.

3.2.3.5 Receptor affinity of GLP-1 analogs with replacement of Aib

Three GLP-1 analogs with Aib replacement including EM4025, Isu-166, and Isu-168 were evaluated. A mixed result was observed compared to L-GLP-1. By replacing multiple Aib, the pancreas uptake was reduced which was consistent to the results of receptor binding affinity. Surprisingly, the high pancreas and low liver uptake was observed when Aib was replaced by Ala^{8} (EM4025).

Table 10. Screening of GLP-1 analogs by receptor binding affinity and *ex vivo* PET

Peptide	Sequence	IC50 (nM)	Ex vivo PET		
			Pancreas	Liver	Ratio
L-GLP-1	HAEGTF TSDVSSYLE GQ AAKEFIAWLVKGR	**7**	**0.4**	**1.2**	**0.33**
D-GLP-1	--A--	n.d.	0.6	0.7	0.86
EM3110	--A--------------E----K----------------------------	n.d.	0.8	n.d.	-
EM4041	--A----------------------------E---K-----	n.d.	0.3	n.d.	-
Isu-154	--A--------------E----K---E----K-------------------	**17.7**	0.4	n.d.	-
BM2136	--A--------------E----K---E----K-------------------	**4.01**	n.d.	n.d.	-
Isu-149	--A--------------E----K----------E----K------------	61.3	0.1	n.d.	-
EM2131	--A--------------E----K--------------E----K-----	n.d.	0.3	n.d.	-
BM2046	--A-------------------E----KE----K-----------------	**0.33**	**2.0**	4.0	0.50
BM2035	--A--------------E----K----E----K------------------	**0.71**	**1.7**	3.0	0.57
EM2198	--A--------------E----K---------E----K----	**11.2**	**1.7**	1.1	**1.53**
BM2125	--A--------------E----K--------K-----E----	**2.86**	n.d.	n.d.	-
EM2198r	--A--------------K----E--------K-----E----	n.d	**1.6**	2.4	0.67
EM2196	--A-------------------E----K----E----K--	n.d.	n.d.	n.d.	-
EM4003	--A--------------E----K---E----K-----E----K-----	n.d.	0.9	2.1	0.43
EM4025	--A--	**21.4**	1.5	0.7	**2.14**
Aib 24	-------------------------------A----------------------	81.2	-	-	-
Aib 30	--------------------------------------A--------------	**6.8**	-	-	-
Aib 32	--A----------	**14.3**	-	-	-
Aib 33	--A------	**11.4**	-	-	-
Isu-166	--A-----------------------------------A------	69.5	0.4	n.d.	-
Isu-168	--A-----------------------------------A-----A------	46.3	0.2	0.5	0.40

E: Glutamic acid, K: Lysine, c: cyclization with lactam bridge, d-Ala: D form Alanine
▢ :lactam bridge. . ▢ :Lys^i/Glu^{i+4} lactam bridge
n.d.: not determine. Area highlighted in yellow indicates the main α-helix conformation in the GLP-1 sequence. Underlined area indicates the critical location for receptor binding[204].

3.3 Evaluation of EM2198 Enzymatic Stability, Binding Affinity, Receptor Potency, Cellular Internalization, and Efflux

After screening with *ex vivo* PET imaging for pancreas uptake, EM2198 was one of the GLP-1 analogs which showed the great potential to develop as imaging probe. With two-fold modification strategies, EM2198 was expected to have high resistant to DPP-IV and NEP 24.11. To verify this assumption, we performed an *in vitro* assay to evaluate the enzymatic stability of EM2198 with the comparison to L-GLP-1. Both peptides were incubated at 37°C for over 96 h with either DPP-IV or NEP 24.11. At different time points, the sample was subjected for HPLC analysis.

As shown in **Figure 20**, EM2198 displayed much higher stability against either DPP-IV or NEP 24.11 than the native GLP-1 (L-GLP-1). It remained 96% intact within 24 h of incubation with DPP-IV (**Fig. 20a**). This increased stability can be simply attributed to the presence of D-Ala at 8th position instead of L-Ala. In contrast, 47% of L-GLP-1 was found degraded by DPP-IV within 2 h of incubation and there was only 9 % of intact peptide remained within 24 h. Furthermore, while L-GLP-1 showed a rapid degradation by NEP 24.11 (approximately 20% degraded within 2 h), less than 4% degradation was observed for EM2198 after 2 h of incubation with NEP 24.11 and over 61% of EM2198 was found intact even after 24 h (**Figs. 20b and 20c**). As expected, even after 96 h of incubation with DPP-IV or NEP 24.11, over 86% and 30% of EM2198 remained intact, respectively (**Fig. 20c**).
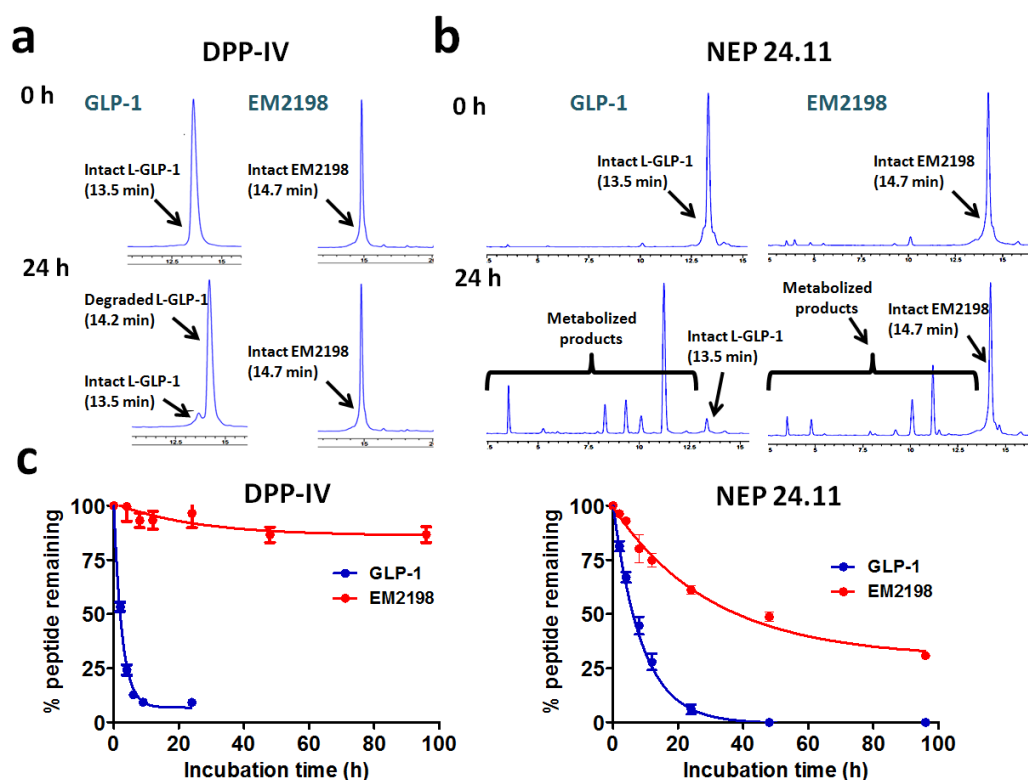
Figure 20. *In vitro* enzymatic stability assay of GLP-1 analogs. (a) HPLC chromatograms of GLP-1 and EM2198 after 0 and 24 h incubation with DPP-IV. (b) HPLC chromatograms of GLP-1 and EM2198 after 0 and 24 h incubation with NEP 24.11. (c) Comparative curve of enzymatic stability of GLP-1 and EM2198 against DPP-IV and NEP 24.11.

The receptor potency of EM2198 was determined by using stably transfected HEK293 cells overexpressing human GLP-1 receptors. Exendin-4 and L-GLP-1 were served as controls. Cyclic AMP accumulation by the GLP-1 analogues was measured in subconfluent cultures of the HEK293 cells in the presence of the phosphodiesterase inhibitor, 3-isobutyl-1-methylxanthine (IBMX), as previously reported[213]. For dose-response experiments, the HEK293 cells were treated with a peptide at various concentrations for 20 min at 37°C. After the reaction had been quenched with trichloroacetic acid, the produced cAMP was isolated by a two-column chromatographic method[214]. Results were analyzed by Prism 5.0 (GraphPad) and the 50% effective concentration (EC_{50}) was used to determine the receptor potency. As expected, exendin-

4 showed the best receptor potency with EC_{50} of 0.38 nM. Similar receptor potency of L-GLP-1 and EM2198 were observed with EC_{50} values of 2.94 nM and 5.70 nM, respectively.

We further performed *in vitro* cell-based receptor binding assays to determine if the modifications affected the binding affinity to GLP-1R. As the control, the native GLP-1 (L-GLP-1), scrambled EM2198, and exendin-4 were included in the assays. The binding assay was performed using GLP-1R-positive β-TC-6 insulinoma cells. EM2198 showed desired high GLP-1R binding affinity comparable to L-GLP-1 (**Table 11**) whereas the scrambled EM2198 showed no binding affinity. In addition, there was no significant change in the binding affinity after the introduction of the two lactam bridges and/or the C-terminus modifications (Ahx-Cys or Ahx-Cys-NOTA) or BFCs (NOTA or DOTA).

Table 11. Competitive receptor binding assay of GLP-1 analogs and controls

Peptide	Sequence and Modifications	IC_{50} (nM)
L-GLP-1	HAEGTFTSDVSSYLEGQAAKEFIAWLVKGR	9.7
EM2198 w/o d-Ala/linker	c[E18,K22]c[E30,K34]	2.4
EM2198 w/o linker	[d-Ala8],c[E18,K22],c[E30,K34]	5.2
EM2198	[d-Ala8],c[E18,K22],c[E30,K34], Ahx-Cys	11.2
NOTA-EM2198	[d-Ala8],c[E18,K22],c[E30,K34], Ahx-Cys ,NOTA	8.62
DOTA-EM2198	[d-Ala8],c[E18,K22],c[E30,K34], Ahx-Cys ,DOTA	2.65
sc-EM2198	DQVSKEARLEFEVWGKLTSIGAHEATYKEF-Ahx-Cys	N.B.
Exendin-4	HGEGTFTSDLSKQMEEEAVRLFIETLKNGGPSSGAPPPS	0.24

Ahx: aminohexanoic acid; d-: D-form; c: lactam bridge position; N.B.: no binding; sc-: scramble

To evaluate internalization and efflux of EM2198, an *in vitro* cell study was performed using β-TC6 cells. ^{67}Ga-labeled EM2198 was chosen because of the longer experimental time frame was needed. For the internalization study, cells were incubated with ^{67}Ga-NOTA-EM2198 at 37°C and harvested at 0, 15, 30, 45, 60, 90, 120, 360, and 1440 min. For the efflux study, cells were incubated with ^{67}Ga-NOTA-EM2198 at 37°C for 3 h before changing to the fresh binding medium. Supernatant was collected at 0, 15, 30, 45, 60, 90, 120, 360, 900, and 1440 min. As shown in **Figure 21**, the EM2198 was internalized and remained the similar level for the first 120 min, whereas the efflux rate of EM2198 stayed constant. This indicated the internalization and efflux were at the balance stage and the probe was not trapped inside of the cell. Interestingly, after 6 h the internalization suddenly increased while as the efflux reached equilibrium. This result might indicate that the probe was trapped after 6 h of incubation.
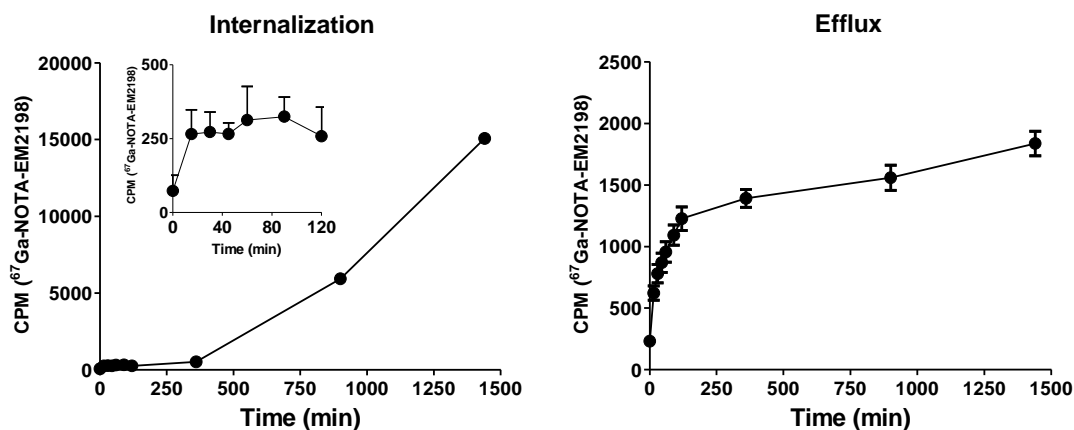
Figure 21. Internalization and efflux of EM2198

3.5 Conclusion

In the current design for a therapeutic GLP-1 analog, receptor potency and *in vivo* stability are the main focal points. Therefore, the introduction of either lactam bridge or Aib to enhance the receptor potency and stability against NEP 24.11by stabilizing α-helix conformation fits the main design concept. Based on screening results, GLP-1 analogs with the primary placement of lactam bridge on Ser^{18}/Gly^{22} showed better results on both receptor binding affinity and pancreas uptake. Good binding affinity was observed when adding a secondary lactam bridge on flexible region of GLP-1 sequence (BM2046 and BM2035). Nevertheless, this approach might not be suitable for designing an imaging GLP-1 analog due to increased nonspecific uptake in liver. On the other hand, EM2198, a GLP-1 analog with double lactam bridge on Ser^{18}/Gly^{22} and Ala^{30}/Lys^{34}, at first glance might not seem to be the best candidate for a favorable receptor binding affinity. Along with the superior enzymatic stability against both DPP-IV and NEP 24.11, EM2198 showed high specific uptake in pancreas and low non-specific uptake in liver which was much more suitable for imaging (**Table 10**). Moreover, compared to exendin-4, a widely used GLP-1R ligand, EM2198 showed 15 times less receptor potency. This result alone with good enzymatic stability indicated that EM2198 was much suitable to be developed as an imaging probe compared to exendin-4 because of the less biological reactivity. Therefore, EM2198 was chosen as a candidate for the further *in vivo* evaluations in Aim 2. In this part of dissertation, I finished the preliminary screening for the receptor affinity and *in vivo* pancreas uptake *via* standardized protocols. Although evaluations for several GLP-1 analogs were not complete, it might be feasible to select a potential GLP-1 analog for imaging based on the critical components.

CHAPTER FOUR

DEVELOPMENT OF PEPTIDE-BASED PROBES FOR BCM IMAGING (AIM 2)

Imaging probes of PET or SPECT derived from the naturally occurring peptide ligand of a specific cell membrane-bound receptor have potential to quantitatively measure the receptor's expression level *in vivo*. However, the biological action of a peptide hormone on its specific receptor is often a transient response to a stimulant. As the result, endogenous peptide ligands are short-lived to avoid the otherwise persistent stimulation; they are degraded by their corresponding peptidases soon after the stimulant diminishes. To develop peptide-based imaging probes, such instability should be addressed under the prerequisite condition that the peptide level is not able to incur the corresponding biological actions of its receptor. The sensitivity of PET or SPECT imaging technique is capable of meeting this prerequisite. As such, the effort of peptide-based imaging probe development is more on the selection and modification of proper peptides aimed to achieve the desired high stability without compromising their specific receptor binding affinity. In other words, within the imaging window of a biological event, the imaging probe must have the anticipated stability to faithfully read out the interrogated biological event.

Specifically in this dissertation, our goal is to target GLP-1R as the surrogate biomarker for noninvasive assessment of BCM. The GLP-1 analogs of our selection for BCM imaging must be stable in order to measure the expression of GLP-1R on β-cells. As shown before, EM2198, a GLP-1 analog stabilized with lactam bridges on Ser^{18}/Gly^{22} and Ala^{30}/Lys^{34} positions indeed showed the most promising results in GLP-1R binding and pancreas targeting through our

screening process. Therefore, EM2198 was chosen to be developed as an imaging probe of BCM in this dissertation. Given the imaging mechanism is based on the specific interaction between the GLP-1 and GLP-1R pairs, EM2198 must be radiolabeled at high specific activity in order not to elicit the biological actions of GLP-1 action. In the meantime, a higher binding affinity is always desired to further enhance the imaging sensitivity. To date, the multivalent effect has become a well-accepted concept when amplification of imaging signal of the targeted receptor is necessary[215]. As reported previously[216], we had designed NOTA-based multivalent scaffolds with ligands targeting integrin $\alpha_v\beta_3$ and showed promising results in the enhancement of binding affinity. Hence, multimerization of EM2198 on this BFC scaffold was also tested to further enhance its binding to GLP-1R and optimize the *in vivo* kinetics of the EM2198-based probes.

Two goals were set in this part of research. We aimed 1) to evaluate the biological behavior of EM2198 through biodistribution and pharmacokinetic experiments using radiolabeled-EM2198 in an animal model and 2) to optimize the *in vivo* kinetics of EM2198-based imaging probes by multi-presentation of EM2198 on a common scaffold.

4.1 Research Strategy

4.1.1 In vivo evaluations of EM2198

In vivo evaluations of EM2198 were performed including *in vivo* stability in blood, biodistribution, and pharmacokinetic. Due to the longer duration required for these evaluations than in the early screening, longer lived radioisotopes, ^{64}Cu ($t_{1/2}$ = 12.7 h) and ^{67}Ga ($t_{1/2}$ = 3.26 days), were used instead of ^{68}Ga ($t_{1/2}$ = 68 min). Specifically, ^{67}Ga-labeled NOTA-EM2198 was

used in the pharmacokinetic evaluation and ^{64}Cu-labeled DOTA-EM2198 for biodistribution and *in vivo* metabolism studies.

4.1.1.1 Pharmacokinetic study of ^{67}Ga-NOTA-EM2198

The pharmacokinetic profile of EM2198 was evaluated by using ^{67}Ga-NOTA-EM2198. C57/BL6 mice were i.v. injected (10μCi) with ^{67}Ga-NOTA-EM2198. Blood samples were collected and weighed for up to 24 h. Radioactivity of the sample was counted by a calibrated γ counter. The quantitative uptake in the blood was calculated as the percentage of injected dose per gram (%ID/g) of blood.

4.1.1.2 Biodistribution and metabolism studies

^{64}Cu was chosen for the biodistribution study, because of the longer time points were required. Therefore, we modified the GLP-1 analog by placing a DOTA chelator at the C-terminus of the peptide which was subsequently radiolabeled with ^{64}Cu. For the biodistribution study, the ^{64}Cu-labeled EM2198 or L-GLP-1 was injected intravenously (10 μCi) into BALB/c mice. To evaluate of GLP-1R binding specificity, a blocking study was performed by co-injection of a GLP-1R agonist, exendin-4, along with ^{64}Cu-DOTA-EM2198. Animals were sacrificed at selected time points. Blood and organs were collected, weighed, and counted by a γ-counter. The quantitative uptake in tissues of interest was calculated as %ID/g.

In vivo stability in blood was conducted at 1 and 4 h p.i of ^{64}Cu-labled peptides. Samples were homogenized and analyzed by radio-HPLC. The metabolic fate of ^{64}Cu-DOTA-EM2198 was determined by the changes of the corresponding HPLC peaks.

4.1.2. Further enhancement of GLP-1R binding affinity and optimization of the in vivo kinetics of GLP-1 analogs by multi-presentation of a GLP-1analog on the NOTA-BFC scaffold (Scheme 3)

4.1.2.1 Multimeric EM2198 on NOTA scaffold

Recently, a multivalent NOTA scaffold system was designed and conjugated with an integrin $\alpha_v\beta_3$ ligand, (c(RGDyK))[216]. As expected, the binding affinity was dependent on the valency of conjugates. The *in vivo* behavior of ^{68}Ga-labeled NOTA conjugates with mono-, di-, tri-valent presentations of c(RGDyK) was evaluated in Severe combined immunodeficiency (SCID) mice bearing an integrin $\alpha_v\beta_3$-positive PC-3 prostate cancer xenograft. Accumulation in tumor varying with the valence was observed 2 h after injection of the probes. The same design was applied to the development of EM2198-based imaging probes. As shown in **Scheme 3**, the synthesis of EM2198 conjugates can be achieved in three steps, namely: 1) synthesis of *t*butyl-protected BFC scaffolds, NOTA ^{t}Bu$_3$-COOH, NOTA ^{t}Bu$_3$-(COOH)$_2$ and NOTA ^{t}Bu$_3$-(COOH)$_3$, *via* our previously reported procedures[217], 2) formation of the maleimide derivatives: NOTA ^{t}Bu$_3$-Mal, NOTA ^{t}Bu$_3$-(Mal)$_2$ and NOTA ^{t}Bu$_3$-(Mal)$_3$, and 3) conjugation of the EM2198 to the synthesized maleimide derivatives, followed by deprotection of the α-carboxylate groups to provide the final conjugates. Conjugates were labeled with ^{68}Ga at 75°C for 15 min. Radiochemical yield and purity was determined by instant thin layer chromatography (iTLC) and radio-HPLC, respectively. The preliminary evaluation of the probes was performed on normal C57/BL6 mice by PET imaging.

R= (structure: propanoic acid) OH, O

NOTA $^tBu_3$-COOH: $X_1 = R$, X_2, $X_3 = H$, $X_4 = {}^tBu$
NOTA $^tBu_3$-(COOH)$_2$: X_1, $X_2 = R$, $X_3 = H$, $X_4 = {}^tBu$
NOTA $^tBu_3$-(COOH)$_3$: X_1, X_2, $X_3 = R$, $X_4 = {}^tBu$

H_2N (maleimide) | EDC, Et$_3$N
DMF

NOTA $^tBu_3$-Mal: $X_1 = R$, X_2, $X_3 = H$, $X_4 = {}^tBu$
NOTA $^tBu_3$-(Mal)$_2$: X_1, $X_2 = R$, $X_3 = H$, $X_4 = {}^tBu$
NOTA $^tBu_3$-(Mal)$_3$: X_1, X_2, $X_3 = R$, $X_4 = {}^tBu$

R= (amide-maleimide structure)

PBS | HS·Cys-EM2198

NOTA $^tBu_3$-EM2198: $X_1 = R$, X_2, $X_3 = H$, $X_4 = {}^tBu$
NOTA $^tBu_3$-(EM2198)$_2$: X_1, $X_2 = R$, $X_3 = H$, $X_4 = {}^tBu$
NOTA $^tBu_3$-(EM2198)$_3$: X_1, X_2, $X_3 = R$, $X_4 = {}^tBu$

R: EM2198

R= (amide-succinimide structure) S·Cys-EM2198

TFA

NOTA-1A-EM2198: $X_1 = R$, X_2, $X_3 = H$, $X_4 = H$
NOTA-2A-(EM2198)$_2$: X_1, $X_2 = R$, $X_3 = H$, $X_4 = H$
NOTA-3A-(EM2198)$_3$: X_1, X_2, $X_3 = R$, $X_4 = H$

Scheme 3. Synthetic route to multimeric peptide conjugates

4.2 Results

4.2.1 Radiochemistry of ^{67}Ga-NOTA-GLP-1 analog

For the radiosynthesis of ^{67}Ga-NOTA-EM2198, NOTA-conjugated EM2198, synthesized as described earlier, was labeled with ^{67}GaCl$_3$. Unlike ^{68}Ga which is produced through a ^{68}Ga/^{68}Ge generator, ^{67}Ga is purchased from commercial source (Nordion) which is produced in a cyclotron by proton irradiation of enriched zinc. The labeling of the compound was performed under the

same labeling and purification conditions as those used for ^{68}Ga. In details, ^{67}Ga was diluted with 0.6N HCl and pH was adjusted to 3.0 by adding 1M HEPES. Radiochemical yield of ^{67}Ga-NOTA-EM2198 was 8.4-27.2% and the specific activity was up to 18 GBq/μmol. Compared to the radiosynthesis results for ^{68}Ga-NOTA-EM2198, both radiochemical yield and specific activity were significant lower. This might be due to the high content of Zn^{2+} (30 ppm) and Fe^{3+} (4 ppm) impurities in the ^{67}GaCl$_3$ solution[218]. Due to the increased amount of impurities, the purification of ^{67}Ga is crucial prior to the radiolabeling to enhance the specific activity of ^{67}Ga-NOTA-EM2198. As purification method, extraction with isopropyl ether/HCl was used. As a result, the radiochemical yield and specific activity increased to 85% and 173 GBq/μmol, respectively. The radiochemical purity (RCP) was further evaluated by radio-HPLC. The minimal RCP of ^{67}Ga-NOTA-EM2198 was maintained over 97% for the *in vivo* pharmacokinetics study.

4.2.2. Synthesis of DOTA-GLP-1 analogs for biodistribution study (Scheme 4)

For the biodistribution study, DOTA-EM2198 and DOTA-L-GLP-1- conjugates were synthesized through a well-established maleimide-thiol reaction. The EM2198 and L-GLP-1 conjugates were obtained in high chemical yields (~60 %) after reacting for 2 h at room temperature under inert atmosphere. Both conjugates were then purified by RP-HPLC and were further characterized by matrix-assisted laser desorption ionization-mass spectrometry (MALDI-MS)(**Table 12**). The receptor affinity of DOTA-conjuagated EM2198 was evaluated by receptor binding assay. The IC$_{50}$ value of DOTA-EM2198 (2.65 nM) was similar to the nonconjugated EM2198 (11.2 nM).
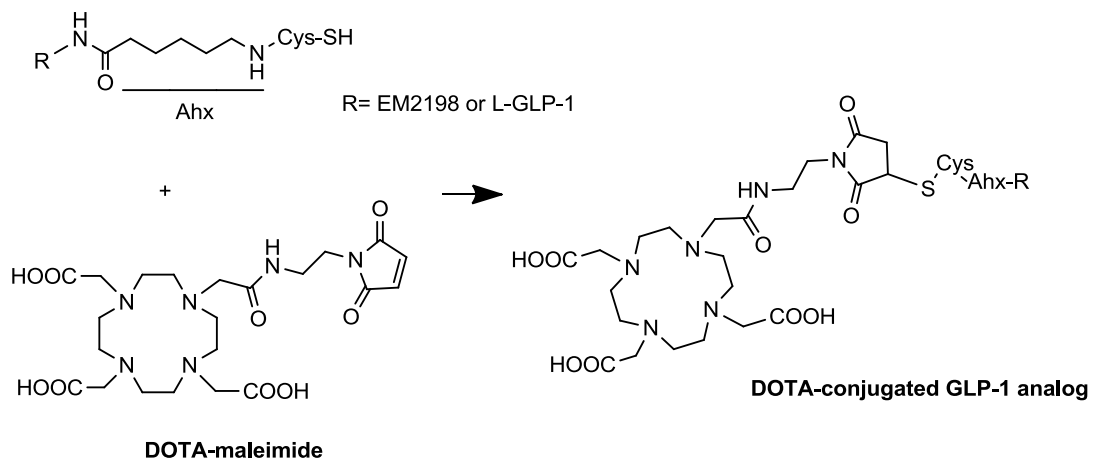
Scheme 4. Synthesis of DOTA-GLP-1 conjugates

Table 12. MALDI-MS characterization of the DOTA-conjugates of GLP-1 analogs

Peptide	calc'd m/z	found m/z
DOTA-EM2198	4175.70	4175.72
DOTA-L-GLP-1	4040.55	4040.60

4.2.3. Radiochemistry of ^{64}Cu-DOTA-conjugated EM2198 and L-GLP-1 (Scheme 5)

For the radiosynthesis of ^{64}Cu-DOTA-GLP-1, different concentrations of the GLP-1 conjugate were incubated with ^{64}Cu at 37°C to determine the more efficient labeling conditions. It was found that both DOTA-EM2198 and L-GLP-1 were successfully labeled at concentration ≥ 5

µM in 0.1 M ammonium acetate (pH 6.5) with high labeling efficiencies (> 80%). Radiochemical yields of ^{64}Cu-DOTA-GLP-1 conjugates were over 75% and the specific activity up to 100 GBq/µmol. The separation and purification were performed efficiently through Sep-Pak C-18 cartridge. The radiochemical purity (RCP) was further evaluated by radio-HPLC. The minimal RCP of ^{64}Cu-DOTA-EM2198 and L-GLP-1was maintained at over 97% for all *in vitro* and *in vivo* studies.
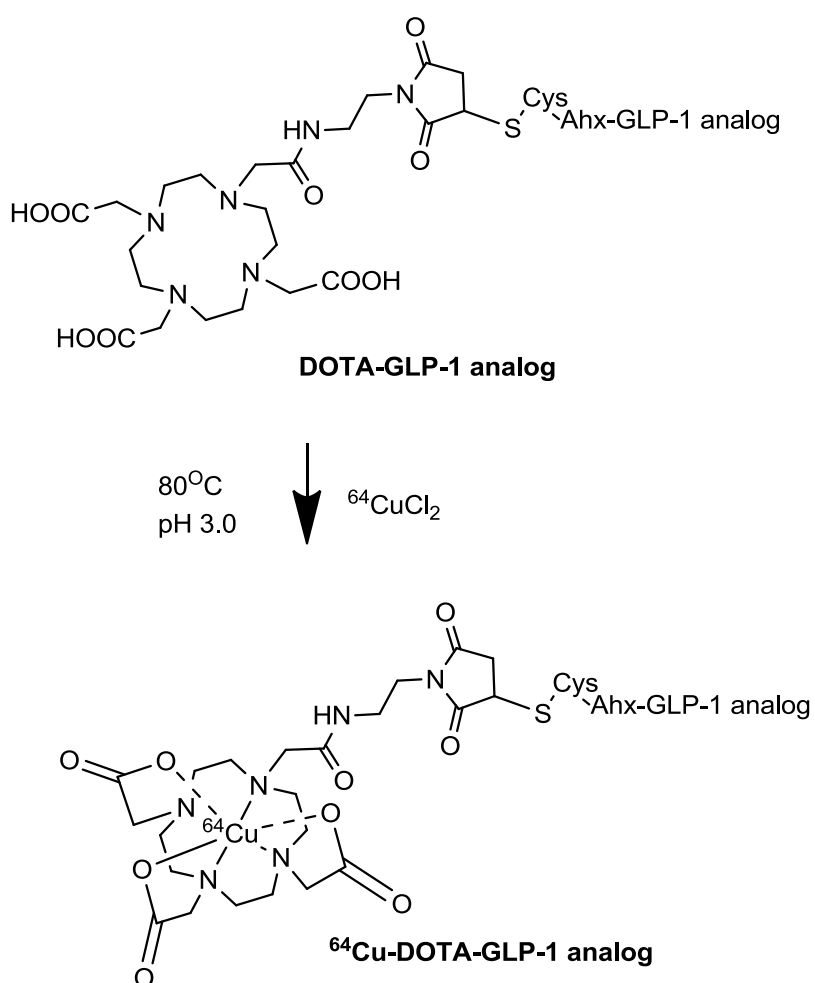
Scheme 5. Radiosynthesis of ^{64}Cu-DOTA-GLP-1 analog

4.2.4 Pharmacokinetics

In vivo pharmacokinetics studies of EM2198 were performed in normal C57/BL6 mice (n=3). Blood samples were collected for up to 24 h after a single i.v. bolus injection of 10 μCi of ^{67}Ga-NOTA-EM2198. As shown in **Figure 22a-d**, a two-compartment open model was used to calculate the distribution half-life ($t_{1/2\alpha}$) and the elimination half-life ($t_{1/2\beta}$). The linear regression showed the best and reasonable fit for both α and β phases (**Fig. 22b and c**). The average of $t_{1/2\alpha}$ and $t_{1/2\beta}$ were 28.2 min and 565.7 min, respectively.
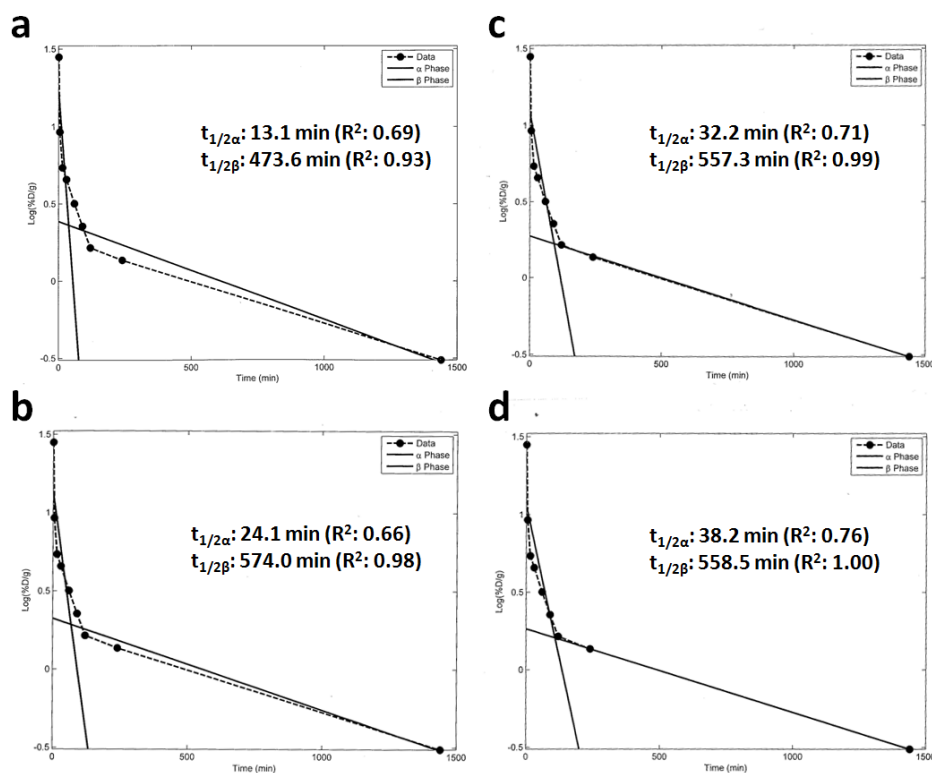
Figure 22. Logarithms of the concentrations versus time for the pharmacokinetic evaluation of ^{67}Ga-NOTA-EM2198. Curve fitting with (a) 4, (b) 5, (c) 6, and (d) 7 points for the α phase.

4.2.5 Comparative biodistribution of EM2198 and L-GLP-1

The comparative biodistribution data are summarized in **Figure 23**. Both ^{64}Cu-labeled DOTA-EM2198 and DOTA-L-GLP-1 showed extremely high uptake in the kidneys, along with small uptake in the lung and liver. ^{64}Cu-DOTA-EM2198 showed 2.5-fold higher accumulation in the pancreas compared to ^{64}Cu-DOTA-L-GLP-1 (EM2198: 4.9 %ID/g; L-GLP-1: 2.0 %ID/g). The accumulation of ^{64}Cu-DOTA-EM2198 in pancreas was specific to the same target as the GLP-1R agonist, exendin-4, as verified by a blocking study in reducing uptake levels in the pancreas and lung. Because of exendin-4 carries -1.9 of net charge which is higher than EM2198 (-0.9), the renal uptake was also reduced significantly (p < 0.0001) in the blocking group. As a result, the activity balance in the blocking group was different than those of ^{64}Cu-labeled DOTA-L-GLP-1 and DOTA-EM2198 with higher uptake in blood, heart, muscle, and fat. ^{64}Cu-labeled DOTA-L-GLP-1displayed relatively low accumulation in the pancreas which may be caused by its lower *in vivo* stability compared to EM2198 (**Fig. 23**).
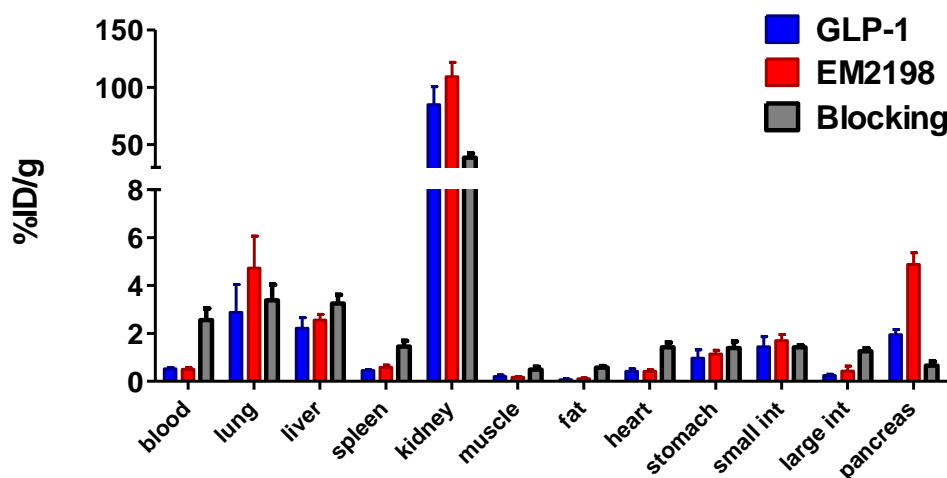
Figure 23. Comparative biodistribution data of ^{64}Cu-DOTA-EM2198, ^{64}Cu-DOTA-L-GLP-1, and ^{64}Cu-DOTA-EM2198 co-injected with a blockade dose of exendin-4.

4.2.6 Stability of EM2198 in blood

The *in vivo* stability of EM2198 in blood was evaluated in normal BALB/c mice by HPLC analysis of the extracts from blood at 1 and 4 h post-injection (p.i.) (**Figure 24**). EM2198 showed high stability comparable to that of exendin-4 in the blood within 4 h, whereas the GLP-1 analog having only Ala8 modified was totally degraded.
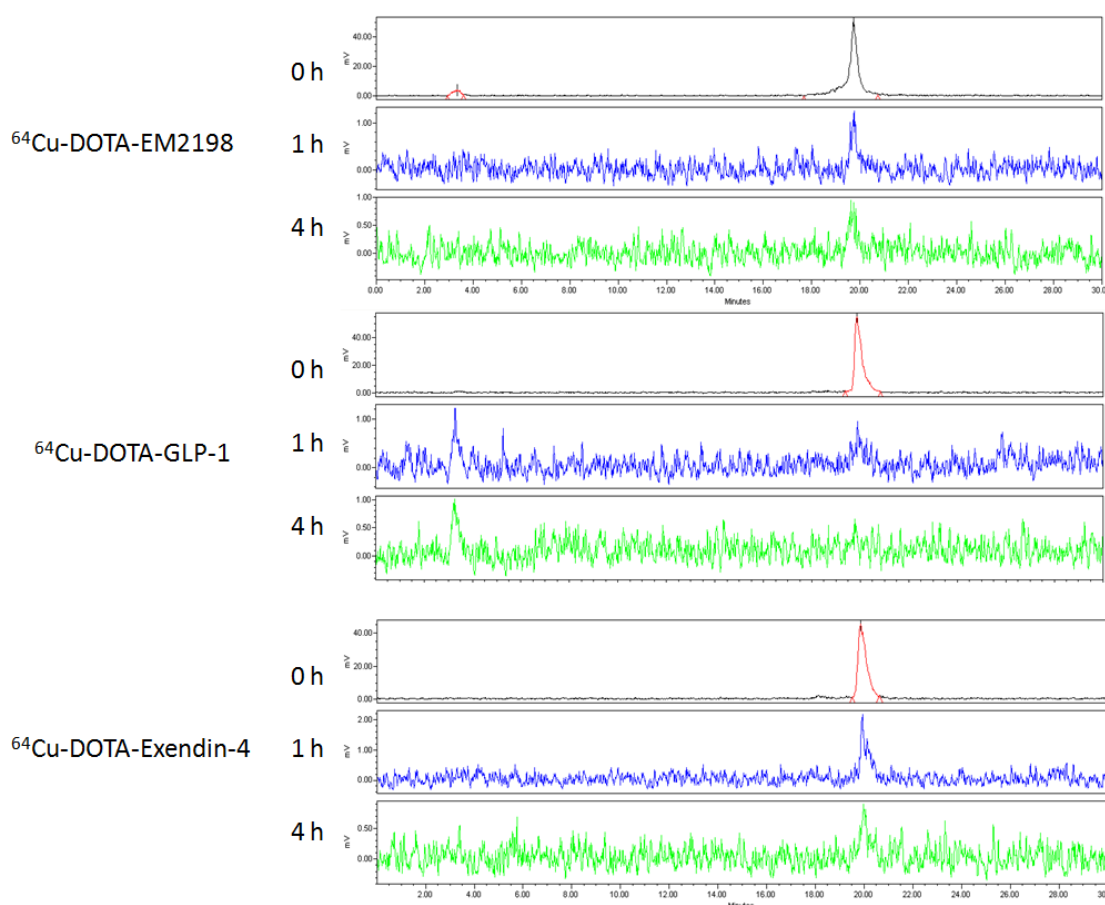
Figure 24. *Ex vivo* stability of GLP-1 analogs and exendin-4 in blood. HPLC chromatograms of ^{64}Cu labeled peptides extracted from the mouse blood at 1 and 4 h post-injection. The retention time of the control is at 20 min. The units of y-axis and x-axis are mV and min.

4.2.7 Renal uptake of radiolabeled EM2198

Based on the results of the biodistribution study, the excretion of radiolabeled EM2198 occurs mainly through kidneys. This observation has been also seen in both therapeutic and diagnostic[219] peptide-based radiopharmaceuticals. Kidneys are the organs susceptible for the dose-limiting toxicity due to the renal tubular reabsorption resulting in the retention of radiolabeled peptide in renal cortex. As a result, the high radiation dose in peptide-receptor radionuclide therapy (PRRT) can cause irreversible loss of function in kidney such as radiation nephritis[220]. Therefore, studies have used gelatin-based plasma expander (Gelofusin, GELO: 4% succinylated gelatine in 0.7% saline)[221], cationic amino acid [222], poly-glutamic acid (PGA), and albumin-derivatives[223] to block the negative charged tubular cell surface. Indeed, the selective reduction effect has been seen in ^{111}In-octerotide and other radiolabeled peptides. For instance, the renal uptake of octreotide can be reduced by Gelofusin and lysine but not PGA, while Gelofusin and PGA can efficiently reduce the renal uptake of ^{111}In-labeled exendin-4 but not lysine[224]. Based on the differences in renal uptake reduction between PGA and lysine, the kidney uptake mechanism might be relevant to the total charge of a molecule. The level of the renal radiation toxicity is also a factor of the physical decay properties of the radioisotope, the type and the half life of radioactive decay. Isotopes, such as ^{64}Cu or ^{68}Ga, used in our PET studies, have relatively short half-life compared to the generally used isotopes in PRRT such as ^{90}Y ($t_{1/2}$ = 2.67 d) and ^{177}Lu ($t_{1/2}$ = 6.73 d). However, the high renal uptake constitutes a problem because of the close proximity of the pancreas to the kidneys in mice. The spillover radioactivity from the kidneys might affect the imaging quantification of pancreas. Hence, it is necessary to implement a method suitable for our imaging probe in the imaging protocol. For convenience, L-lysine was used for the renal uptake reduction in the initial evaluation of ^{68}Ga-labeled NOTA-EM2198.

Thirty minutes prior to the administration of ^{68}Ga-NOTA-EM2198, mice were i.p. injected with a single, double, or triple dose of 400 mg/kg L-lysine or saline as control[225]. Summarized in **Figure 25,** the results showed a dose-effect relationship between i.p. administered L-lysine and the kidneys' uptake. As expected, with the double-dose administration of L-lysine, the maximum kidney uptake was reduced by ~29 %, from 45.5±0.3 % ID/g to 32.1±0.1 %ID/g, in the control animals (p < 0.0001). Similar yet not greater renal uptake reduction was observed in mice with triple dose injection of L-lysine. Based on the *ex vivo* PET imaging, the pancreas uptake was not affected by the L-lysine administration. Compared to a published report[224], we used a different animal model, dosage, and evaluation method. However, the likelihood for clinical implementation of using such method was limited due to the increasing risk of acute tubular necrosis by administration of high concentration L-lysine[226]. Most likely, it is not necessary for including L-lysine administration in clinical imaging study since the location of kidneys is distal from the pancreas in human.
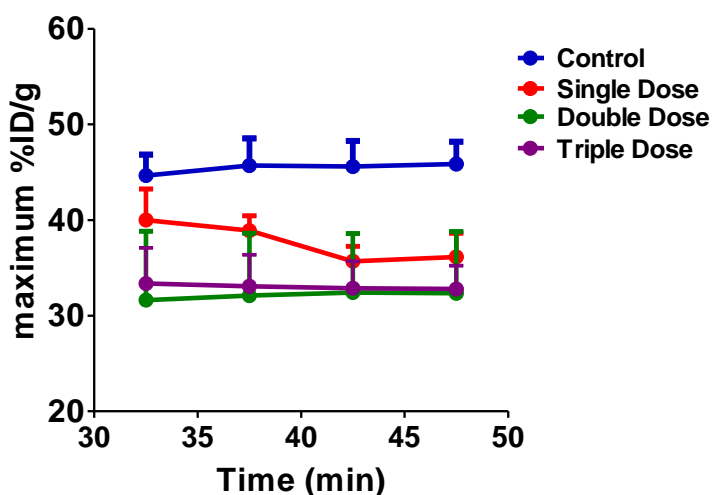
Figure 25. Time activity curves of kidney with or without L-lysine administration (i.p.). The control was administered with saline. A single dose of L-lysine was 400 mg/kg L-lysine (n = 3).

4.2.8 Optimization of the in vivo kinetics of the GLP-1 analogs by multi-presentation of GLP-1analogs on a common scaffold

To optimize the *in vivo* kinetics of the EM2198-based imaging probe, we envisioned to develop imaging probes with multiple EM2198 units on a single scaffold. As such we aimed to enhance the receptor affinity and further increase the probe sensitivity. First, we synthesized mono-, di-, or trivalent functionalized NOTA scaffolds. The chemical yields of the BFC scaffolds: NOTA $^tBu_3$-Mal, NOTA $^tBu_3$-(Mal)$_2$ and NOTA $^tBu_3$-(Mal)$_3$ were 65%, 45%, and 31%, respectively. The obtained maleimide intermediates, were conjugated with one, two or three equivalents of EM2198 through a well established thiol-maleimide reaction to provide NOTA (^tBu)$_3$-EM2198, NOTA (^tBu)$_3$-(EM2198)$_2$, and NOTA (^tBu)$_3$-(EM2198)$_3$ respectively. The final products were obtained after deprotection of the *t*-butyl groups of the above conjugates using TFA (95%). All conjugates were then purified by RP-HPLC and were further characterized by matrix-assisted laser desorption ionization-mass spectrometry (MALDI-MS)(**Table 13**).

All conjugates were radiolabeled after reacting with ^{68}GaCl$_3$ at 75 °C for 15 min. After radiolabeling reaction, C18 cartridge was used to separate the unreacted ^{68}Ga. Finally, the labeled product was eluted from the C18 cartridge by an 80% ethanol/H$_2$O solution. The radiochemical yield and specific activity of ^{68}Ga-labeled NOTA-mono-, di- and trivalent EM2198 was determined by iTLC and radio-HPLC (**Table 14)**.

Table 13. MALDI-MS characterization of the multimeric NOTA-EM2198 conjugates

Peptide	calc'd m/z	measured m/z
NOTA-1A-EM2198	4145.33	4206
NOTA-2A-(EM2198)$_2$	7986	7801
NOTA-3A-(EM2198)$_3$	11741.49	11896

Table 14. Radiochemistry results of the multimeric ^{68}Ga-NOTA-EM2198 conjugates

Peptide	RCY (%)	SA (GBq/µmole)
NOTA-1A-EM2198	29-32	5.9-8.0
NOTA-2A-(EM2198)$_2$	46-59	3.5-11.1
NOTA-3A-(EM2198)$_3$	55-58	8.7-10.5

RCY: radiochemical yield; SA: specific activity

To evaluate the *in vivo* kinetics of the multimeric EM2198-based imaging probes, ^{68}Ga-labeled the mono-, di-, or trivalent NOTA-EM2198 were i.v. injected in normal C57BL/6 mice for PET/CT imaging, as shown in **Figure 26**. Based on the PET image results, di- and trivalent EM2198 showed markedly high liver uptake whereas monovalent EM2198 was mainly accumulated in kidneys. The *in vivo* results were confirmed with *ex vivo* PET scans. The liver uptake of the trivalent EM2198 was found to be 3.7 and 13.9 times higher than the di- and monovalent conjugates, respectively. Possibly, increasing the valency of the conjugate resulted in the increase of lipophilicity of the compound and subsequently the liver uptake. To confirm this hypothesis, further studies were performed to calculate the partition coefficient (log*P*) values of all three new compounds. The log*P* value of the trivalent EM2198 conjugate was -0.38 significantly lower than the divalent (-0.66) and monovalent (-0.68) conjugates. These results

confirmed our assumption that the increased lipophilicity of the trivalent compound results in the increased uptake in liver (**Fig. 27**).

Our ongoing work on the development of multivalent imaging probes based on the NOTA scaffold includes the incorporation of a PEG12 side chain into the constructs in order to minimize the non-specific binding in liver by increasing the desired hydrophilicity (**Scheme 6**).
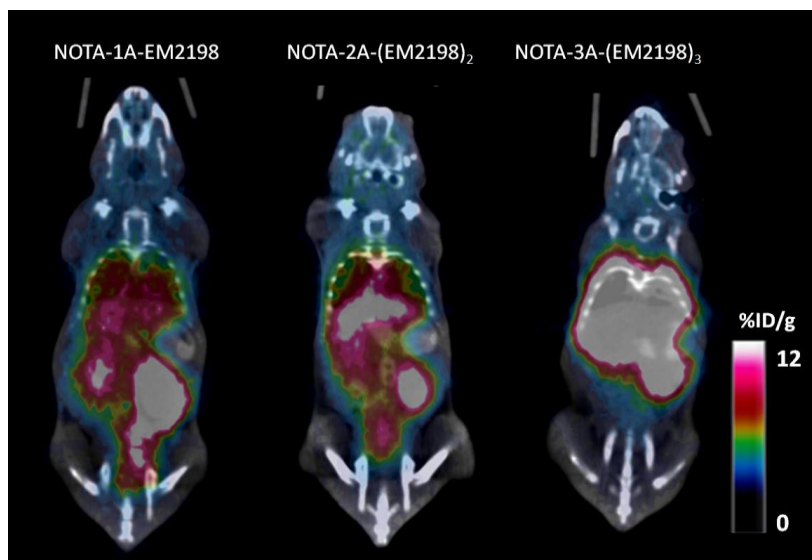
Figure 26. *In vivo* distribution of ^{68}Ga-NOTA-mono-, di- and trivalent EM2198
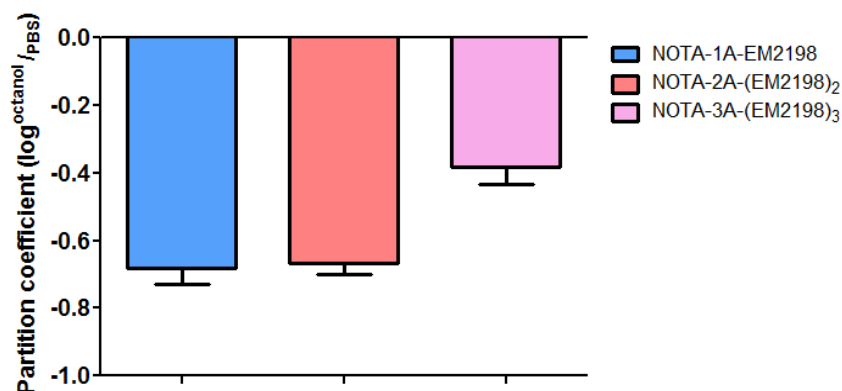
Figure 27. Partition coefficient (log P) of mono-, di-, and trivalent NOTA-EM2198 conjugates

NOTA ^{t}Bu$_3$-PEG$_{12}$NH$_2$: $\quad$ X$_1$ = R, X$_2$, X$_3$ = H, X$_4$ = ^{t}Bu
NOTA ^{t}Bu$_3$-(PEG$_{12}$NH$_2$)$_2$: X$_1$, X$_2$ = R, X$_3$ = H, X$_4$ = ^{t}Bu
NOTA ^{t}Bu$_3$-(PEG$_{12}$NH$_2$)$_3$: X$_1$, X$_2$, X$_3$ = R, X$_4$ = ^{t}Bu

NOTA ^{t}Bu$_3$-PEG$_{12}$Mal: $\quad$ X$_1$ = R, X$_2$, X$_3$ = H, X$_4$ = ^{t}Bu
NOTA ^{t}Bu$_3$-(PEG$_{12}$Mal)$_2$: X$_1$, X$_2$ = R, X$_3$ = H, X$_4$ = ^{t}Bu
NOTA ^{t}Bu$_3$-(PEG$_{12}$Mal)$_3$: X$_1$, X$_2$, X$_3$ = R, X$_4$ = ^{t}Bu

NOTA ^{t}Bu$_3$-PEG$_{12}$-EM2198: $\quad$ X$_1$ = R, X$_2$, X$_3$ = H, X$_4$ = ^{t}Bu
NOTA ^{t}Bu$_3$-(PEG$_{12}$-EM2198)$_2$: X$_1$, X$_2$ = R, X$_3$ = H, X$_4$ = ^{t}Bu
NOTA ^{t}Bu$_3$-(PEG$_{12}$-EM2198)$_3$: X$_1$, X$_2$, X$_3$ = R, X$_4$ = ^{t}Bu

NOTA (COOH)$_3$-PEG$_{12}$-EM2198: $\quad$ X$_1$ = R, X$_2$, X$_3$ = H, X$_4$ = H
NOTA (COOH)$_3$-(PEG$_{12}$-EM2198)$_2$: X$_1$, X$_2$ = R, X$_3$ = H, X$_4$ = H
NOTA (COOH)$_3$-(PEG$_{12}$-EM2198)$_3$: X$_1$, X$_2$, X$_3$ = R, X$_4$ = H

Scheme 6. Design of mono-, di-, and trivalent EM2198 with NOTA scaffold with PEG12 linker

4.3 Conclusion

To develop an effective molecular imaging probe, there are several key elements such as: i) high binding affinity to the target, ii) high *in vivo* stability, iii) good contrast ratio between target and non-target, iv) high specificity and v) low immunogenicity and toxicity. Previously, we had showed that EM2198 displayed: i) good enzymatic stability against DPP-IV and NEP24.11, ii) high binding affinity to the target and iii) good imaging contrast between target (pancreas) and

non-target (liver). In this chapter, we performed further *in vivo* experiments in order to understand the biological behavior and specific targeting of EM2198. Based on the pharmacokinetics (PK), EM2198 displayed rapid clearance from blood with elimination half life 28 min and followed with a distribution half life of ~10 h. Compared to the GLP-1 without lactam constrains, EM2198 showed similar stability as exendin-4 and maintained intact 4 h p.i. Specificity of EM2198 to the target was verified by the blocking study. However, the markedly high renal uptake might be problematic for imaging quantification. To overcome this problem, L-lysine co-administration was included to the imaging protocol, which resulted in an effective reduction in renal uptake. We further attempted to improve the sensitivity by designing a multimeric presentation of EM2198 on a NOTA scaffold. However, higher liver uptake was observed in the multimeric imaging probes. This is likely caused by the increased lipophilicity and size of the compounds that result in the rapid clearance of the multimeric conjugates from the circulation by the reticuloendothelial system (RES). Further modifications in the design of the probes are needed to improve the *in vivo* kinetics and to reduce the lipophilicity of the imaging probe. Such modifications can involve changes of the linker between the peptide and the BFC to longer PEG chains and/or decorate the BFC after pegylation or glycosylation. For the purpose of this study, we used the monomeric radiolabeled EM2198 for GLP-1 targeted BCM assessment. In the next chapter, we present our efforts to optimize the imaging method so as to assist the better interpretation of BCM imaging in a mouse model.

CHAPTER FIVE

RADIOLABELED EM2198 CONJUGATES FOR GLP-1R TARGETED BCM

ASSESSMENT – IMAGING METHODS AND INTERPRETATION (AIM 3)

In the previous chapter, we presented our efforts to identify the biological behavior of EM2198 through pharmacokinetics and biodistribution studies. The radiolabeled EM2198 showed rapid clearance in blood and specific accumulation in pancreas. Compared to the L-GLP-1, EM2198 displayed not only a better *in vivo* stability but also good pancreas targeting. Combined with the high sensitivity of PET, ^{68}Ga-NOTA-EM2198 might be able to image BCM *in vivo*. However, due to the poor spatial resolution, it is impossible to directly image BCM only with PET imaging. Emerging multimodality molecular imaging techniques such PET/CT, SPECT/CT, and even PET /MRI provide tremendous opportunities in BCM imaging due to the combination of high sensitivity and spatial resolution. However, it is still very difficult to image BCM in a rodent model, because pancreas is a membrane-like tissue which is sparse and heterogeneously distributed throughout the rodent pancreas. The task for monitoring the decreasing BCM in a diabetic mouse model is even more challenging. Furthermore, the contrast of an imaging probe is strongly affected by the activity retention in adjacent tissues such as liver and kidneys, which further makes the PET imaging quantification inaccurate. Due to these limitations, it is very important to find a reliable and reproducible imaging method to validate the *in vivo* imaging potential of EM2198 to assess BCM changes in a rodent model. Hence, there are two goals in this part of work, i) to validate the potential of EM2198 to image GLP-1R expression

for BCM quantification and ii) to develop the imaging methods in combination with the available imaging modalities, CT and MRI, for the imaging localization of pancreas in rodents.

5.1 Research Strategy

5.1.1 Ex vivo PET imaging validation of GLP-1R targeted ^{68}Ga-NOTA-EM2198 retention in normal and diabetic mouse model

The loss of BCM is closely related to the diabetes onset. Therefore, to trace the changes of BCM in healthy and diabetic subjects is an important goal of diabetes research. However, it is extremely challenging to monitor the BCM *in vivo* during disease progression. As shown before, based on the biodistribution and cell-based receptor binding studies, EM2198 showed the potential of targeting pancreas through GLP-1R as exendin-4. However, there is no direct evidence showing that the targeting was on the pancreatic β-cells. In this Chapter, we aimed to validate the potential of EM2198 to monitor the changes of BCM between normal and diabetic mice by correlation of *ex vivo* imaging and histological examinations. To this aim, two methods were applied. The first method focused on the overall uptake of EM2198 in the pancreas and adjacent tissues in normal and diseased mice. In addition, the pancreas was further evaluated by histology to validate the imaging findings. The second method aimed to evaluate the *in situ* uptake of the probe in the entire pancreas. Histological studies were included to correlate the distribution of probe uptake area with the islet location. For both methods, ^{68}Ga-NOTA-EM2198 was i.v. injected in normal and STZ-induced T1D mice. At 1 h p.i., the entire pancreas and adjacent tissues such as stomach and duodenum were excised after perfused with phosphate buffered saline (PBS), The tissues were then subjected to PET /CT imaging. The PET image analysis was based on the region of interest selected by CT. Pancreas samples from the first method were further stained for identification of α- and β-cells using the appropriate biomarkers.

Whole hematoxylin and eosin (H/E) stained pancreas sections from the second method were imaged using a montage microscope (Nikon) to correlate the imaging findings and the histological analysis. The size, number, and volume density of putative islets were evaluated within the pancreas sections (head, body, and tail).

5.1.2 Contrast-enhanced CT imaging of gastrointestinal tract for assisting pancreas localization in mouse model

One of the challenges of *in vivo* imaging of BCM in rodents is the nature of presentation of the pancreas. As highlighted in **Figure 28a**, a part of pancreas head and body can be visualized by flipping over the liver. The pancreas tail is under the stomach and attached to the spleen. In general, it is a membrane-like tissue which connects to other tissues such as stomach and duodenum (**Fig. 28b**). Another challenge is that the location of pancreas is nearby liver and kidneys. With the high blood flow rate in those two organs, it is possible to overestimate the imaging quantification in pancreas due to the activity spillover from the high nonspecific background. To that end, it is important to find a secondary imaging modality with better anatomical spatial resolution to locate the pancreas area and further enhance the quantification accuracy of PET imaging.
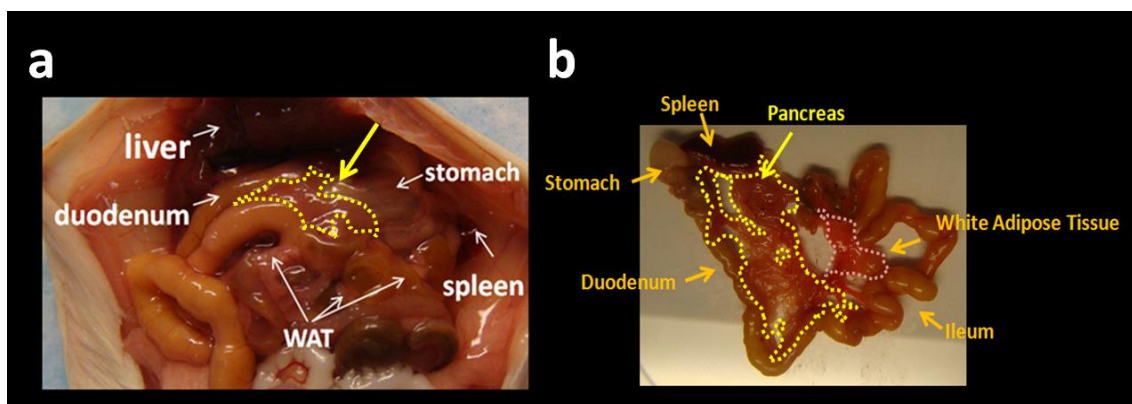
Figure 28. Anatomical location of the mouse pancreas. (a) Mouse pancreas is displayed as membrane-like tissue (b) *Ex vivo* disposition of the pancreas along with surrounding tissues.

Since a hybrid Siemens PET/CT system was available in our laboratory, Computed Tomography (CT) was a straightforward option for our anatomical imaging evaluation. However, without contrast media, CT shows a poor contrast of soft tissue in the gastrointestinal (GI) tract. Therefore, a GI tract CT contrast agent, $BaSO_4$ (Readi-CAT® 2, Ez EM, Lake Success, NY), was administrated to the mice through oral administration. The mice were then subjected to CT imaging for the anatomical information of GI tract.

5.1.3. MRI-aided in vivo PET imaging of BCM with ^{68}Ga-NOTA-EM2198

Compared to CT, MRI provides exquisite contrast of soft tissues. For that reason, it demonstrates a relatively accurate guidance on the anatomic location of the pancreas which is needed for the PET imaging analysis[227]. During our experiments, each animal was subjected to MR imaging on a 7-T small animal MR system (Varian, Inc, Palo Alto, CA) with a 40 mm internal diameter (I.D.) of Horizontal Millipede™ Coil. Since the MRI and PET systems were at different locations, the animal was placed on a positioning device (**Fig. 29**) equipped with a

respiratory sensor to maintain constant the animal orientation for an accurate coregistration of PET and MRI images. After MRI imaging, the animal was transfered to the PET scanner. ^{68}Ga-NOTA-EM2198 was i.v. injected for 1 h dynamic PET scan in normal and diseased mice. MRI dicom file was transferred to Siemens Inveon workstation for coregistration of the two images and analysis.
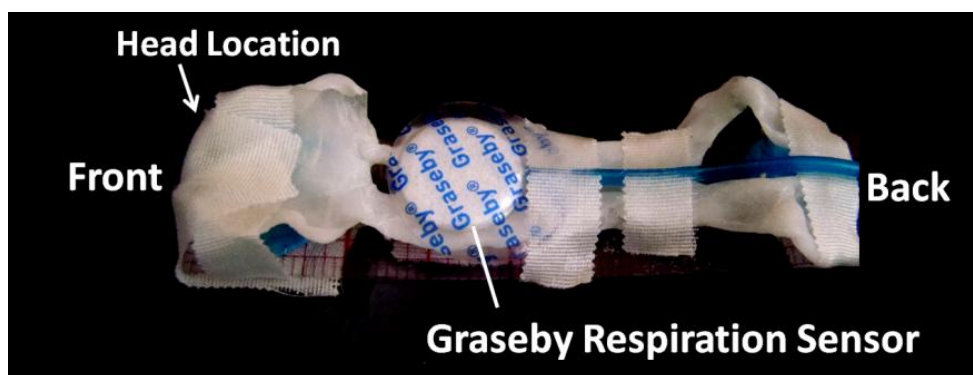
Figure 29. Positioning device for MRI and PET imaging.

5.1.4 In vivo PET imaging of BCM with ^{64}Cu-DOTA-EM2198 aided by BaSO$_4$-enhanced CT

In order to evaluate the targeting potential of the EM2198-based imaging probe *in vivo*, we further performed the PET imaging with ^{64}Cu-DOTA-EM2198 in normal and STZ-induced T1D mice. Moreover, a blocking experiment was performed by co-administration of the probe along with an excess dose of cold EM2198 to evaluate the specific targeting potential of EM2198. Due to its low positron energy ($E_{\beta+max}$= 0.65 MeV, mean range ~0.9 mm) and commercial availability, ^{64}Cu was chosen for the initial evaluation of EM2198. In this study, prior to the imaging probe injection, BaSO$_4$ was orally administered to mice assist in the identification of pancreas by locating the adjacent organs through CT.

5.1.5. Imaging reproducibility

A consistent ROI throughout the experiment is one of the key elements for the imaging reproducibility. Due to the high renal uptake of radiolabeled EM2198, ROI location for our study is selected as the red arrow shown in **Fig 30** which is in between stomach and duodenum to minimize the activity spillover from the kidneys.
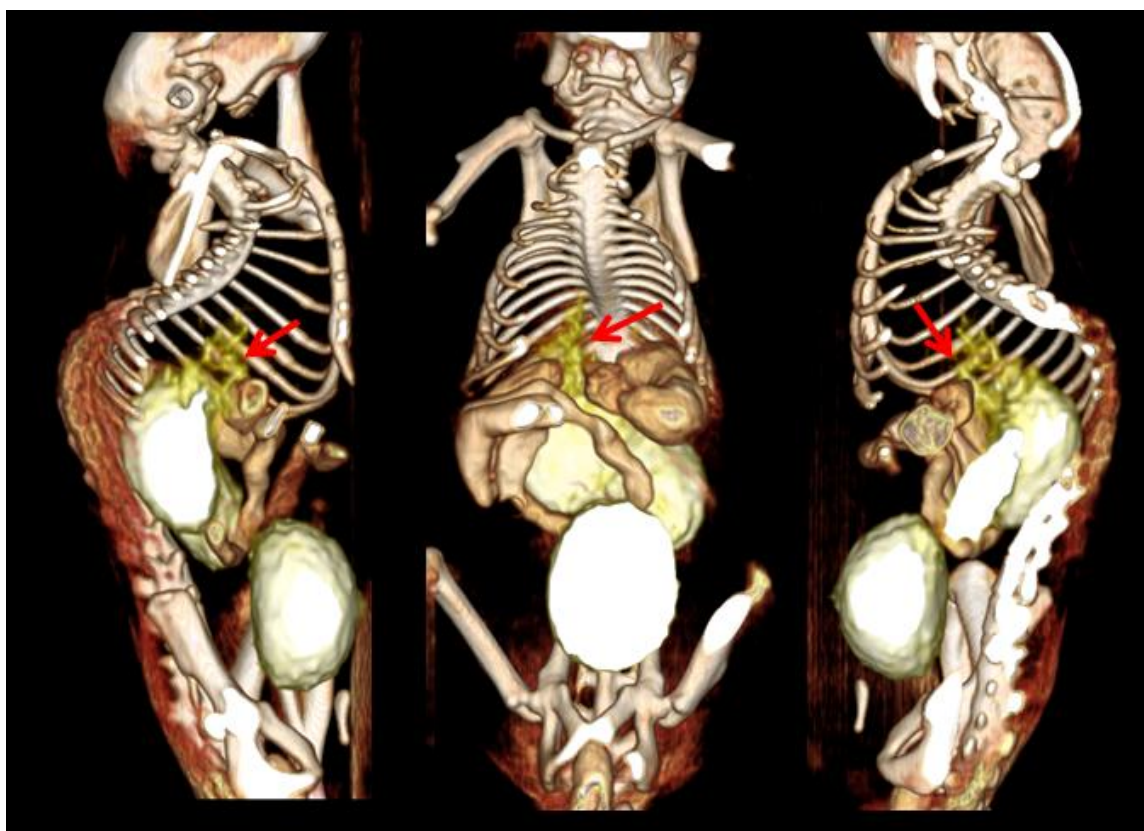
Figure 30.   Three dimensional image of PET/CT with $BaSO_4$-enhanced GI tract for the localization of the pancreas. Pancreas is highlighted with red arrow. Mouse is orally administrated with CT contrast agent $BaSO_4$ before PET/CT imaging.

To test the imaging reproducibility, animals were firstly orally administrated with $BaSO_4$ to assist the localization of the pancreas area through CT. ^{68}Ga-NOTA-EM2198 was then used and PET/CT imaging was performed in normal C57BL/6 mice. The coefficient of variation (%CV)(**Equation 1**) was used for the evaluation of reproducibility.

$$\text{Coefficient of Variation (\%CV)} = \left[\frac{\text{Standard Deviation (SD)}}{\text{Mean}} \right] \text{x100\%.}$$

Equation 1. Coefficient of variation

Two imaging sets were performed. The first set was aiming to evaluate the imaging reproducibility in different individuals. Thirteen mice were used in this study. To determine the inter-observer variation in measurements of pancreatic activity, independent ROIs were generated and compared for consistency. Three mice from this group were then chosen and subjected 3 days later to imaging to evaluate the reproducibility in the same individual.

5.1.6. Comparison of EM2198 and exendin-4 for BCM imaging by in vivo PET/CT

Although the GLP-1R agonist exendin-4, has only 53% sequence similarity with L-GLP-1, it has 6-fold higher binding affinity and 3.5-fold enzymatic stability to GLP-1R and proteases, respectively. As such, exendin-4 has been widely used for imaging insulinoma[131, 223], transplanted human islets[134], and BCM [132, 133, 224]. Moreover, it has been approved by FDA for diabetes therapy due to its 10-fold higher receptor potency than L-GLP-1[228, 229]. Based on our previous experimental data, EM2198 showed comparable enzymatic stability and specificity to that of

exendin-4. Hence, it was also necessary to compare the imaging capabilities of EM2198 and exendin-4. To that end, EM2198 and exendin-4 were labeled with ^{68}Ga through a NOTA moiety. The same *in vivo* PET imaging protocol was applied for both probes. For the imaging analysis, regions of interest (liver, pancreas, lung, and kidney) were selected and analyzed on a Siemens Inveon workstation.

5.2 Results

5.2.1 Ex vivo PET imaging validation of GLP-1R targeted ^{68}Ga-NOTA-EM2198 retention in normal and diabetic mouse model

Ex vivo PET was performed on the organs of interest excised from saline-perfused mice. The probe uptake level was determined by the percentage of the injected dose (%ID) which was normalized to the animal body weight (g). As shown in **Fig. 31**, the uptake of ^{68}Ga-NOTA-EM2198 was high in the pancreas of a normal mouse (1.7 ± 0.1%ID/g). The bright spots on duodenum and stomach were the residual pancreatic tissues after the organ removal. In sharp contrast, the corresponding pancreas tissues in the STZ-treated mice showed much lower presence of ^{68}Ga-NOTA-EM2198 (0.8 ± 0.2 %ID/g). After the PET scan, the pancreas was submitted for histological examinations. Islets from normal and diabetic mice showed similar morphology. However, the expressions of insulin and GLP-1R were reduced in the islets from diabetic mice (**Fig. 32**). It is noteworthy that a high PET signal was highlighted near the stomach of both normal and STZ-treated mice (**Fig. 31**). A close examination revealed that the spot was the antrum of stomach, where the GLP-1R expression is not affected by STZ-induced BCM destruction in the pancreas [230].
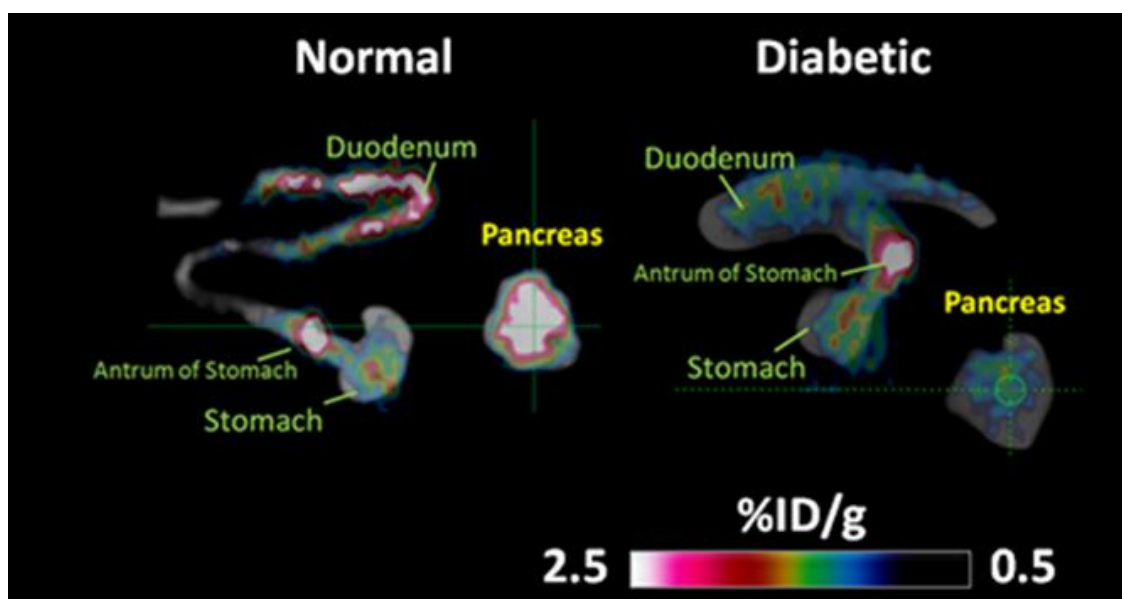
Figure 31. *Ex vivo* PET/CT imaging of organs of interest of normal and STZ-induced diabetic mice.
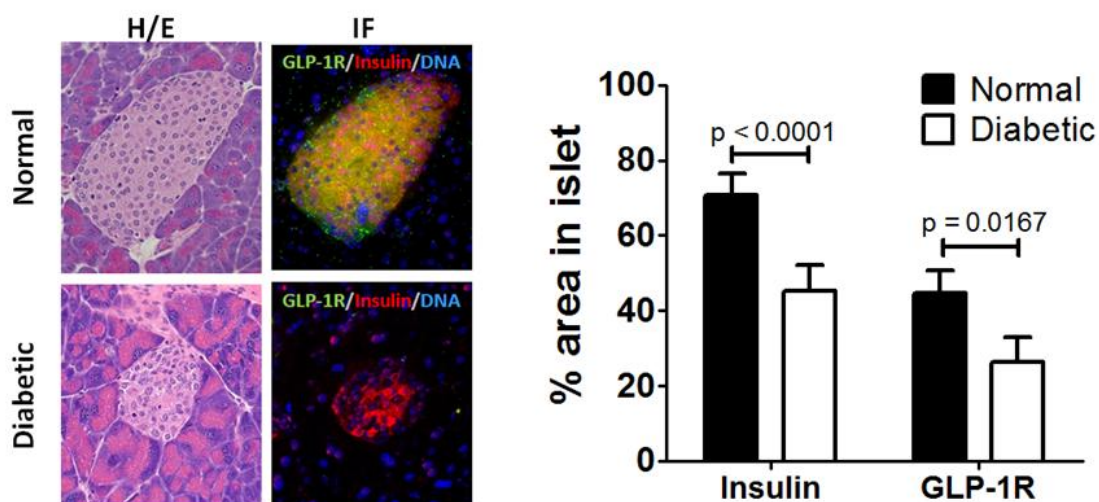
Figure 32. Histological evaluations of islets' morphology and β-cell markers expression in pancreatic islets of normal and diabetic mice. (a) H/E and immunofluorescence staining of pancreatic islet from normal and diabetic mice. (b) Quantitative analysis for insulin and GLP-1R expression level (n = 12). Statistical analysis is performed by nonparametric Mann-Whitney test with confidence level of 95%.

To identify the correlation between the level of pancreas uptake and the BCM change between normal and diabetic state, we performed *ex vivo* PET scans on flatten pancreas excised from normal and diabetic mice. The flatten pancreas was sliced and stained with H/E (surrounding figures in **Fig. 33a and b**). Based on the *ex vivo* PET imaging, the percentage of high uptake region (0.7-1.6 %ID/g) in pancreas from normal mice was significant higher (6.11 %) compared to pancreas from diabetic mice (2.59%) (**insert of Fig. 33c**). The normal pancreas contained much larger islets (**Fig. 33d**) and the PET signal area was clearly located on these larger islet clusters in pancreas body and tail (**Fig. 33a**). These results confirmed the heterogeneity of pancreas regarding the size and distribution of the islets[231]. On the other hand, in pancreata from diabetic mice, the islets' size was much smaller and the uptake of the probe was significant lower (**Fig. 33b**). These results indicated that ^{68}Ga-NOTA-EM2198 has the potential to *in situ* locate the islets and showed the specificity of uptake in the normal mice pancreatic islets.
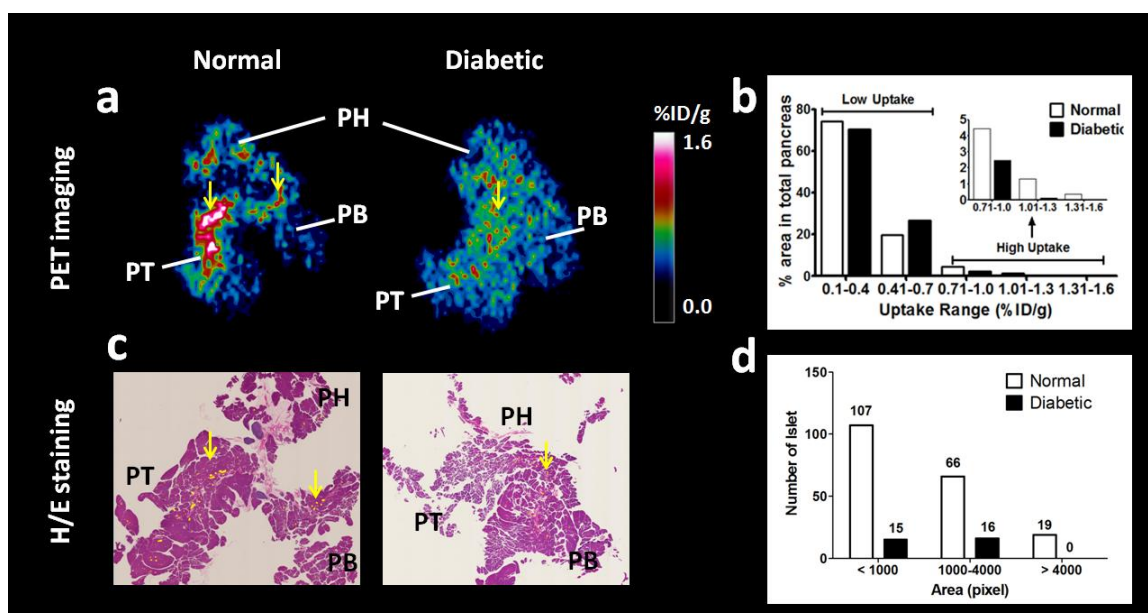
Figure 33. *In situ* localization of BCM by *ex vivo* PET imaging with ^{68}Ga-NOTA-EM2198. (a) *Ex vivo* PET/CT imaging of flatten pancreas and (b) the correlated H/E staining from normal and STZ-induced T1D mice. (c) Imaging analysis by segmentation of uptake level. The insert figure is the percentage of area in total pancreas of higher uptake level (0.7 to 1.6 %ID/g). (d) Quantification of islet area from H/E stained specimens. Data was collected from three sequential slides of the same individual. The number of islet is the sum of three slides.

5.2.2 Contrast-enhanced CT imaging of gastrointestinal tract for assisting pancreas localization in mouse model

Thirty minutes prior to CT scan, normal C57BL/6 mice were orally administrated with 500 µl of $BaSO_4$. CT scans were performed on a Siemens hybrid PET/CT scanner and CT imaging clearly revealed the GI tract *in vivo* (**Fig. 34**). This method was further used to assist the identification of the pancreas area on the PET images by locating the adjacent organs (stomach and duodenum by $BaSO_4$-enhanced CT, kidneys and liver by normal CT). This valuable method allowed us to pinpoint the pancreas area.
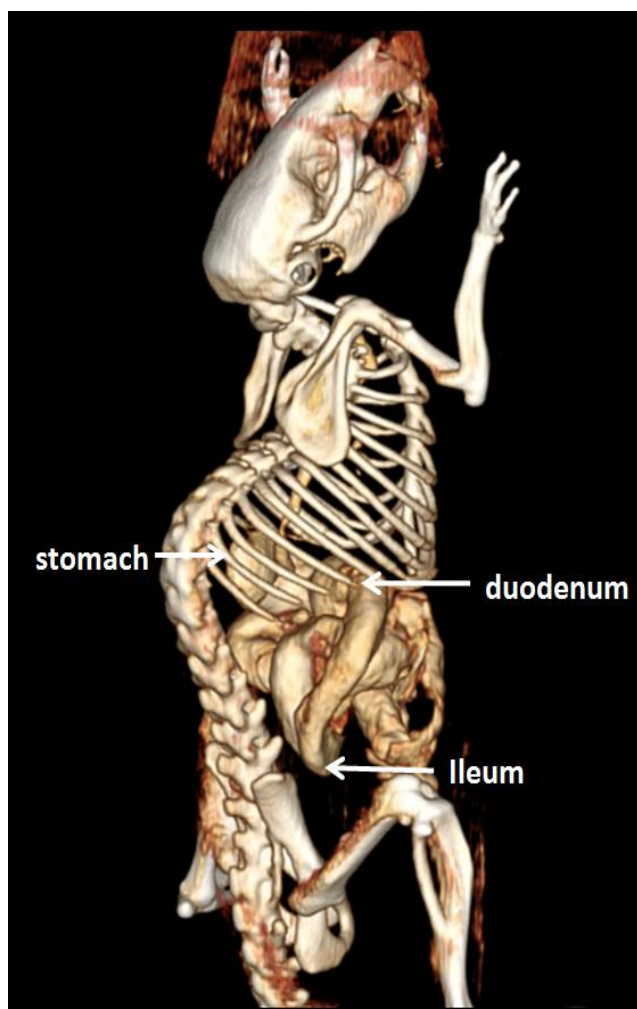
Figure 34. Surface rendering CT imaging of mouse with BaSO$_4$-enhanced CT contrast in gastrointestinal tract

5.2.3 MRI-aided in vivo PET imaging of BCM with ^{68}Ga-NOTA-EM2198

Based on the tissue contrast, mouse pancreas was clearly delineated in the axial and coronal views of PD-T1-mixed weighted MRI as highlighted in yellow in **Figure 35a and b**. Using the high spatial resolution MR imaging as guidance for drawing the regions of interest (ROIs), PET imaging analysis was performed in the axial view of the fused MRI/PET images in

normal mice (**Fig. 35a lower and 35b right**). Pancreas uptake was clearly identified in the pancreas area from axial and coronal views which provided relatively accuracy of imaging quantification. Moreover, this method also could be used on clinical implementation.
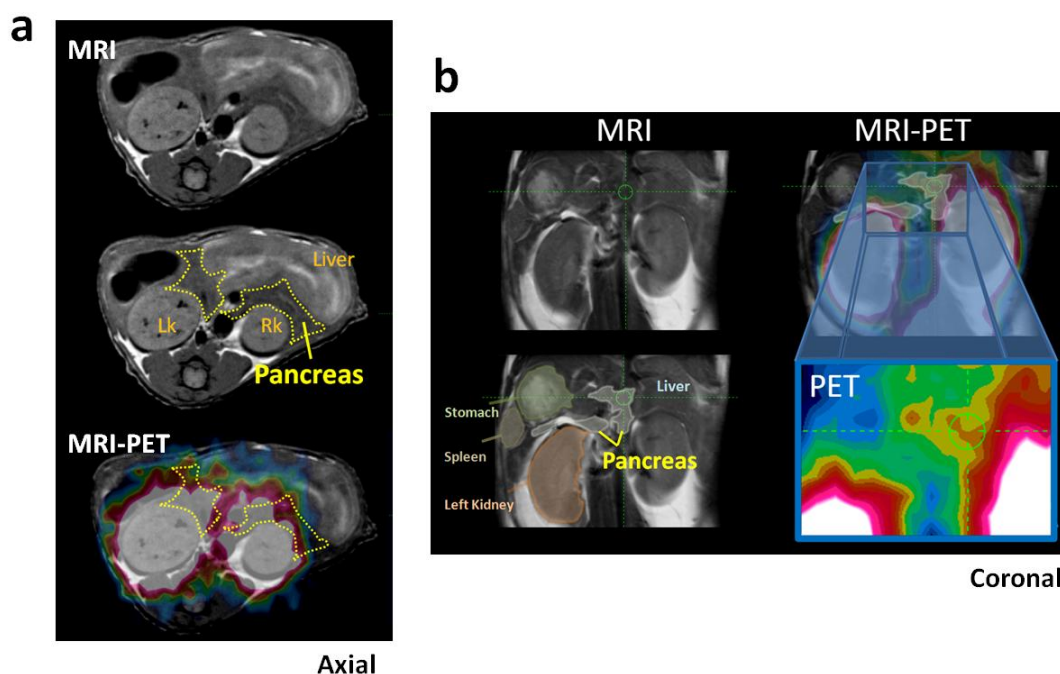
Figure 35. Representative *in vivo* MRI-aided PET imaging in normal mouse. Axial (a) and coronal (b) views of MRI-aided PET imaging with injection of ^{68}Ga-NOTA-EM2198. The pancreas areas are highlighted with yellow dotted line. Probe accumulation is observed on the pancreas area located by MRI. The enlarged imaging in (b) highlighted the PET signal in pancreas area. Sp: spleen; St: Stomach; L-k: Left Kidney; R-k: Right Kidney.

5.2.4 In vivo PET imaging of BCM with ^{64}Cu-DOTA-EM2198 aided by BaSO$_4$-enhanced CT

As shown in **Figure 36**, the pancreas area can be easily identified when the PET images were co-registered with BaSO$_4$-enhanced CT. Due to there is no GLP-1R expression in liver, we used liver as a control tissue. Hence, *in vivo* PET images were analyzed by normalizing the pancreas uptake to the liver uptake (Pancreas-to-Liver: P/L) for signal-to-background ratio. The

P/L ratio was 1.87±0.28 in normal mice, and significantly reduced to 1.20 ± 0.14 (p = 0.05) and

1.11 ± 0.09 (p = 0.05) in the STZ-treated mice and the blockade group, respectively (**Fig. 36**).
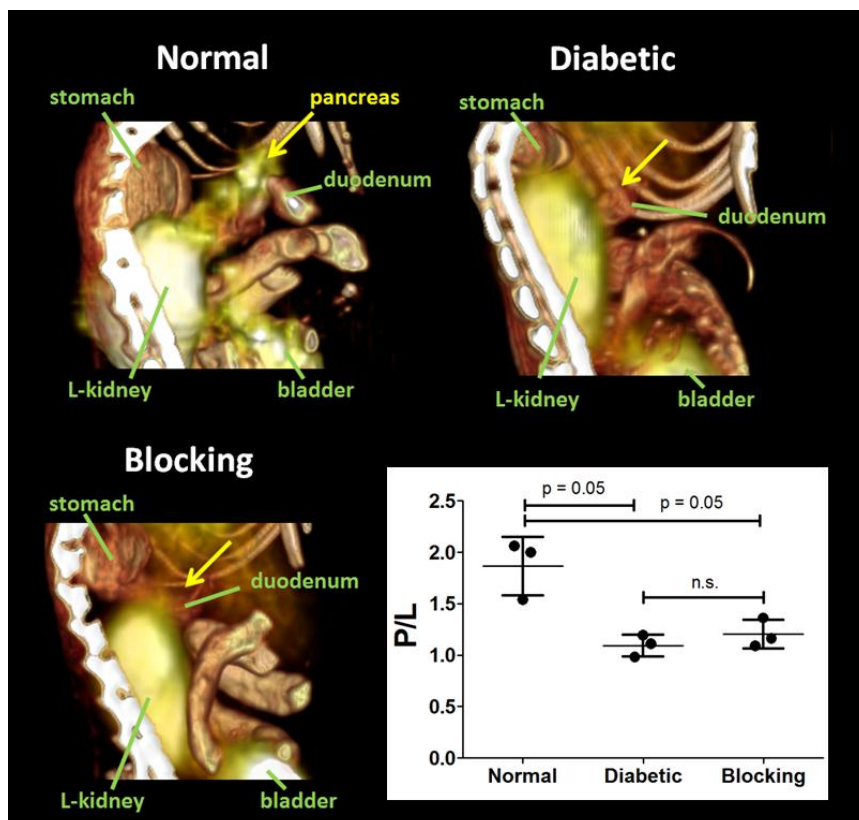
Figure 36. Surface rendering BaSO$_4$-enhanced PET/CT images for quantification of pancreas uptake in normal, diabetic mice or the mice coinjected with excess of cold EM2198. Based on the CT imaging, pancreas uptake is clearly visualized and attached to the duodenum in the PET scan with normal mice.

5.2.5 Imaging reproducibility

The imaging quantification for pancreas uptake was performed on BaSO$_4$-aided PET/CT

imaging (**Fig. 37a**). Seven PET/CT scans were performed and the ROIs were based on CT after

administration of oral contrast. The %CV of the pancreas uptake from the seven scans was found

8.84%. Similar %CV (10.06%) was observed from the second observer by using the same

analysis procedure. The %CV of the imaging reproducibility from both observers showed better reproducibility than the published [18]FDG scans in mouse tumor xenografts (25 scans: %CV= 23.2%)[232]. Due to lack experience of the second observer, the inter-observer variation was significant (**Fig. 37c**).
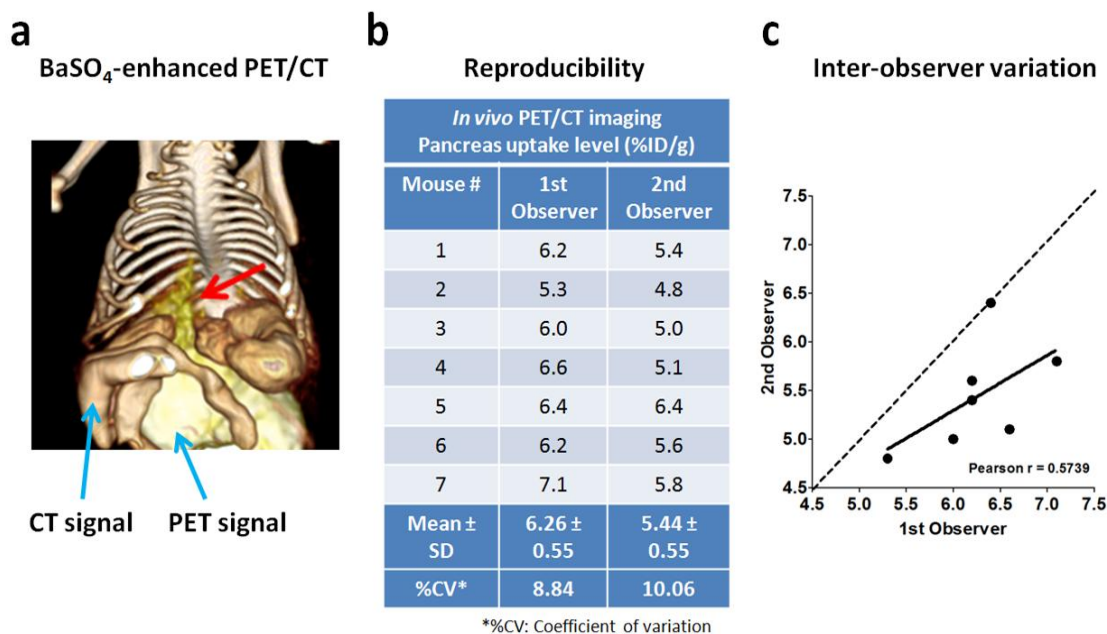
Figure 37. Evaluation of imaging reproducibility. (a) Pancreas area (red arrow) is selected based on the BaSO$_4$-enhanced GI tract CT imaging. (b) Quantification of the pancreas uptake from two different observed. Coefficient of variation (%CV) is used to determine the reproducibility of imaging method. (c) Inter-observer variation is evaluated by linear correlation between results from two observers.

5.2.6. Comparison of EM2198 and exendin-4 for BCM imaging by in vivo PET/CT

Although exendin-4 has almost 10-fold higher binding affinity compared to that of EM2198, EM2198 showed slightly higher pancreas uptake compared (**Fig. 38**) (p = 0.015). Similar uptake in lung from both peptides was observed. Interestingly, EM2198 showed

significantly higher uptake in liver and lower uptake in kidneys (p = 0.005). This might be due to the peptides differences in formal charge and lipophilicity. Based on the peptide sequence, exendin-4 has a higher charge (-1.9) than EM2198 (-0.9), lactam bridge modification is not included) which might contribute to the higher kidney uptake. Moreover, in the imaging protocol, we applied L-lysine to reduce the renal uptake which has been reported that L-lysine is ineffective to reduce the renal uptake of exendin-4. Furthermore, the lipophilicity might be increased due to the two lactam bridges on EM2198 which contribute to the higher liver uptake.
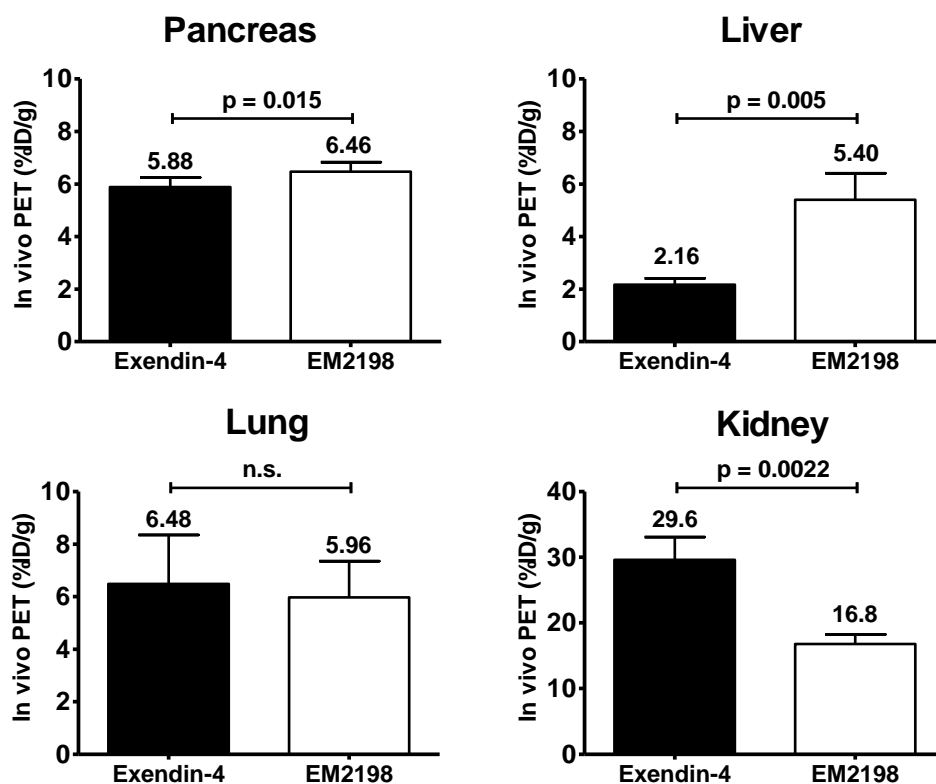
Figure 38. Comparison of the tissue uptake by *in vivo* PET imaging with ^{68}Ga-NOTA-EM2198 or ^{68}Ga-NOTA-exendin-4. PET scans were performed on the same group of mice with 5 days interval between the scans. Regions of interest (ROI) were selected based on the CT scans. Pancreas was located based on the CT enhanced gastrointestinal tract whereas the other organs (liver, right kidney and lung) can be located directly by CT.

5.3 Conclusion

Due to the lack of anatomical guidance for identification of the pancreas, it is difficult to localize the pancreas *in vivo* and accurately quantify the BCM with only PET imaging and a specific probe. Here, we performed the *ex vivo* PET imaging as gold standard to demonstrate the high accuracy of ^{68}Ga-NOTA-EM2198 in performing BCM imaging by targeting pancreatic islets. ^{68}Ga-NOTA-EM2198 was also able to detect the reduction of the signal in pancreas of diabetic mice. Based on the histological examinations, the *ex vivo* imaging results were well correlated to GLP-1R expression and islet distribution in normal and diabetic conditions. In order to develop a reliable and reproducible *in vivo* BCM imaging method with EM2198-based PET imaging probe, two strategies were applied. First, a CT-contrast agent, $BaSO_4$, was given to assist the identification of pancreas through the CT imaging of GI tract. Second, MRI was performed to locate the pancreas. Both methods can be easily adapted for clinical applications. Based on the anatomical guidance either from MRI or $BaSO_4$-enhanced CT, we were able to locate the pancreas area which was essential for the BCM imaging quantification. As the result, we established a reproducible dual modality imaging technique which showed the potential to detect the BCM loss in diabetic mice by using a highly specific GLP-1R-targeted imaging probe. Furthermore, in comparison with exendin-4, EM2198-based imaging probe showed better pancreas uptake. However, the liver uptake was significantly higher which might be due to the increased lipophilicity after the lactam bridge modification. On the other hand, due to the higher negative charge of exendin-4 and ineffective renal reduction of L-lysine, exendin-4 showed significant higher kidney uptake compared to EM2198. Since total non-specific uptake in kidneys and liver was lower, EM2198 showed better imaging contrast compared to exendin-4. In summary, in our current imaging protocol, EM2198 showed a great potential for targeted BCM

imaging which can be applied to *in vivo* imaging for the dynamic change of BCM during disease

progression.

CHAPTER SIX

IMAGING THE DYNAMIC BCM CHANGE – A LONGITUDINAL EVALUATION OF THE GLP-1R TARGETED IMAGING TECHNIQUE IN A T1D MOUSE MODEL

(AIM 4)

Both T1D and T2D are characterized by a gradual loss of functional BCM. However, the trend of the BCM loss is different between the two types of diabetes. T1D is a T-cell-mediated autoimmune disease. In patients with recent onset of T1D, the BCM loss is approximately 90%[233-236], but the remaining BCM is able to maintain the insulin secretion level at about 40% of normal level [237]. In patients with T2D (**Fig. 39**) [238], the BCM loss is not as sharp as seen in patients with T1D. Due to the variation among individuals, it is more difficult to determine the onset of T2D. As a matter of fact, most of T2D cases are not diagnosed until 10 or more years post the disease's onset[239]. During the initial insulin-resistant state of T2D, a β-cell compensation mechanism is often seen to maintain the glucose homeostasis by enhancing the insulin biosynthesis and secretion of individual β-cells [240, 241] coupling with increases in β-cell mass[218, 219] and hypertrophy of existing β-cells[242]. Over time, the β-cell compensation fails as the consequence of the increasing demand of insulin to offset the increasing insulin resistance, which leads to the exhaustion of β-cell function and the β-cell apoptosis. Based on the autopsy results, the BCM loss in patients with T2D is 65% of the normal level[39, 243, 244].
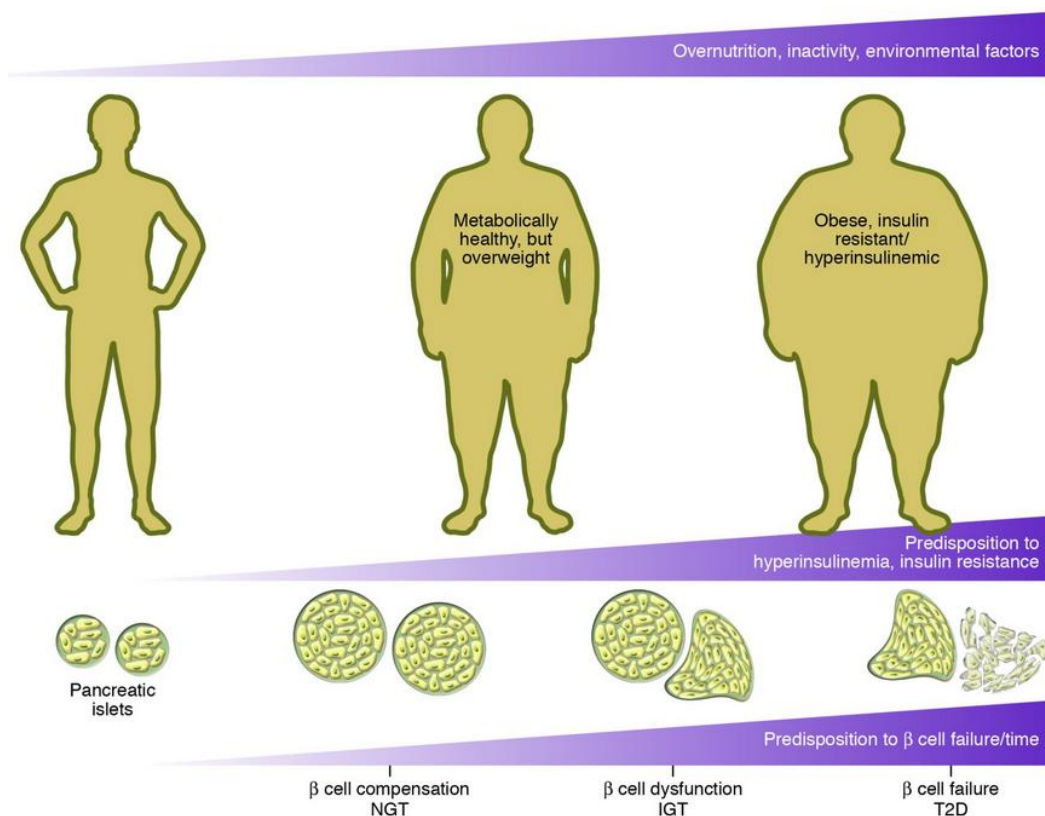
Figure 39. Pancreatic β cell failure and the natural history of T2D progression in human patients. Reprinted from Prentki, M. et al. Copyright 2006 American Society for Clinical Investigation[238].

As described above, both T1D and T2D clinically manifest a BCM loss. However, not until a sensitive and specific method is applied to *in vivo* quantification of BCM, we can possibly know the degree of BCM loss to trigger the onset of disease in individual patients. To develop such a method, it is crucial to have a proper surrogate biomarker for the evaluation of BCM change during the disease progression or treatment.

In the previous chapter, we demonstrated the potential of using a reproducible multimodality imaging technique to detect the BCM change in between normal and STZ-induced

diabetic mice. In this part of my dissertation, the goal is to further validate the potential of using this imaging technique to monitor the dynamic change of BCM during diabetes progression.

To pursue this goal, we need 1) to develop a diabetic mouse model with moderate disease progression in order to capture the dynamic change of BCM, 2) to perform the longitudinal PET/CT imaging with this imaging technique, 3) to perform *ex vivo* PET scan to verify the pancreas uptake level quantified from *in vivo* imaging, and 4) to evaluate GLP-1R expression level during the disease progression in order to correlate the imaging readouts with the BCM change quantified by conventional assays.

6.1 Research Strategy

Forty eight mice were treated with moderate dose of STZ to induce diabetes and used for the longitudinal imaging. The experimental duration was 35 days. To observe the disease progression, the fasting blood glucose level and the body weight of the mouse were measured. Prior to imaging, animals were i.p. injected L-lysine to reduce the renal uptake and followed by orally administration with $BaSO_4$ to enhance the CT contrast in GI tract. After imaging at each time point, three mice were sacrificed and organs were excised immediately for *ex vivo* PET validation and the pancreas samples were subjected for Western blots and histology to evaluate the GLP-1R expression level and BCM changes during the disease progression.

6.2 Results

6.2.1 Longitudinal PET/CT Imaging of BCM changes

Unlike ^{64}Cu, ^{68}Ga is a bench top generator produced radioisotope with higher branch ratio of positron emission. Gallium-68 allows a noninvasive PET imaging procedure to be performed on an as-needed basis for longitudinal monitoring of the BCM loss during the progression of diabetes. The potential of using ^{68}Ga-NOTA-EM2198 to assess the longitudinal BCM loss was evaluated in the STZ-induced T1D mouse model for 5 weeks. Mice were imaged before and after STZ treatment, specifically at 0, 6, 9, 15, 18, and 35 days post the treatment. At each time point, at least 6 mice were randomly selected for PET imaging with ^{68}Ga-NOTA-EM2198. A rapid decrease of P/L ratio was observed from day 0 to day 9 (**Fig. 40**). After day 9, the P/L ratio did not change within the remaining evaluation period.
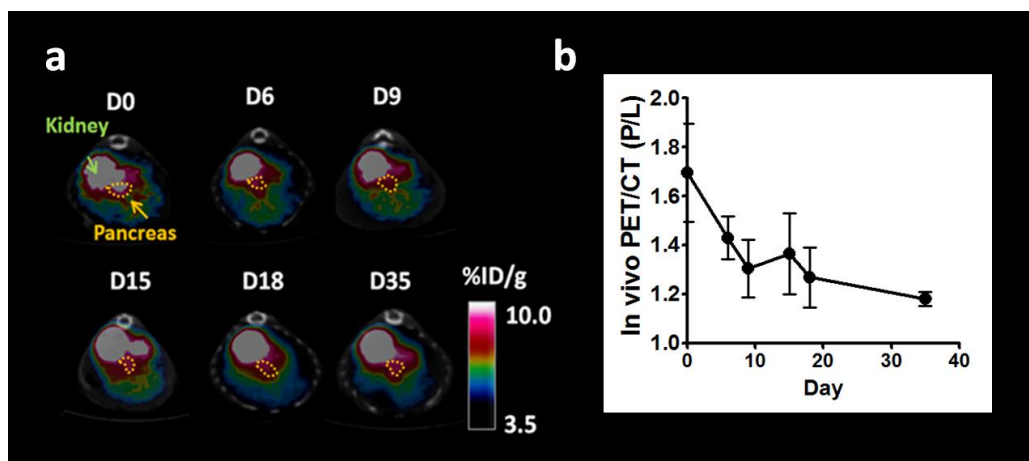
Figure 40. Longitudinal *in vivo* PET/CT imaging of BCM change in STZ-induced T1D mouse model. (a) Representative PET/CT images. Pancreas area is indicated byyellow dotted line and arrow. (b) Imaging quantification was performed by analyzing the pancreas-to-liver uptake ratio (P/L).

6.2.2. Clinical and pathological parameters of T1D progression in the STZ-induced mouse model

Clinical and pathological parameters used to evaluate the T1D progression were summarized in **Figure 41**. Two weeks after the STZ treatment, mice developed hyperglycemia (>300 mg/dl) and maintained a similar fasting blood glucose level throughout 35 days of the study period (**Fig. 41a**). Histological evaluation was performed by immunofluorescence staining (IF) (**Fig. 41b**). In brief, pancreas specimens were collected from different time points before and after STZ-treatment, and images were analyzed by ImageJ. The β-cell areas were identified by insulin-positive and GLP-1R-positive staining. High correlation between insulin and GLP-1R was observed (Pearson r = 0.9550). As shown in **Figure 41c**, the β-cell areas were gradually reduced whereas α-cell areas were not affected after STZ-treatment. Furthermore, we counted the islet number in the H/E stained pancreas specimen, which showed approximately 62% declination in the STZ-treated mice compared to the control cohort (**Fig. 41d**). Intriguingly, the islet number was also correlated with the β-cell area in each individual islet **(Fig. 42).** Moreover, the GLP-1R expression level in pancreas was analyzed by normalizing the GLP-1R intensity to the control (β-actin), showing a gradual decrease in the STZ-treated mice (**Fig. 41e**). This indicated the validity of using GLP-1R as a surrogate biomarker for the assessment of BCM change.
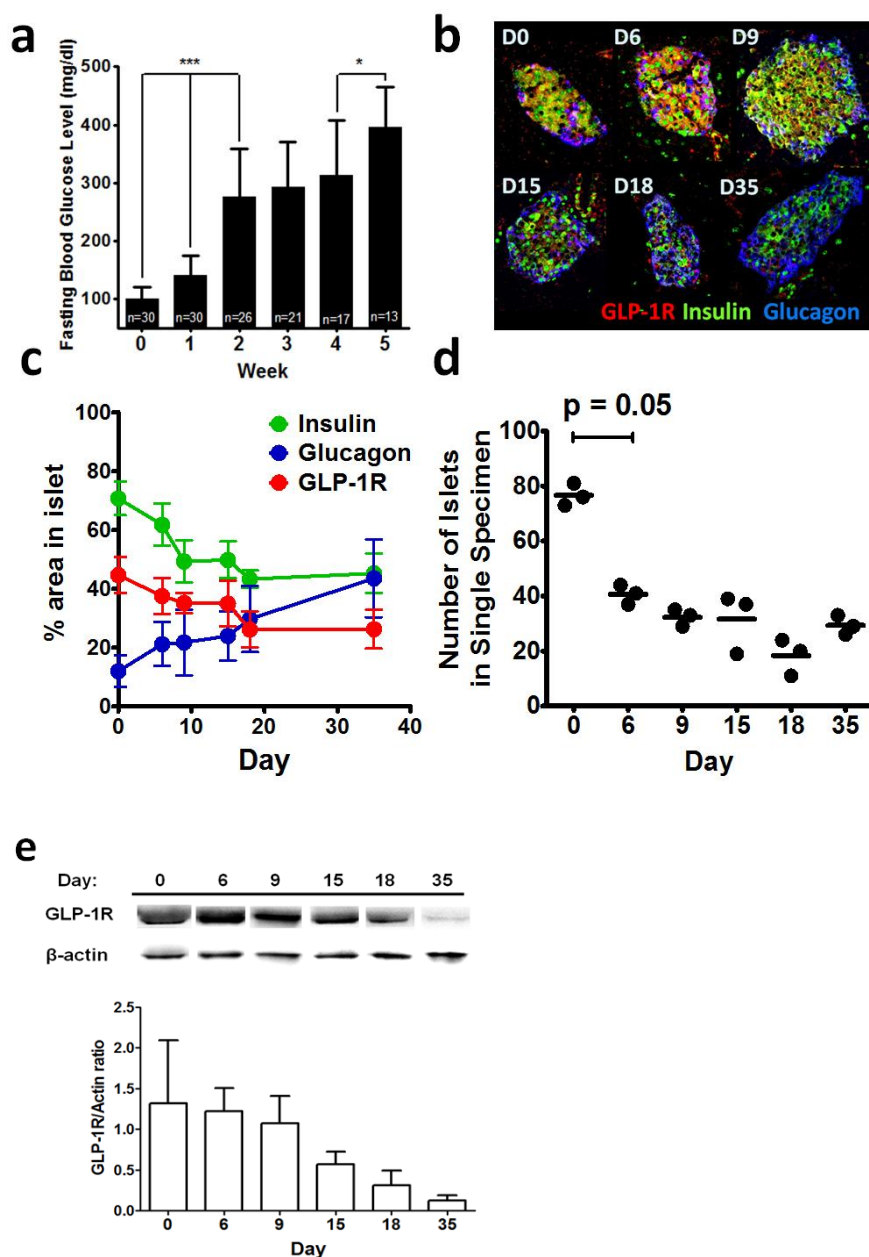
Figure 41. Development of a STZ-induced T1D mouse model. (a) Fasting blood glucose level of STZ-induced diabetic mice. *: $p < 0.05$; ***: $p < 0.0001$ (b) Immunofluorescence (IF) staining for GLP-1R (red), insulin (green), and glucagon (blue) expression in pancreatic islet. (c) Statistical analysis of IF results for the percentage of insulin-, GLP-1R- and glucagon-positive areas in a single islet. The percentage of stained area in the islet (% area in islet) is normalized to the entire islet area. (d) Pancreatic islet number obtained from the H/E assays of pancreas specimens. (e) Representative Western blot result from single mouse. GLP-1R expression change in pancreas determined by Western blots during the T1D progression in this mouse model ($n = 3$).
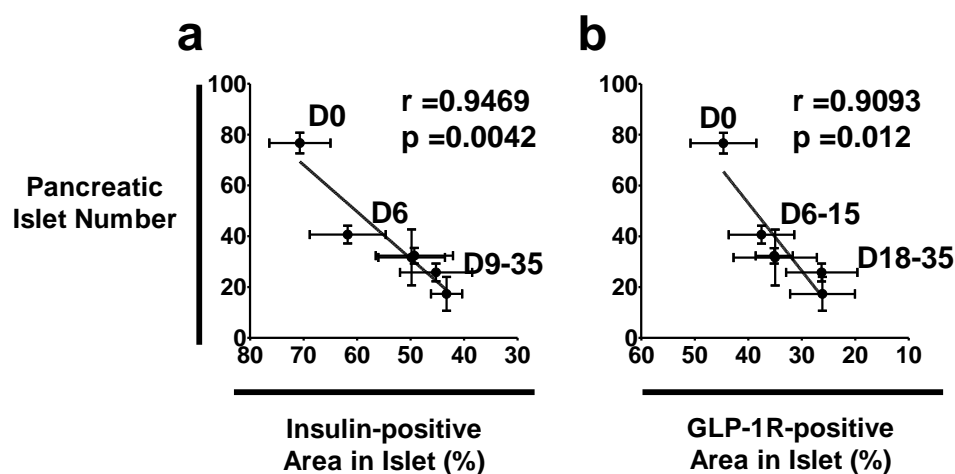
Figure 42.   Linear correlation analysis of pancreatic β-cells and islet number during disease progression. Correlation between the quantified pancreatic islet number from H/E staining and percentage of (a) insulin-positive and (b) GLP-1R-positive cells in islet from IF staining (Insulin-positive: Pearson coefficient r = 0.9469, p<0.005; GLP-1R-positive: Pearson coefficient r = 0.9093, p=0.012).

6.2.3. Correlation of ex vivo PET signals with the fasting blood glucose levels

In order to test whether the pancreatic PET signal can be used instead of the commonly used clinical parameter to monitor the diabetes progression, a series of *ex vivo* PET/CT imaging experiments of pancreas were performed in 18 STZ-treated mice over a period of 35 days after STZ-treatment to evaluate the correlation between the PET signal and the fasting blood glucose level. At days 0, 6, 9, 15, 18, and 35, three mice were subjected to *ex vivo* PET/CT imaging immediately after the *in vivo* scan. As shown in **Figures 43a-b**, a clear declination was displayed for the *ex vivo* PET signal change of pancreas over the time course. Interestingly, a two-phase correlation was observed between the *ex vivo* PET signals and the fasting blood glucose level: the *ex vivo* PET signal intensity showed a sharp 45% decrease from day 0 to day 9, followed by a

relatively mild declination to a steady state from day 9 to day 35 (**Fig. 43b**). Overall in the STZ-induced disease progression, the *ex vivo* PET signal of pancreas decreased by ca. 50% from 1.7 ± 0.1 %ID/g (day 0) to 0.85 ± 0.2 %ID/g (day 35) (**Fig. 43b**).

However, the correlation between the *ex vivo* PET signals and the fasting blood glucose levels were not significant ($p = 0.3$) from day 0 to day 9 and day 9 to day 35 with Pearson correlation coefficient r values of -0.6921 and -0.8748, respectively (**Fig. 43**). This result indicates that while the decreasing trends of both parameters might reflect the T1D progression, the sample size must be increased in the future evaluation to validate the imaging role in the assessment of β-cell function change.
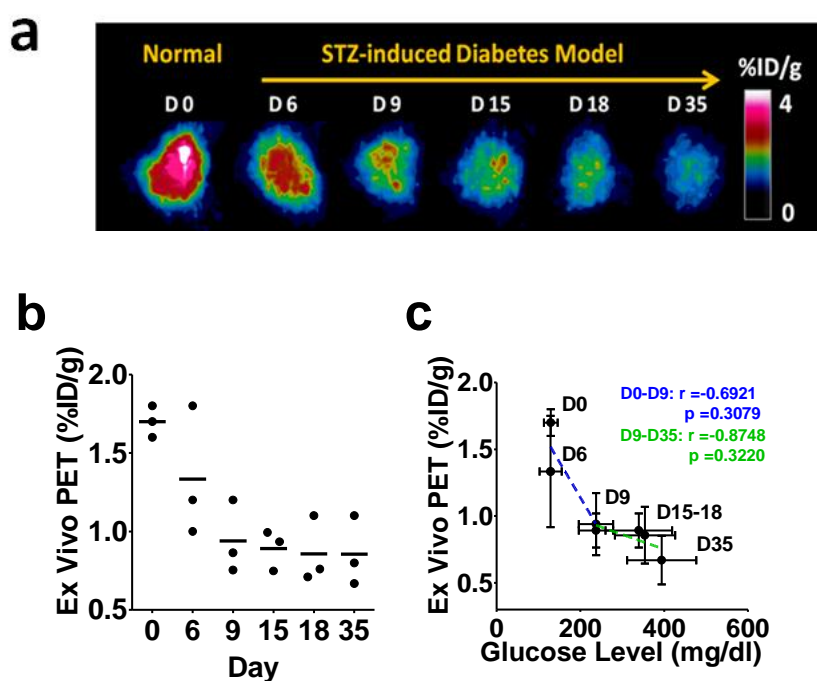
Figure 43. *Ex vivo* PET imaging of pancreas during diabetes progression. (a) Representative *ex vivo* PET/CT images of pancreas during STZ-induced diabetes progression, (b) *Ex vivo* PET signal intensity of pancreas in mice over the the time course after STZ-treatment (n = 3), and (c) Relationship between the *ex vivo* PET signal and the fasting blood glucose level. Linear regression line of day 0 to day 9 is indicated in blue, while that of day 9 to day 35 in green.

6.2.4. Correlation of imaging results with the changes of GLP-1R expression or BCM during the diabetes progression

In order to confirm that the gradual PET signal loss was caused by the BCM declination which was associated with the decrease of GLP-1R expression level, the changes of β-cell islet number and β-cell area in the pancreas were quantified by H/E staining (pancreatic islet number) (**Fig. 44a and b**) and immunofluorescence staining (% of β cells in islet) (**Fig. 44c and d**)), respectively. The corresponding GLP-1R expression was measured by Western blots (**Fig. 44e and f**). For the histology examinations, three pancreas sections were collected from each animal to cover the whole pancreas. For the Western blots, the whole pancreas lysate was collected and immunostaining performed with an anti-GLP-1R antibody. All three parameters, % β-cell area (normalized to the area of islet), pancreatic β-cell islet number, and GLP-1R expression level were found in a linear correlation with either *ex vivo* or *in vivo* PET signal throughout the study period (Linear regression R^2 > 0.84, Pearson coefficient r > 0.9, p < 0.01). Overall, our results clearly demonstrate that BCM changes can be noninvasively assessed by PET imaging with ^{68}Ga-NOTA-EM2198.
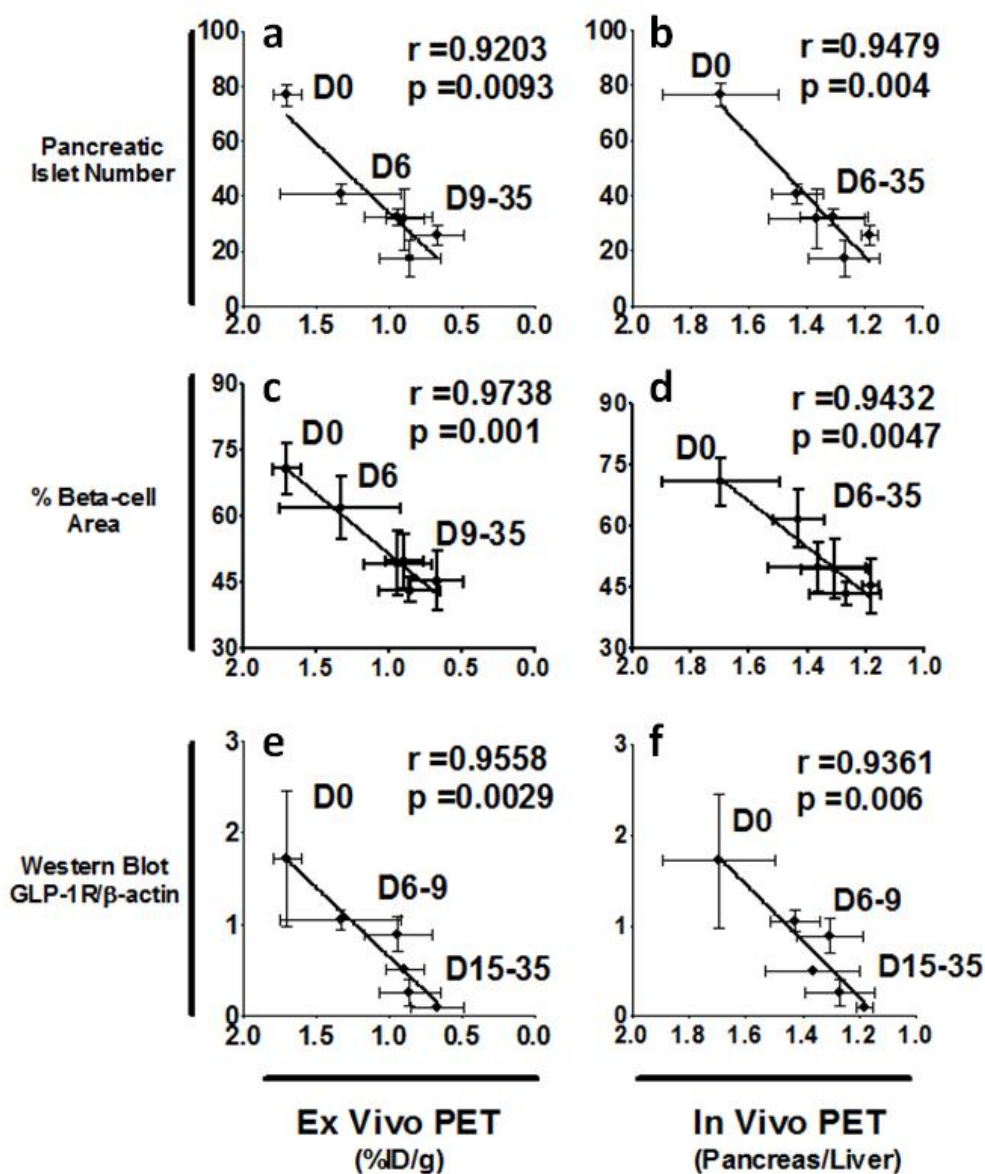
Figure 44. Linear correlation analysis of PET readouts and histological parameters. (a and b) Correlation between quantified pancreatic islet number from H/E staining and either *ex vivo* or *in vivo* PET results (*Ex vivo* PET: Pearson coefficient r = 0.9203, p<0.01; *in vivo* PET: Pearson coefficient r =0.9479, p=0.004) (c and d) Correlation between percentages of insulin-positive area in single islet and either *ex vivo* or *in vivo* PET results (*Ex vivo* PET: Pearson coefficient r= 0.9738, p=0.001; *in vivo* PET: Pearson coefficient r= 0.9432, p=0.0047). (e and f) Correlation between GLP-1R level in pancreas and either *ex vivo* or *in vivo* PET results (*Ex vivo* PET: Pearson coefficient r= 0.9558, p=0.001; *in vivo* PET: Pearson coefficient r= 0.9361 , p=0.0047).

6.3. Conclusion

In this chapter, we demonstrated that our established imaging method with ^{68}Ga-NOTA-EM2198 can be reproducibly and reliably used to noninvasively monitor the BCM change in a longitudinal manner during the progression of STZ-induced diabetes. Based on the clinical measurement, STZ-induced T1D mice developed hyperglycemia at 2 weeks after STZ-treatment. However, the pathological measurements detected the early reduction of BCM 1 week after the treatment. Linear correlations were observed between imaging results and pathological measurements which indicated the validity of using this imaging method to detect the early onset of diabetes.

CHAPTER SEVEN

PROJECT DISCUSSION AND PERSPECTIVE

7.1. Discussion

To date, several PET radiotracers have been reported for BCM imaging by targeting a variety of biomarkers expressed in pancreatic β-cells[245, 246]. Among them, [^{11}C]- and [^{18}F]-Dihydrotetrabenazine (DTBZ) have drawn most attentions and have been tested in clinical trials[48, 121]. However, given the fact that VMAT-2, the target of DTBZ, is not exclusively or is only partially expressed in pancreatic β-cells[247], a discordance remains on whether or not its imaging readout reflects the actual change of BCM. Indeed, inconsistent imaging results with [^{11}C]-DTBZ have been demonstrated [248]. Most recently, negative results indicated that the VMAT2-directed tracers [^{18}F]fluoropropyl-(+) dihydrotetrabenazine ([^{18}F]FP-DTBZ) and its derivatives did not specifically bind to β-cells[128]. One the other hand, GLP-1R appeared to provide better target since it has been reported that is exclusively expressed on pancreatic β-cells and not on other endocrine pancreatic cell types[139]. Also, based on the physiological role of GLP-1, such as triggering insulin release from β-cells, enhancing β-cells survival and regeneration of BCM[185, 186],GLP-1R ligand (GLP-1) and its agonists (exendin-4 derivatives) have been extensively studied and used for treatment of T2D. Compared to GLP-1 analogs that are often limited by a short biological half-life, exendin-4 and its analogues are resistant to the enzymatic degradation that GLP-1 suffers[190, 249]. Thus, they have been developed as radiotracers for SPECT (^{111}In, ^{125}I, and ^{99m}Tc) [137, 250-252 135, 253, 254] or PET (^{68}Ga and ^{64}Cu) [134, 255] imaging of GLP-1R-positive insulinoma. Albeit these experiments of imaging of xenografted insulinomas demonstrate their feasibility of

112

highlighting pancreatic β-cells with exendin-4-based radiotracers targeting GLP-1R, their use in assessing BCM may be limited due to the fact that BCM is decreasing over the progression of diabetes rather than increasing as in insulinomas. Also, based on the net charge of exendin-4, a higher kidney uptake is expected which might cause inaccurate imaging quantification due to higher activity spillover from the kidneys. To effectively image BCM in an *in vivo* context, radiotracers should possess higher enzymatic stability while maintaining binding affinity to GLP-1R and being more efficient in the clearance from the non-target adjacent organs of pancreas such as liver and kidneys. Finally, the major concern of using exendin-4 as BCM imaging probe is that exendin-4 has much higher receptor potency compared to GLP-1, which might activate the incretin effect. Based on the therapeutic study in obese diabetic mouse model, exendin-4 displays effective glucose-lowering ability with 50% of effective dose (ED_{50}) of 0.059 µg/kg whereas ED_{50} value of GLP-1 is 329 µg/kg[256]. With the assumption of 25g for body weight of an adult mouse, exendin-4 can effectively activate the incretin effect with ~1.5 pg of the mass whereas GLP-1 requires ~8 µg.

As an endogenous ligand to the receptor, GLP-1 has a strong binding affinity and appears to adopt an α-helical structure at the N- and C-terminal region separated by a short flexible linker region (as determined by 2D-NMR[257, 258]). The significance of the helical structure for the receptor-ligand interaction is further supported by the recent X-ray crystal structure of the truncated GLP-1[193]. The addition of lactam bridges or alpha-aminoisobutyric acid (Aib) to the peptide sequence can stabilize the helical conformation[253, 254,259], which we have utilized to develop GLP-1 analogs by placing these lactam bridges (Glu^i/Lys^{i+4} or Lys^i/Glu^{i+4}) or Aib at the inactive positions in the sequence of GLP-1. Based on the previous results of receptor potency and enzymatic stability, several effective positions were identified including Ser^{18}/Gly^{22} and

Gly^{22}/Lys^{26}, surprisingly, these residues cover the flexible region in the GLP-1 sequence [260]. The introduction of the lactam bridges in this specific region not only simultaneously stabilized the two helical segments in the N- and C-terminal regions but also maintained the receptor affinity[201]. Moreover, the lactam bridges also shielded the bicyclic peptide from NEP 24.11 degradation. Especially, GLP-1analogs with the double lactam bridges at Ser^{18}/Gly^{22} and Ala^{30}/Lys^{34} and triple lactam bridges at Val^{16}/Leu^{20}, Gly^{22}/Lys^{26}, and Ala^{30}/Lys^{34} display the similar stability against NEP 24.11 compared to exendin-4. We further developed a series GLP-1 analog by replacing Ala8 with D-Ala or Aib to minimize the enzymatic degradation by another protease, DPP IV. To evaluate the imaging potential of these GLP-1 analogs by *ex vivo* PET imaging, maleimide-functionalized bifunctional chelators (BFCs) (e.g., DOTA, NOTA) were conjugated to the peptide analogs *via* Cys through a 6-aminohexanoic acid (Ahx) spacer on C-terminal. GLP-1 analogs were radiolabeled with ^{68}Ga and subjected for *ex vivo* PET imaging in normal C57BL/6 mice. Among all GLP-1 analogs, two (EM2198 and EM4025) showed good target to non-target ratio. Compared to EM4025, EM2198 also displayed better enzymatic stability while maintaining the receptor affinity. Hence, EM2198 was selected to be developed as a BCM imaging probe. Based on the *in vivo* evaluations, radiolabeled EM2198 showed i) higher accumulation in the pancreas compared to L-GLP-1, ii) specific targeting to GLP-1R, and iii) fast blood clearance. Furthermore, radiolabeled EM2198 displayed a significant lower uptake level in the pancreas from diabetic mice. Most importantly, uptake signal from *ex vivo* PET well colocalized to histology results which indicated the probe was specific accumulated in pancreatic islets. Therefore, combining the superior sensitivity of PET, high stability and high specificity of EM2198 allow us to meet the criteria for probe development.

Due to its ideal positron energy ($E_{\beta+}max= 0.65$ MeV) and commercial availability, ^{64}Cu was chosen for the initial evaluation of whether EM2198 could be utilized for specific imaging of pancreatic β-cells in mice *in vivo*. With ^{64}Cu having a similar energy to the most widely used PET isotope, ^{18}F ($E_{\beta+}max= 0.635$ MeV), and better radiochemical yield compared to ^{18}F-labeled GLP-1 analog[151], the ^{64}Cu-labeled ligand was initially used for PET imaging evaluation in normal mice. While the pancreas region on the PET images clearly showed high uptake of ^{64}Cu-DOTA-EM2198, an anatomical imaging technique is needed to confirm the pancreas localization. As our PET scanner currently in our laboratory is coupled with Computed Tomography (CT), CT was used for the delineation of the pancreatic region along with surrounding organs. However, without contrast media, CT offers poor soft tissue contrast in adjacent organs of pancreas such as gastrointestinal tract. Therefore clinical CT contrast agent, $BaSO_4$, was administrated by orally administration to enhance CT contrast in the GI tract. This method was later proven to be a valuable tool since it allows us to pinpoint the pancreas area on co-registered PET/CT images. With the aid of $BaSO_4$–enhanced CT, we were able to evaluate the potential of EM2198 conjugates for BCM imaging as compared to their exendin-4 counterpart. From results obtained by *in vivo* PET imaging, EM2198 showed higher uptake in pancreas compared to exendin-4. In the uptake of organs adjacent to pancreas, EM2198 showed 43% lower uptake in the kidneys which results in a better contrast imaging compared to exendin-4. To validate the BCM specificity, the same imaging experiment was performed in STZ-treated mice and normal mice co-administered a blocking dose of cold (non-^{68}Ga labeled) EM2198. In the former, the pancreatic β-cells were abolished by STZ; in the latter, the GLP-1R would be overwhelmingly saturated by the cold ligand. In both cases, the BCM imaging specificity of EM2198 would be indicated by the reduction of the PET signal in the pancreas area.

Given the inherent exquisite soft tissue contrast and high spatial resolution, MRI is a second imaging technique that can assist in pancreas localization and aid in PET imaging quantification. Without a hybrid PET/MRI system, we performed the MR and PET imaging sequentially by placing a mouse on a special designed device to enhance the registration accuracy between two modalities on the same mouse. By using PD-T1 mixed MRI scan, the anatomical position of the whole pancreas can be readily identified. While we fused the MRI scan with corresponding PET images, the MR images greatly facilitate the ROI definition of PET images and thereby improve the accuracy and reliability of BCM imaging.

Ex vivo PET imaging of excised organs immediately after the PET scans can provide the absolute quantification of radiotracer's accumulation in organs of interest. To eliminate the blood contamination from the organs, mice were perfused with saline before dissection. It is remarkable that the *ex vivo* PET images together with their quantification unequivocally confirm the specific BCM imaging of EM2198 *in vivo* has shown. These results further demonstrate that PET imaging with EM2198 aided by either $BaSO_4$-enhaned CT or MRI is a promising noninvasive approach for *in vivo* BCM assessment. Moreover, these methods can be easily translated to clinical applications.

The potential and utility of EM2198 for BCM imaging was evaluated by two additional sets of experiments to address a clinical question of whether the pancreas PET signal readouts are indicative of the progression of diabetes and to investigate the correlation between fasting blood glucose level and actual BCM loss. Both sets of experiments were carried out with the STZ-induced diabetes mouse model in a longitudinal manner for 5 weeks. We used ^{68}Ga instead of ^{64}Cu in this part of study since ^{68}Ga is a cyclotron independent isotope which can be eluted from a

[68]Ga/[68]Ge generator on a daily basis. In the first set of experiment, groups of three mice were randomly selected from the STZ-treated mice at days 0, 6, 9, 15, 18, and 35 after the STZ treatment. After the standard measurement of the fasting blood glucose level[261], the mice was injected with ^{68}Ga-NOTA-EM2198 and then sacrificed at 1 h post-injection. The pancreas tissue was excised and imaged by PET to quantify the uptake level of ^{68}Ga-NOTA-EM2198. The *ex vivo* PET signal readouts are plotted against the treatment time-course and the fasting glucose level. The fasting blood glucose level of STZ-treated mice maintained at the normoglycemic level during the first 9 days after the STZ treatment, after which it rapidly rose to the hyperglycemic level after day 15. Interestingly, the *ex vivo* PET readouts showed a reduction in tracer uptake at day 9, which was 1 week earlier than abnormally elevated fasting blood glucose level was observed. Further analysis has show the poor linear correlation (Pearson coefficient r = -0.6921; p=0.3) between *ex vivo* PET readouts and fasting blood glucose levels of the STZ-treated animals. It is notable that the trend fits in two separate linear correlation groups. This indicates that one of the two parameters has the retention phase. This observation was similar to that of the combined effect which has been described in the glucose effect model during diabetes progression[262]. This observation supports the previous statement that *ex vivo* PET readouts detects the reduction of BCM at the time points (day 6 and 9) whereas the fasting blood glucose displays normoglycemia (≤ 200 mg/dl).

To evaluate the correlation between BCM and imaging results, the *in vivo* and *ex vivo* PET signal readouts are plotted against the islet number quantified by H/E stained pancreas specimens and β-cell area (insulin-positive) from immunofluorescence stained slides at different time points after treatment with STZ. Remarkably, we observed strong correlations between *ex vivo* and *in vivo* PET imaging results and BCM parameters (islet number and insulin-positive are

in islet). A similar correlation was found between imaging results and GLP-1R expression level. Taken together, these results clearly indicate that the PET readouts (*in vivo* or *ex vivo*) using EM2198 as the imaging probe can accurately reflect the GLP-1R receptor density change during the diabetes progression. These results showed that we have established a method to indirectly evaluate small change in BCM. To correlate the *ex vivo* and *in vivo* PET result, a linear regression line of *ex vivo* PET results showed a much sharper decline compared to that of the results obtained by *in vivo* analysis. One possible reason for this is that the PET signal analyzed *in vivo* is taken from the pancreas head area (adjacent to stomach and duodenum) whereas *ex vivo* PET acquires from the entire pancreas. The heterogeneous distribution of islets throughout the pancreas is the main factor for the imaging quantification. A similar trend in islet distribution in a human pancreas has been published[263]. The human pancreatic β-cells are concentrated toward the tail of the pancreas[263]. One may argue the *in vivo* PET results were limited by the ROI selection in the mouse model. Moreover, several determinants such as normalization, partial volume effect and motion artifact might affect strongly to the imaging quantification of preclinical PET results. On the other hand, with high targeting specificity and specific activity of ^{68}Ga-NOTA-EM2198, it might be better to image BCM on a larger subject such as a pig or even in humans. However, a dose-dependent imaging study needs to be conducted to determine the optimal imaging dose to minimize the biological reactivity and the non-specific uptake of the imaging probe.

7.2. Perspective

7.2.1 Internalization of imaging probe

Our imaging target, GLP-1R, is a member of class B family of G protein-coupled receptors (GPCRs) and undergoes a rapid caveolin-1-associated endocytosis after the formation

of GLP-1/GLP-1R complex[213]. Since the probe is derived from GLP-1, the imaging mechanism is strongly relied on the specific receptor/ligand binding and the GLP-1R internalization. The metabolite of the imaging probe after internalization might be trapped in the endosome/lysosome compartment or recycled back to extracellular space within a fragmented or intact form. The irreversible trapping processes of imaging signal buildup might mislead the linear correlation between the signal intensity and the receptor density. Also, the efflux probe might act as a GLP-1R agonist and interfere the receptor/ligand binding. Therefore, it is critical to understand the internalization process and metabolite of the imaging probe.

In an ongoing study, we successfully synthesized Dylight 649-conjugated EM2198 and detected ligand distribution in mouse insulinoma cells (β-TC6) by a confocal laser scanning microscope (**Fig. 45**). The Dylight 649-conjugated EM2198 was mostly internalized and to a lesser extent on the cell membrane. A similar result was found in the cells which were stimulated with 10 nM exendin-4[213]. Further investigation of the trafficking for EM2198 by GLP-1R can be made by using either insulinoma cells transiently expressing the GLP-1R-GFP or HEK293 cells stably expressing GLP-1R-GFP. Moreover, the multifocal plane microscope might be useful to monitor the dynamic trafficking process of EM2198 in the GLP-1R recycling[264].
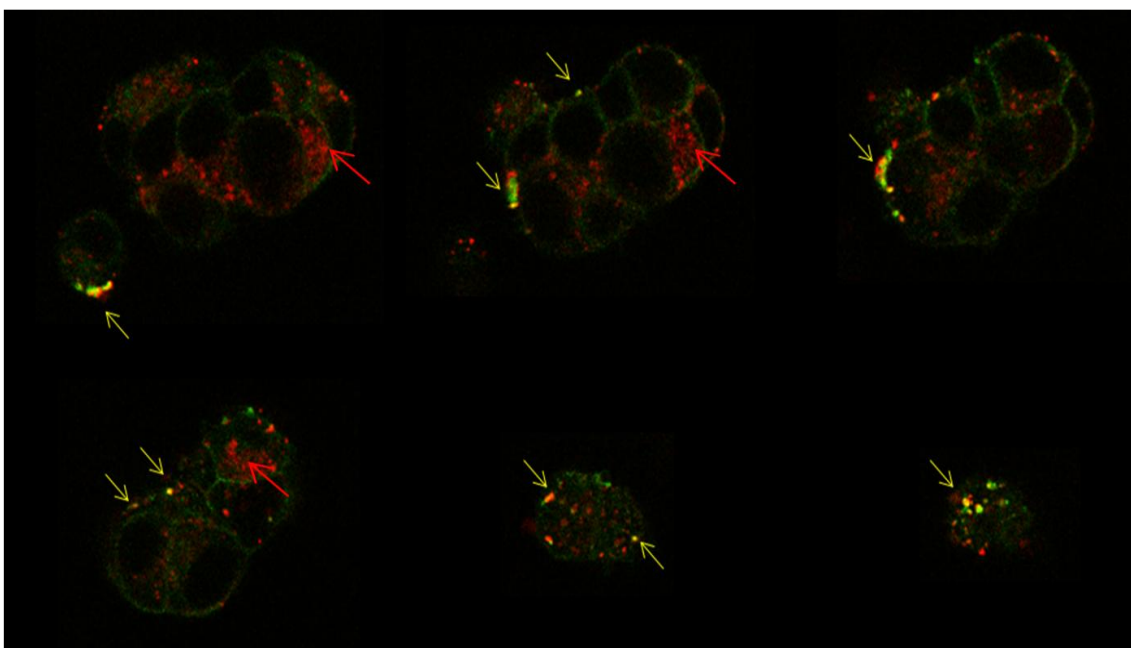
Figure 45. Confocal microscope imaging of Dylight 649-conjugated EM2198 in β-TC6 cells. Cell membrane is stained in green by a fluorescence molecule (ZIMIR)[265].Yellow arrows indicate the colocalization of EM2198 and cell membrane. Red arrows indicate the internalization of Dylight 649-conjugated EM2198.

The imaging quantification for receptor binding is strongly affected by the radiometabolite derived from imaging probe. Metabolite correction in plasma is a commonly used method in nuclear medicine imaging protocol[266]. As shown in previous results, EM2198 not only has a good stability against DPP-IV and NEP 24.11 and it also has good stability in the blood. Therefore, metabolite correction in plasma is relatively straightforward. However, this is not the only factor especially in the ligand/receptor imaging. The metabolite trapped in the targeted cells due to the receptor internalization is another concern. Currently, the liquid chromatography mass spectrometry (LC/MS)-based metabolomics has been widely used to study the intracellular metabolite[267]. With the proper processes of cell harvesting, extraction, and separation, it is possible to acquire the *in vitro* metabolite profiling[268, 269]. According to the published protocol[265], we will perform a metabolomic profiling for EM2198 in β-TC6 cells in the future. With a

successful result, we hope to gain a better understanding of the metabolites of EM2198 and the effect on ligand/receptor interaction.

7.2.2 Imaging of β-cell regeneration

One of the major limitations of imaging BCM in diabetic models is the decrease in readout signal during the disease progression. Taking into consideration of the size and the sparse distribution of BCM, it is challenging to use animal models for probe development. On the other hand, a positive readout signal might be feasible to validate the probe specificity.

In an ongoing imaging study, ^{68}Ga-NOTA-EM2198 is being used to monitor the β-cell regeneration on an inducible β-cell ablation model (PANIC ATTAC model: pancreatic islet β-cell apoptosis through targeted activation of caspase 8)[270]. This model is a chemically (dimerizer) induced diabetes model. In brief, the transgenic mouse carries the rat insulin promoter (RIP) which can drive the expression of FK506 binding protein (FKBP)–caspase 8 fusion protein by dosing the mouse with glucose *via* oral administration. After i.p. injected with dimerizer (AP20187, ARIAD Pharmaceuticals, Inc. Cat#635069), the dimerization of FKBP activates caspase 8 and triggers the apoptosis of β-cells[271].
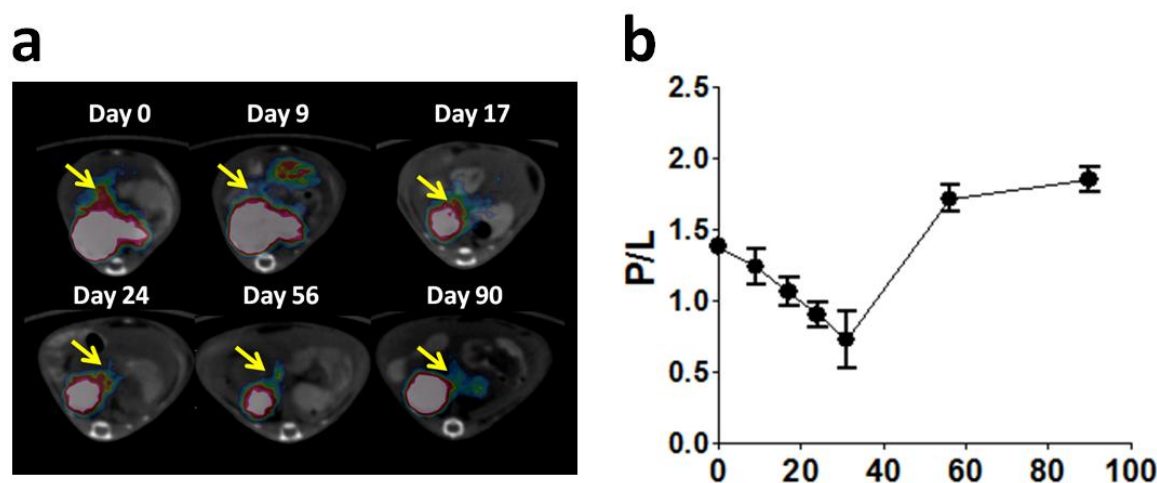
Figure 46. *In vivo* PET/CT imaging of β-cell regeneration model. (a) Representative imaging of longitudinal monitoring the BCM change in axial view. Red arrow indicates the pancreas area. (b) Imaging analysis by pancreas-to-liver uptake ratio.

In this study, PET imaging was performed before and after 9, 17, 24, 56, 90 days of dimerizer treatment. As shown in **Figure 46**, the pancreas parameter (pancreas-to-liver uptake ratio) was reduced immediately and continuously after the dimerizer-induced β-cell apoptosis. Interestingly, the recovery of pancreas-to-liver uptake ratio was observed three weeks after dimerizer treatment. *Ex vivo* imaging was performed to verify the *in vivo* findings (**Figure 47**). Based on the histology, we also observed the recovery of BCM after 48 days (**Fig. 48**). However, two results were not from the same animal. A further investigation is needed to verify the imaging results with histology from same individual. These results indicate that, ^{68}Ga-NOTA-EM2198 has the capability of monitoring the loss of BCM in STZ-induced T1D diabetes mouse model and detecting small change in β-cell regeneration.
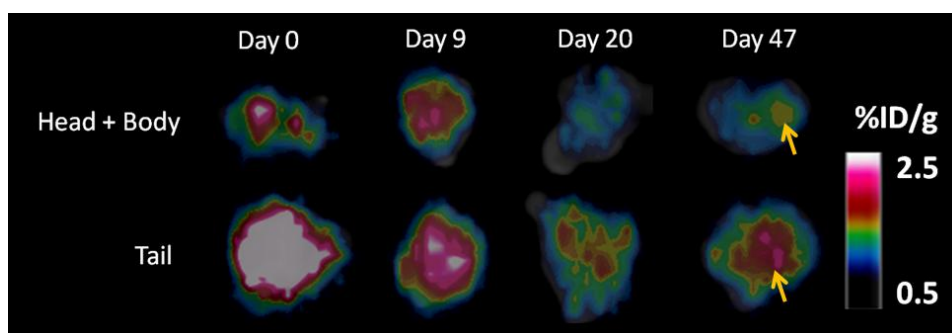
Figure 47. *Ex vivo* PET imaging of β-cell regeneration model before and after treatment. Yellow arrows indicate that *ex vivo* PET imaging with ^{68}Ga-NOTA-EM2198is able to detect the recovery of BCM.
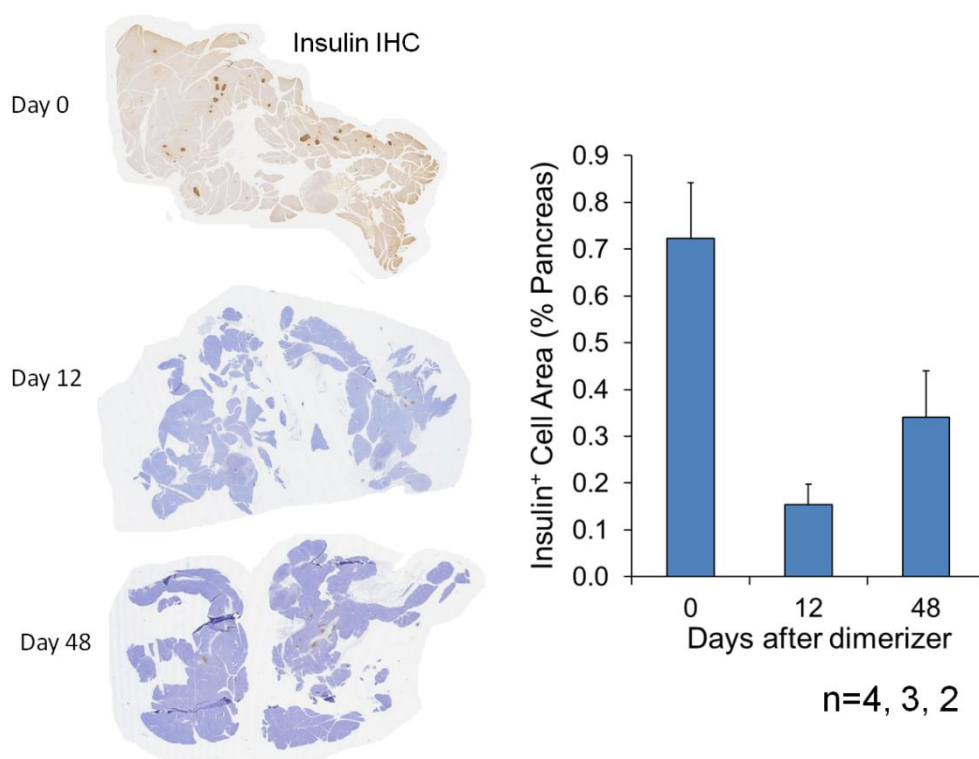
Figure 48. Immunohistochemical staining of BCM in β-cell regeneration model. Based on IHC staining for insulin, there are 20 % of BCM is recovered from the β-cells ablation (n=4, 3, and 2 at day 0, 12, and 48 after treatment)

7.2.3 Partial volume effect (PVE) correction

A general drawback of PET imaging is the limited spatial resolution which caused by positron range, small angle deviation, sensitivity, count rate capability and sampling. Especially in a preclinical imaging quantification in small animal model, its limited spatial resolution leads to partial volume effects[272]. To avoid the underestimation of the activity concentration by PVE, the size of the object should be at least three times of the instrument spatial resolution which is relatively easy to achieve in tumor imaging. In contrast, it is very difficult to avoid the PVE in the BCM imaging in mouse model due to several reasons: i) membrane-like rodent pancreas, ii) small object of BCM, and iii) activity spillover from adjacent organs. Moreover, ^{68}Ga has been used intensively in our imaging study. The high positron energy of ^{68}Ga also contributes the PVE due to the longer positron range compared to ^{18}F. Therefore, PVE correction is necessary to include in the imaging quantification. To evaluate the PVE, initially we used a National Electrical Manufacturers Association (NEMA) micro hollow sphere phantom (**Fig. 49**) including four different sphere sizes with the sphere to background activity ratio of 8:1. Imaging was performed at the center of field of view (FOV). As shown in **Figure 50**, imaging resolution and recovery coefficient of ^{18}F was much better than ^{68}Ga. Further study would be needed to evaluate the recovery coefficient of the phantom at the different PET FOVs and different sphere-to-background activity ratio[273].

Figure 49. Picture of the micro hollow sphere phantom
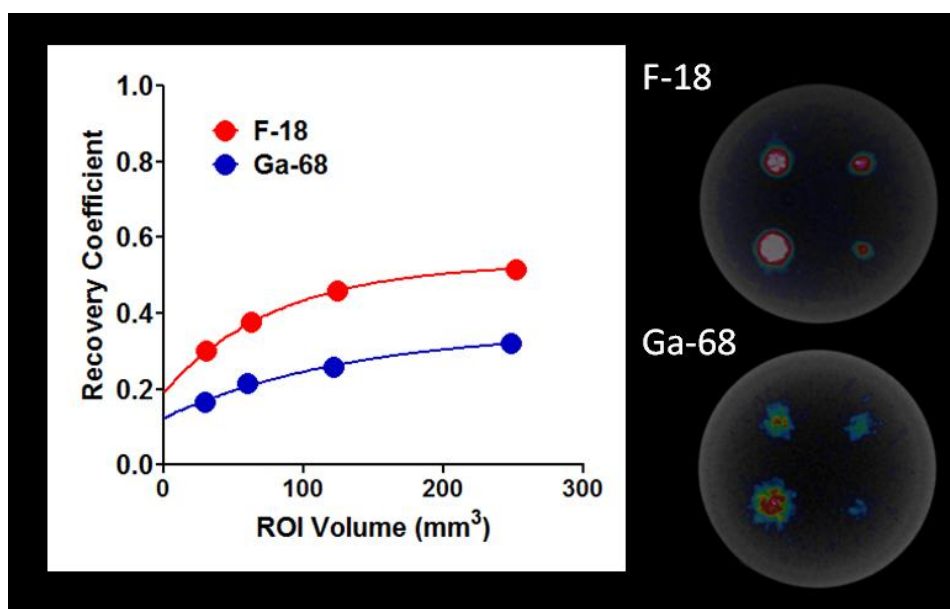
Figure 50. PVE for the different sphere sizes under contrast ratio of 8:1 for Simens Inveon small animal PET/CT system.

7.2.4 Imaging BCM in Ossabaw Mini-pigs

Due to the nature presentations of rodent pancreas and the size of the mouse, it is very difficult to have accurate imaging quantification in mouse model without compromising the limitations such as PVE and the activity spillover. We further applied the imaging technique to translational research in an obesity-prone Ossabaw miniature pig model. This is especially seen in the case of the female Ossabaw pig, where their percentage of body fat increases two-fold after 9 weeks of starting a high-fat diet[274]. They develop features of metabolic syndrome such as insulin resistance, impaired glucose tolerance, dyslipidemia, hypertension, and early coronary atherosclerosis[275]. Therefore, this model can serve as a T2D model for monitor the dynamic change of BCM. Currently, we have 6 castrated male Ossabaw pigs for the initial study. The baseline scan for the BCM imaging was performed by the injection of ~10 mCi of ^{68}Ga-NOTA-1A-EM2198 (**Scheme 3**). A 1 h dynamic PET scan was performed post-injection. As shown in **Figure 51a and b**, the preliminary data shows promising result with a 2.5-fold higher tracer activity in the pancreas compared to the liver at 60 min post-injection of ^{68}Ga- NOTA-1A-EM2198. The time activity curve shows an ideal scenario of increasing pancreas-to-liver ratio throughout the scan (**Fig. 51c**). To further evaluate the certainty of signal detection, we performed a statistical analysis on average uptake level from 30 to 60 min in pancreas, liver, and muscle from all six subjects. The mean (μ) and standard deviation (σ) of SUV (standard uptake value) in pancreas, liver, and muscle was 2.48 ± 0.28, 1.36 ± 0.24, and 0.35 ± 0.17, respectively. The signal-to-noise ratio (SNR) of each organ can be determined as the reciprocal of the coefficient of variation (μ/σ). As a result, the SNR of pancreas, liver, and muscle was 8.76, 5.68, and 2.11, respectively. If we consider liver or muscle as background, the SNR of pancreas-to-liver (P/L) and pancreas-to-muscle (P/M) was 1.81 and 7.06, respectively. As Rose criterion states that an

SNR of at least 5 is needed to be able to distinguish the image with absolute certainty by human eyes, SNR of pancreas and liver are definitely met the criteria. A similar finding is observed in P/M ratio but not the P/L ratio. Evaluation also can be made by analyzing the results with Gaussian distribution curve. As shown in **Figure 52**, it is 78.87% confidence (1.25σ) that the imaging signal is from pancreas but not from the background (liver). Although the difference between uptake levels of pancreas and liver neither met the 5σ statement as the guaranteed signal detection with 99.99994% confidence nor close to the confidence level of detection of Higgs boson, our imaging date still showed a better result compared to the BCM imaging on pig using the most successful BCM PET imaging probe, ^{18}F-labeled DTBZ (^{18}F-FE-DTBZ)[276] (**Fig. 53**). The P/L ratio of ^{18}F-FE-DTBZ displayed less than 1 at the 60 min p.i. which indicates the higher background uptake level (liver) throughout entire imaging period (**Fig. 53d**). On the other hand, our imaging result present 2.286 ± 0.875 at the 60 min p.i. (**Fig. 51 c**). Despite GLP-1R has better expression specificity on β-cells than VMAT2, our probe displays higher pancreas uptake level and better signal-to-background ratio (pancreas-to-liver) than ^{18}F-FE-DTBZ in pig model. Although the P/L ratio not reach to ideal number of > 5 (Rose criterion), based on the results, our probe still have a better chance to detect the decreasing probe accumulation in the pancreas during the diabetes progression than DTBZ-derived imaging probes.
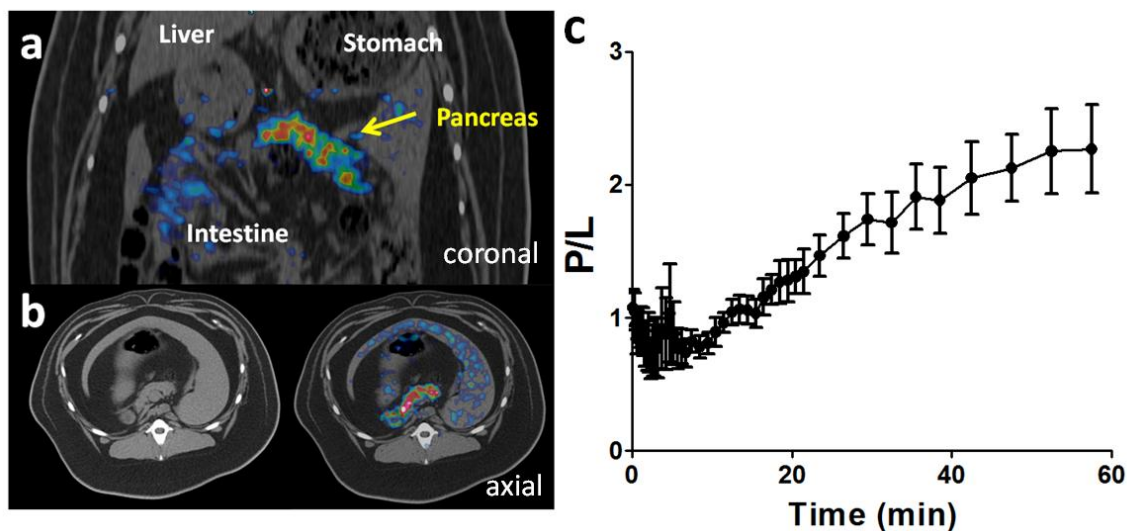
Figure 51. *In vivo* PET/CT imaging of BCM in porcine model using ^{68}Ga-NOTA-1A-EM2198. Coronal (a) and axial (b) views of the PET/CT (right) image pig scan at 60 minutes p.i.. Stomach, liver, pancreas, and intestine are identified by CT (left). (c) Time activity curve of pancreas-to-liver uptake ratio.
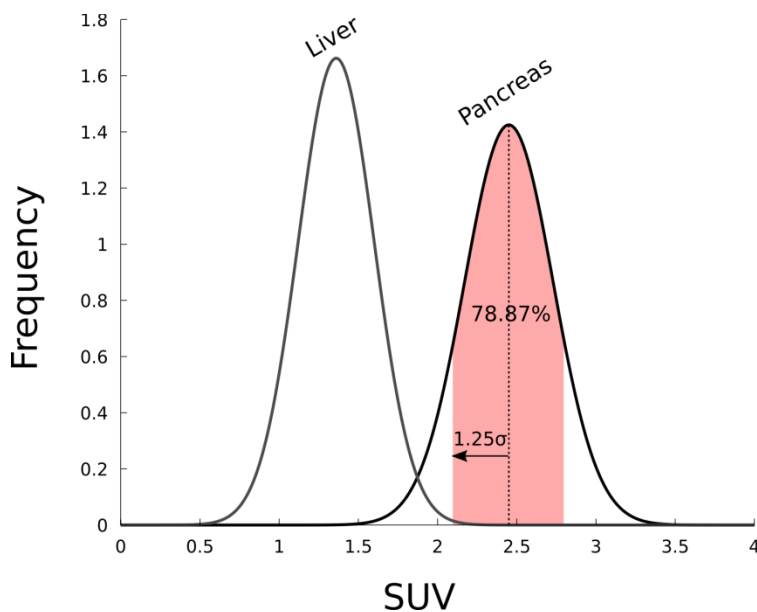
Figure 52. Signal detection from pancreas (signal) to liver (background). Red area indicate the absolute detection of pancreas uptake from pig study (n = 5).
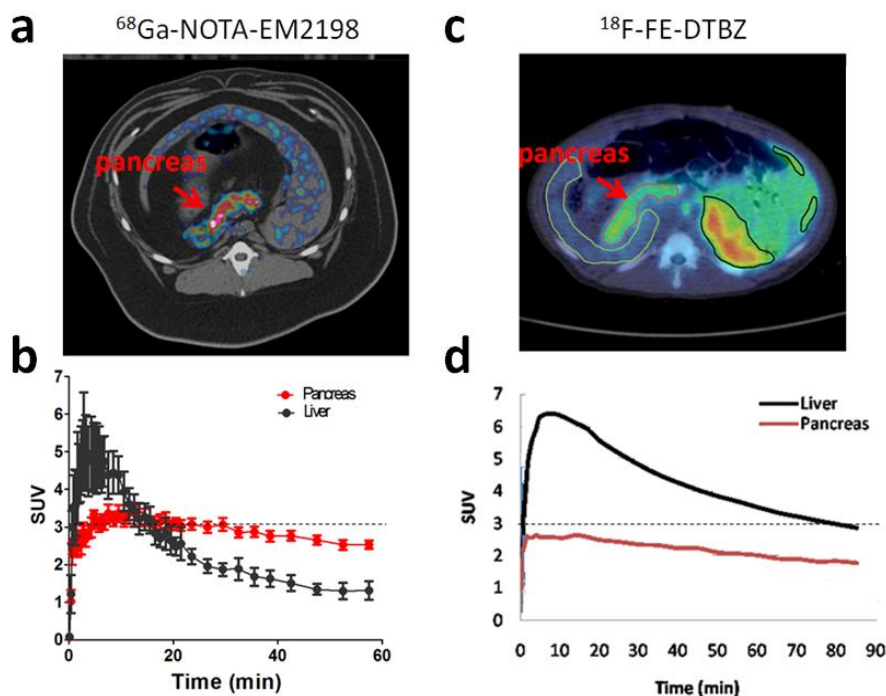
Figure 53. BCM imaging in pig model. (a) Axial view of PET/CT imaging using ^{68}Ga-NOTA-1A-EM2198 on Ossabaw mini-pig model. (b) Time activity curves of pancreas and liver (n = 6). (c) Axial view of PET/CT imaging using ^{18}F-FE-DTBZ on Male Swedish landrace piglet model. (d) Time activity curves of pancreas and liver.

7.2.5 Clinical relevancy

7.2.5.1 Clinical relevance to T1D

Currently, patients with T1D can be categorized into two types, immune-mediated and idiopathic T1D. Depending on the rate of onset, we can further categorize the immune-mediated group into sub-groups of fast- and slow-onset. Hence, the destruction of β-cells is initiated either months or years prior to the occurrence of the clinical features of disease, from which diagnosis are made On the other hand, there are no autoimmune biomarkers observed in the patients with idiopathic T1D. In fact, the clinical diagnosis such as HLA genetic typing, family history, and

blood glucose measurement is not 100% accurate. For example, HLA typing only has 50% accuracy in T1D determination. Also, 85-90% of patients with T1D are without family history. Blood glucose measurements detect positive when only less than 10% of the β-cells are still functional. Therefore, it is too far for any preventive measures to be successful. Early detection and quantification of the functional β-cell loss in mass or function *via* a noninvasive imaging technique would provide not only the opportunity for testing the accuracy of preventive measures but would a valuable tool to monitor the disease prognosis after giving any therapeutic interventions. The T1D prediction can be made by screening the genetic susceptible individual with autoanitibody measurement[277]. After detecting the positive anti-islet antibodies, noninvasive imaging technique can be used to measure the baseline level of BCM and monitor the therapeutic efficacy.

7.2.5.2 Clinical relevance to T2D

For overall diabetes cases, 90 % of the diagnosed patients are T2D. However, there are not many reliable clinical diagnosis means for T2D except glucose measurements. Although the T2D-GENES project identifies several high risk genes which relate to T2D, it is still far to be successful. Glucose measurements detects positive when over 50 % of β-cell loss. Hence, early detection of functional β-cells by noninvasive imaging techniques can help for preventing the T2D. However, the most challenging task is that the baseline level of functional β-cells varies in each individual. It is difficult to solely use the imaging techniques as the primary diagnosis tool for T2D prediction.

7.2.6 GLP-1R density change for BCM imaging during T2D

As described previously, an individual variance has set a higher challenge in evaluating the baseline level of BCM in T2D compared to T1D. What is the reason that makes T2D such complex disease? To answer this question, we have to understand the β-cell plasticity. The β-cell plasticity is balanced between expansion and involution of β-cells in response to the genetic metabolic and environmental impacts (**Fig. 54**)[278].
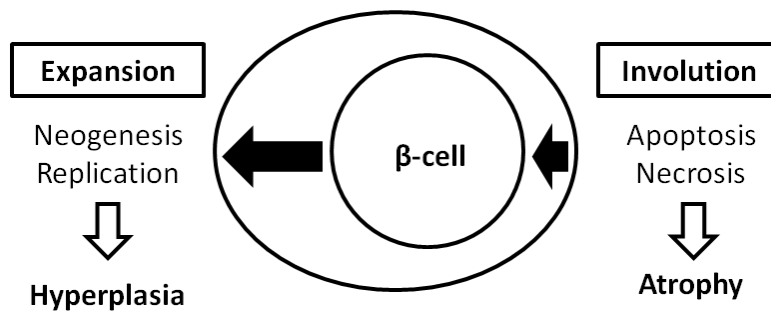
Figure 54. The dynamic balance of β-cell mass

In a normal condition, β-cells undergo fast replication at the neonatal stage and maintain stable throughout the lifespan. However, in the T2D, the balance between the involution and expansion disappears and shifts into the compensatory stage due to the increasing insulin resistance. Beta-cells then undergo hypertrophic stage by increasing the volume[279]. However, hypertrophied β-cells are more prone to apoptosis which further develops an off-balance between expansion and involution[280]. Eventually, the involution dominates the β-cell plasticity due to the β-cell apoptosis. As a result, it is very difficult to monitor an initial BCM change in T2D due to the compensatory stage varies with gender, body mass index, and age in each individual. Theoretically, it is possible to image the BCM change using highly sensitive imaging technique that we developed over the course of the project. However, the relationship between the target, GLP-1R, and the β-cell

plasticity during T2D progression is unknown. It is important to perform a quantitative analysis of GLP-1R expression in the whole human pancreas at different T2D stages such as normal, obese non-diabetic, obese T2D, and lean T2D by using stereological approach with a computer-assisted large–scale analysis[263]. To further study whether GLP-1R expression correlates to β-cell volume during T2D progression, FACS (Fluorescence-activated cell sorting) study with GLP-1R and β-cell surface markers has the potential to determine the relationship between the size and the GLP-1R expression[281]. Although there is no information about the GLP-1R expression level during T2D progression, we expect that the GLP-1R expression level in hypertrophied β-cells would be the determinant for the imaging outcome. There are three scenarios that the GLP-1R expression level is: i) dependent, ii) independent, or iii) mixture of both on the β-cell volume or surface area (**Fig. 55**). As shown in **Figure 56**, the BCM imaging outcome will depend on the GLP-1R expression during the change of β-cell plasticity throughout the course of T2D. To determine the stage of β-cell plasticity during disease progression, certain assays such as proliferating cell nuclear antigen (PCNA) or Ki67 staining (percentage of $PCNA^+/insulin^+$ or $Ki67^+/insulin^+$) and terminal deoxynucleotidyl transferase dUTP nick end labeling (TUNEL) assay can be used to indicate β-cell replication and apoptosis, respectively[282]. Also, body weight measurement is included since it is correlated to the BCM[283]. Finally, the blood glucose measurement can be used as the parameter for stages of impaired fast blood glucose (IFG) and hyperglycemia (**Fig. 56**).
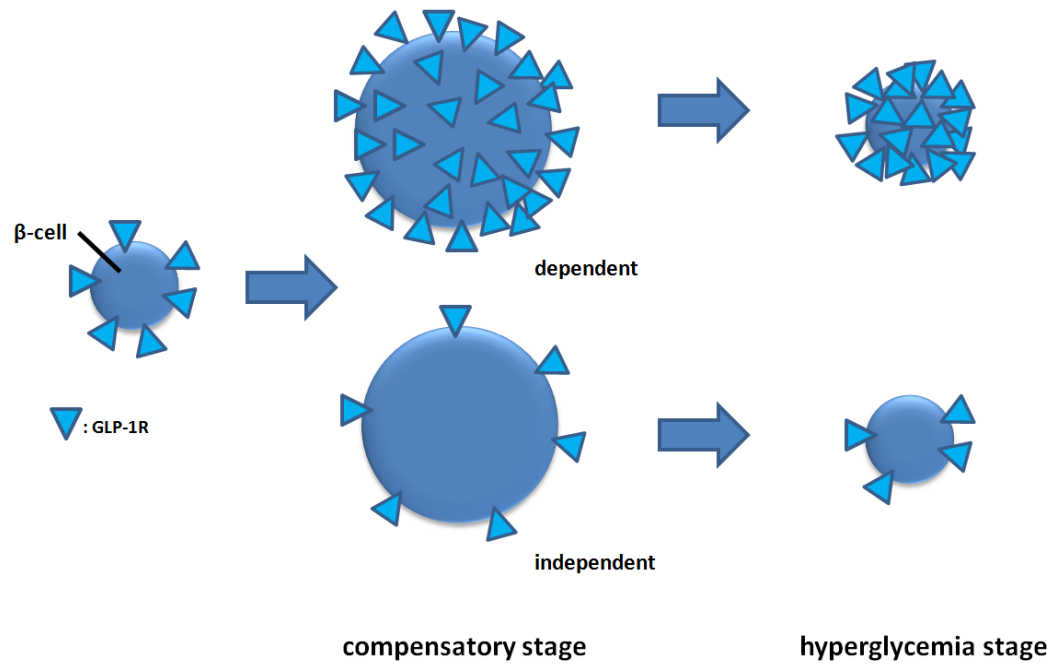
Figure 55. Assumption for GLP-1R expression during T2D progression
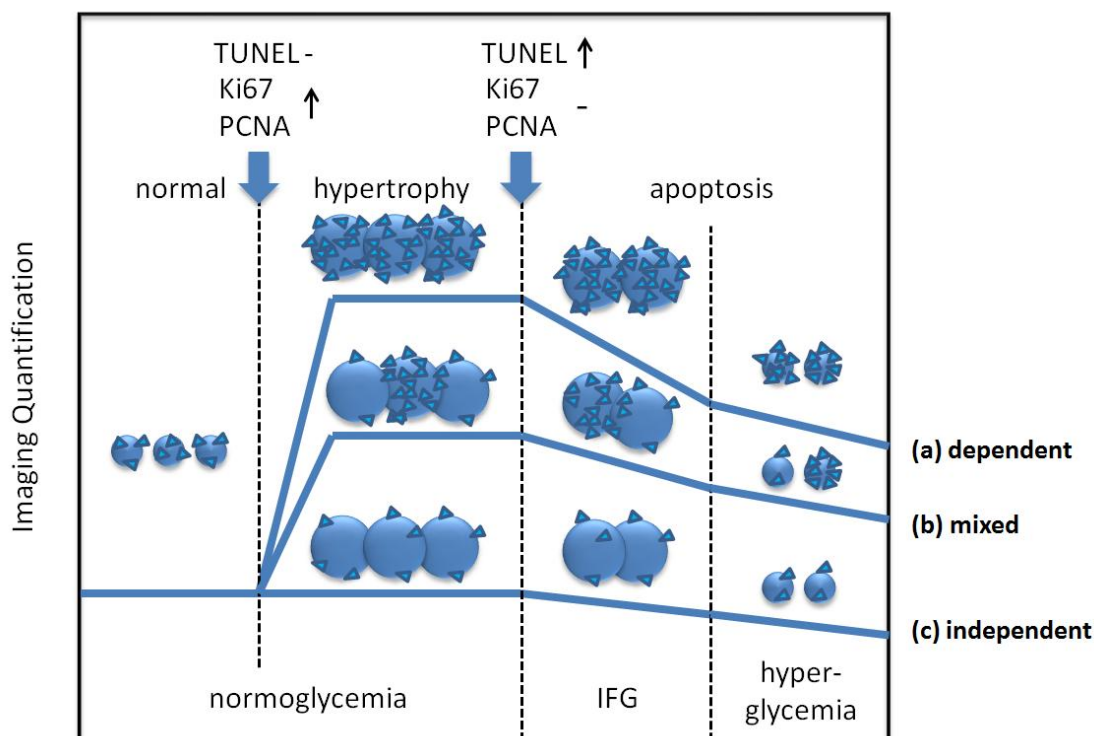
Figure 56. Imaging outcome based on the assumption of GLP-1R expression. Three blue solid lines indicate the three proposed imaging outcomes when GLP-1R expression is (a) dependent or (c) independent on β-cell volume or surface area. (b) The mixed result is also plausible. Glucose tolerance and insulin tolerance tests are used for the clinical staging. Blue triangle indicates GLP-R. TUNEL assay, PCNA, and Ki67 staining indicate the stage of β-cell plasticity. PCNA: Proliferating cell nuclear antigen staining ; TUNEL: terminal deoxynucleotidyl transferase dUTP nick end labeling; IFG: impaired fasting glucose.

7.3 Conclusion

In this dissertation, a stable bicyclic GLP-1 analog, EM2198 was selected by a two-fold screening method. A reliable and reproducible multimodality imaging technique with BaSO$_4$-enhanced CT, MRI, and PET was developed with ^{68}Ga-NOTA-EM2198 as a PET imaging probe. This imaging technique can accurately monitor the BCM change during the progression of

diabetes in a T1D-diabetes rodent model. With the high sensitivity of PET imaging, the BCM loss was detected prior to the positive symptoms which lead clinical diagnosis. The result was verified by pathological measurements for BCM and GLP-1R. With the successful translational study to a large animal model- Ossabaw pigs, PET imaging with EM2198-based probe showed the potential for clinical implementation. The significance of the work is the establishment of a system with comprehensive evaluation for an imaging probe development. The optimization of the probe design and imaging protocol can be performed on the same rodent system. It will be beneficial to the diabetes research and clinical applications in the future.

APPENDIX I

MATERIAL AND METHODS

A1.1 General

All reagents and solvents were purchased from commercial vendors and used directly unless otherwise noted. All amino acids used were of L-configuration unless otherwise stated. Milli-Q water (18 MΩ-cm) was obtained from a Millipore Gradient Milli-Q water system (Billerica, MA). Low adhesion *via*ls and Waters C18 Sep-Pak Plus Light cartridges were purchased from USA Scientific and Waters (Milford, MA), respectively. The C18 Sep-Pak Plus Lightcartridge was activated with 5 mL ethanol and 10 mL water before use. The ammonium acetate buffer (0.1 M, pH 6.5) was pretreated with Chelex 100 resin (Bio-Rad, Hercules, CA) before use. ^{64}Cu (^{64}CuCl$_2$ in 0.05N HCl) was purchased from University of Wisconsin–Madison (Madison, WI) and Washington University at St. Luis (St. Luis, Mo) with radionuclidic purity ≥ 99.90%. Reversed-phase high-performance liquid chromatography (RP-HPLC) was performed on a Waters 600E chromatography system with a Waters 2996 photodiode array detector and a Shell Jr. 1000/2000 single-channel radiation detector. The molecular weight of the peptides and their DOTA- or NOTA-conjugates were confirmed by either electrospray ionization mass spectrometry (ESI-MS) (LCQ Deca XP Plus ESI-ion trap mass spectrometer, Thermo Electron Corporation, West Palm Beach FL) or matrix-assisted laser desorption/ionization-time of flight mass (MALDI-TOF-MS) (Voyager-DE™ PRO Biospectrometry Workstation, Applied Biosystems, Foster City, CA). Basic tissue culture was performed in a Water Jacket CO$_2$/O$_2$ incubator (Thermo Scientific, Waltham, MA). Radioactivity counting was performed on a γ-counter (Perkin Elmer, Waltham, MA). Radio-TLC was performed on an raytest radioTLC system (Agilent, Santa Clara, CA).

Small animal PET-CT imaging studies were performed on a Siemens Inveon PET-CT Multimodality System (Siemens Medical Solutions Inc., Knoxville, TN)

A1.2 Animal

Animals were kept under defined-flora pathogen-free conditions at the animal facility and maintained on a 12-hour light/dark cycle with access to water and pelleted rodent chow. All animal-related experimental procedures were approved by the Institutional Animal Care and Use Committees (IACUC) of the University of Texas Southwestern Medical Center.

A1.2.1 STZ-induced T1D diabetes model

Streptozotocin solution was prepared as previously described[284]. Briefly, all animals were fasted for 6 h prior to STZ-treatment. STZ was dissolved in the freshly prepared citrate buffer pH 4.5. Mice were intraperitoneally (i.p.) administrated 60 mg/kg per day for 5 consecutive days. Disease progression was monitored based on whole body weight change, fasting plasma glucose (FPG) test, and glucose tolerance test (GTT). For the fasting plasma glucose test, mice were fasted overnight (16 h) and blood sample was collected from the tail vein. Each glucose tolerance test was performed by orally administration D-glucose (Sigma-Aldrich) at a dose of 2 g/kg (in saline) of animal and blood samples were collected at 15, 30, 45, 60, 90 min after gavaging D-glucose. Blood glucose level was measured by using glucose oxidase method with an AccuChek® blood glucose monitoring system from Roche.

A1.2.2 PANIC ATTAC model: a reversible β-cell ablation model

The transgenic model was provided by Dr. Philip Scherer at UT Southwestern Medical Center. Briefly, the transgenic mouse model used rat insulin promoter (RIP) to drive the expression of FK506 binding protein (FKBP)–caspase 8 fusion protein in a tissue-specific manner. A PCR fragment containing FKBP-caspase 8 and 3'-untranslated region was cloned into pCR4TA (Invitrogen) and then subcloned into the promoter vector. After linearization, the DNA preparation was injected into FVB embryos. Positive lines were identified by PCR genotyping. To induce the β-cell ablation, dimerizer (AP20187) was injected in homozygous male mice once a day for two consecutive days. The dose was according to the manufacturer recommendation (Ariad Pharmaceuticals). The progression of the ablation was monitored by oral glucose tolerance test.

A1.3 Peptide synthesis

A1.3.1 Solid phase peptide synthesis[201]

All of the GLP-1analogues were synthesized manually using standard N-Fmoc/tBu solid-phase peptide synthesis protocol (**Fig. 57**). Aminomethylated polystyrene resin (0.25 mmol, 0.4 mmol/g) was swollen in dimethylformamide (DMF) for 10 min and washed 3 times with DMF for 1 min. Fmoc-Rink amide linker (203 mg, 1.5 equiv), O-Benzotriazole-N,N,N',N'-tetramethyl-uronium-hexafluoro-phosphate (HBTU) (379 mg, 4 equiv), N-Hydroxybenzotriazole (HOBt) (135 mg, 4 equiv), and N,N-Diisopropylethylamine (DIEA) (0.35 mL, 8 equiv) were dissolved in DMF (3 mL). The solution was then added to the resin and incubated with shaking for 2 h. The coupling reaction was followed by Kaiser ninhydrin and TNBS tests[285-287] and unreacted amines were capped by using acetic anhydride (0.5 mL, 20 equiv) in DMF (3 mL) for 30 min. The Fmoc

protecting group of the Rink amide linker was removed *via* treatment with piperidine (20% in DMF, 1 x 5 min and 1 x 30 min) and washed three times with DMF (1 min each time). The first amino acid was introduced by using a pre-activated Fmoc amino acid that was prepared by mixing a Fmoc amino acid (4 equiv), HBTU (4 equiv), HOBt (4 equiv), and DIEA (8 equiv) in DMF (3 mL) for 30 min. The coupling reaction was conducted for 2 - 4 h or until Kaiser ninhydrin and TNBS tests became negative. When a coupling reaction was found to be incomplete, the resin was washed with DMF (3 x 1 min) and the amino acid was coupled again with a freshly prepared preactivated Fmoc amino acid. When the second coupling reaction did not result in negative Kaiser ninhydrin and TNBS tests, the resin was washed with DMF(3 x 1min) and the unreacted amines were capped by being treated with acetic anhydride (20 equiv) in DMF for 5-10 min. These steps (removal of a Fmoc group and coupling of a Fmoc amino acid) were repeated until all amino acids in the sequence of a peptide were coupled. Then, the resin was washed with DCM (5 x 1min) and dried under vacuum. A growing peptide was frequently characterized *via* cleavage of a small amount of resin and analysis of the released peptide *via* RP-HPLC and ESI-MS.
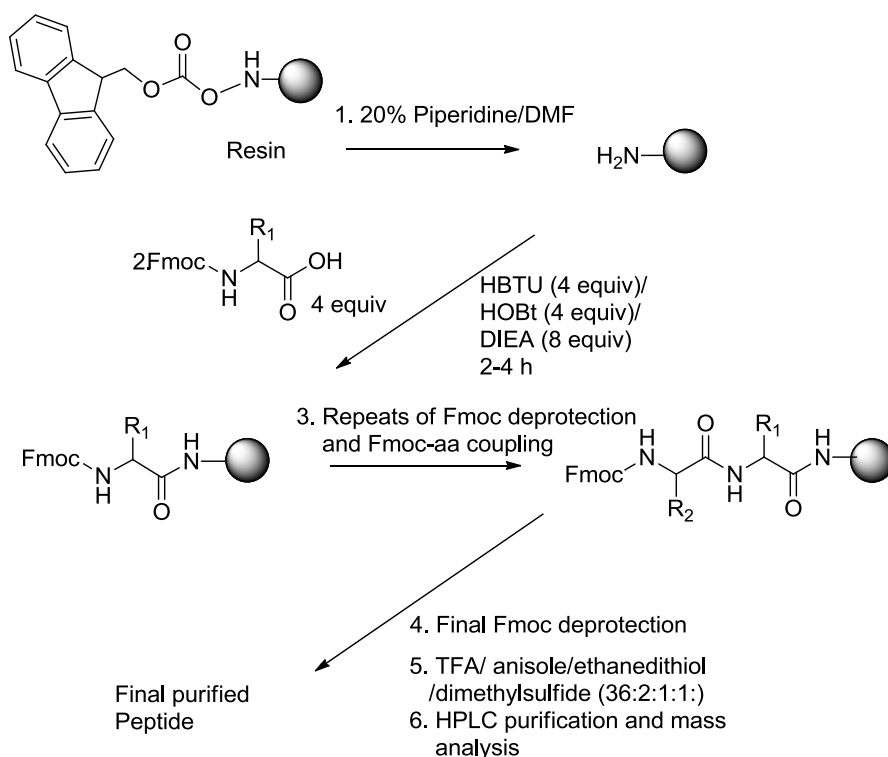
Figure 57. General procedure for Fmoc solid phase peptide chemistry

A1.3.2 On-resin formation of lactam bridges[201]

To enable on-resin lactam bridges formation, the side chains of Glu and Lys residues that were involved in lactam formation were protected with allyl protection groups. These protection groups were selectively removed while the peptide was on the solid support. Hence, a fully protected peptide still conjugated on resin (0.25 mmol), was placed in a 12 mL-polypropylene reaction vessel. The reaction vessel was then sealed with a rubber septum and flushed with nitrogen for 10 min. To the reaction vessel, Pd(PPh$_3$)$_4$ (30 mg, 0.1 equiv), and DMBA (390 mg, 10 equiv) dissolved in degassed DCM/DMF (4 mL, 3:1) was delivered by a syringe and the reaction mixture was kept under nitrogen for 30 min with occasional shaking. The resin was washed with LiCl/DMF (0.8 M, 3 × 1 min) and the reaction was repeated again. The resin was

then treated with PyBOP/HOBt/DIEA (6, 6, and 12 equiv) or BOP/HOBt/DIEA (6, 6, and 12 equiv) dissolved in DCM/DMF/NMP (1:1:1, 1% Triton X100) for 6-8 h until the reaction was complete (**Figure 58**). The resin was washed with DMF (3 × 1 min).
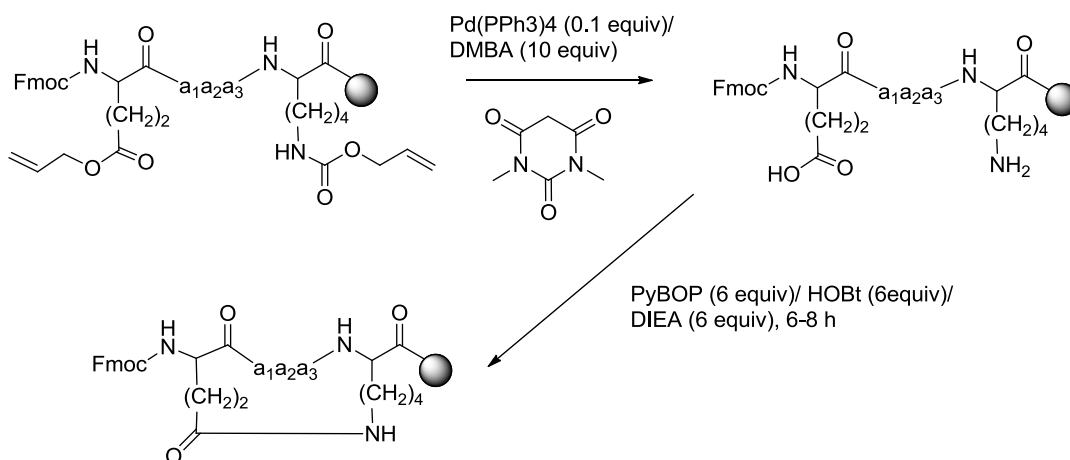
Figure 58. General procedure for on-resin lactam formation.

A1.3.3 Cleavage and final deprotection of peptides[201]

A cleavage mixture of trifluoroacetic acid (TFA), dimethylsulfide, 1,2-ethanedithiol, and anisole (20 mL, 36:1:1:2) was added to a peptide on dried resin (0.25 mmol) in a disposable 50 mL-polypropylene tube, and the mixture was stirred for 90 min at room temperature in the dark. The TFA solution was filtered, and the resin was washed with TFA (2 mL) and DCM (2 mL). The combined TFA solution was concentrated to a volume of approximately 3 mL with a gentle stream of nitrogen, and the peptide was precipitated with cold diethyl ether (40 mL). The precipitated peptide was centrifuged and the ether solution was carefully decanted to remove the

scavengers. Washing with cold diethyl ether was repeated and the precipitated peptide was centrifuged, decanted and dried under vacuum.

To monitor the progress of peptide synthesis, a small amount of resin (approximately 20 mg) was collected and treated with the cleavage mixture (2 mL) for 90 min at room temperature in the dark. The TFA solution was filtered and concentrated to a volume of approximately 0.5 mL with a gentle stream of nitrogen. The peptide was then precipitated with cold diethyl ether (10 mL) and the centrifuged peptide was washed with diethyl ether again. The peptide was dried under vacuum followed by HPLC and ESI-MS analysis.

A1.5 *In vitro* cellular study

A1.5.1 Receptor potency[201]

The receptor potency of GLP-1 analogs was determined by the accumulation of cyclic AMP (cAMP) in HEK293 cells overexpressing human GLP-1R in the presence of a phosphodiesterase inhibitor, 3-isobutyl-1-methylxanthine (IBMX) as described previously[213]. For dose-response experiments, cells were treated with a peptide for 20 min at 37°C. In all cases, reaction were terminated with trichloroacetic acid (1.2 M), and accumulated cAMP was isolated by the two-column chromatographic method[288]. The half maximal effective concentration (EC50 values) was used to evaluate the receptor potency. EC50 value was determined by the curve fitting using GraphPad Prizm program (version 5.0, San Diego, CA).

A1.5.2 Enzymatic stability[201]

The enzyme stability of GLP-1 analogs was determined by following the previously reported procedure[201]. Briefly, GLP-1 analog (100 µg) was incubated with recombinant human DPP-IV enzyme (0.2 ng/mL) in Tris buffer (25 mM, pH 8.0) or NEP 24.11 enzyme (1.0 µg/mL) in HEPES buffer (50 mM, pH 7.4, 50 mM NaCl) at 37°C. At 0, 2, 3, 4, 6, 9, 24, 48, and 96 h, an aliquot of the solution (100 µL) was quenched with aqueous TFA (10%, 20 µL) and analyzed by HPLC [elution gradient, 10 to 90% ACN in aqueous trifluoroacetic acid (0.1%) over 40 min; C18-bonded column, Zorbax C-18, 4.6 mm x 250 mm]. The concentrations of intact and degraded peptides were determined on the basis of their peak areas relative to that of an internal standard, and their half-lives were calculated by nonlinear regression *via* GraphPad Prism version 5.0.

A1.5.3 Competitive receptor binding assays

Mouse insulinoma cells, β-TC-6 cells (CRL-11506, ATCC), were seeded in a poly-D-lysine coated 48-well plate (BD Biosciences, San Jose, CA) with 5×10^5 cells per well prior to the study. After overnight incubation in a 37°C incubator, culture medium was removed and cells were rinsed briefly with cold PBS. After PBS rinse, peptide candidates was diluted in the concentrations range from 10^{-4} to 10^{-12} M was added together with the tracer ^{125}I-exendin (7-39) (PerkinElmer) (~15,000 cpm) into culture plate with 150 µl of total volume (n=4). Competitive receptor binding study was performed at 4°C for 4 h. Binding medium (DMEM culture medium without fetal bovine serum) with peptide candidates were removed after 4 h of incubation and followed by twice cold PBS rinsing to remove non-specific binding. Cells were then lysed by adding 0.5 N NaOH for 15 min at room temperature. Binding medium, washing PBS, and cell

lysate were collected separately for radioactivity counting on a gamma counter (PerkinElmer). All the data were analyzed by GraphPad Prism 5.0.

A1.5.4 Cellular internalization and efflux of ^{67}Ga-NOTA-EM2198

Mouse insulinoma cells (β-TC6) were obtained from American Type Culture Collection and cultured in DMEM media containing, supplemented with 10% heat-inactivated fetal bovine serum (FBS) and penicillin/streptavidin. The cells were incubated at 37°C in 100 cm^3 tissue culture flasks under a humidified 5% CO2 atmosphere. The culture media were changed every four days. Cellular internalization and efflux of ^{67}Ga-NOTA-EM2198 were evaluated in β-TC6 cells. For internalization study, β -TC6 cells (5×10^5/well) were seeded into a 48-well cell culture plate and incubated at 37°C overnight. After being washed once with binding media (DMEM without FBS), the cells were incubated at 37°C for at 0, 15, 30, 45, 60, 90, 120, 360, and 1440 min (n=4) in the presence of approximately 15,000 counts per minute (cpm) of purified ^{67}Ga-NOTA-EM2198. After incubation, the reaction medium was collected and cells were rinsed with 2 × 0.5 mL of ice-cold pH 7.4, 0.01 M PBS. Cellular internalization of ^{67}Ga-NOTA-EM2198 was assessed by washing the cells with acidic buffer [40 mM sodium acetate (pH 4.5) containing 0.9% NaCl and 0.2% BSA] to remove the membrane bound radioactivity. The remaining internalized radioactivity was obtained by lysing the cells with 0.5 mL of 1N NaOH for 5 min. Membrane-bound and internalized ^{67}Ga activity was counted in a gamma counter. Cellular efflux of ^{67}Ga-NOTA-EM2198 was determined by incubating β-TC6 cells with ^{67}Ga-NOTA-EM2198 for 3 h at 37°C, removing non-specific bound activity with 2 × 0.5 mL of ice-cold pH 7.4, 0.01 M PBS rinse, and monitoring radioactivity released into cell culture media. The radioactivity in

media, on cell surface and in cells were separately collected and counted in a gamma counter 0, 15, 30, 45, 60, 90, 120, 360, 900, and 1440 min post incubation in the culture media.

A1.5.5 Confocal laser scanning microscopy (CLSM) imaging of cellular internalization of Dylight 649-conjugated EM2198

Cellular internalization of Dylight 649-conjugated -EM2198 was evaluated in β-TC6 cells. For cell imaging, we cultured cells in 35-mm Petri dishes with glass bottoms (MatTek). Cells were incubated with Dylight 649-conjugated EM2198 (20 nM) at 4 °C for 3 h and washed with SAB before imaging. To label the cell membrane, cells were washed with a secretion assay buffer (SAB: containing 114 mM NaCl, 4.7 mM KCl, 1.2 mM KH_2PO_4, 2.5 mM $CaCl_2$, 1.16 mM $MgSO_4$, 3 mM glucose, and 20 mM Hepes, pH 7.4). The DMSO stock solution of ZIMIR[265] (1–2 mM) diluted in a small volume of SAB was added to cells to a final concentration of 1 μM. Cells were imaged with CLSM using an LSM510 imaging system (Carl Zeiss) and a 40× oil immersion objective at 25°C.

A1.7 Chemistry

A1.7.1 Synthesis of NOTA-maleimide

To synthesize NOTA-maleimide, bifunctional chelator, p-SCN-Bn-NOTA (Macrocyclics, TX) (5 mg, 8.94 μmol), was added to a solution of N-(2-aminoethyl)maleimide trifluoroacetate (Sigma Aldrich, MO) (9 mg, 35.4 μmol,) in 250 μl of anhydrous dimethyl sulfoxide (DMSO). To the resulting mixture, 5 μl of basic additive N,N,-diisoproprylethylamine (DIPEA) was added and the reaction mixture was left on a constant rotor for overnight. The crude reaction mixture was

purified by HPLC with a Waters XTerra C18 column (5 µm, 4.6 mm × 150 mm). The flow rate was set at 1 mL/min using a gradient system starting from 80% solvent A by a linear ramp to 100% solvent B at 40 min. Solvent A: 0.1% trifluoroacetic acid (TFA) in water (v/v); solvent B: 0.1% TFA in acetonitrile (v/v). The collected fractions were pooled together and lyophilized to give bifunctional chelator, NOTA-maleimide as a white powder in 75% yield. The compound was characterized by MS ([M+H]$^+$cal'c 590 m/z, found 591 m/z).

A1.7.2 Synthesis of DOTA- or NOTA-GLP-1 analogs

Prior to the reaction, all solution was flushed with inert gas to minimize the oxygen content in the solution. The DOTA-EM2198 and NOTA-EM2198 conjugates were obtained by reacting the peptide construct with a C-terminal Cys (0.5 µmol) with bifunctional chelators, maleimidomono-amide-DOTA (DOTA-maleimide)(Macrocyclics, TX) and maleimidomono-amide-NOTA(NOTA-maleimide)(2.5 µmol; molar ratio: 5:1), respectively, in 10 mM PBS (pH 6.4, containing 10 mM EDTA) *via* thiol-maleimide reaction at room temperature (RT) for 2 h. The DOTA-EM2198 was purified by HPLC with a Waters XTerra C18 column (10 µm, 4.6 mm × 250 mm). The flow rate was set at 4 mL/min using a gradient system starting from 80% solvent A by a linear ramp to 100% solvent B at 40 min. Solvent A: 0.1% trifluoroacetic acid (TFA) in water (v/v); solvent B: 0.1% TFA in acetonitrile (v/v). The purified fractions were characterized by MALDI-MS with α-cyano-4-hydroxycinnamic acid. The purity of the product was >99 %.

A1.7.3 Synthesis of EM2198 on multimeric NOTA scaffold

R= OH

NOTA ^{t}Bu$_3$-COOH: X$_1$ = R, X$_2$, X$_3$ = H, X$_4$ = ^{t}Bu
NOTA ^{t}Bu$_3$-(COOH)$_2$: X$_1$, X$_2$ = R, X$_3$ = H, X$_4$ = ^{t}Bu
NOTA ^{t}Bu$_3$-(COOH)$_3$: X$_1$, X$_2$, X$_3$ = R, X$_4$ = ^{t}Bu

H$_2$N | EDC, Et$_3$N
           | DMF

R=

NOTA ^{t}Bu$_3$-Mal: X$_1$ = R, X$_2$, X$_3$ = H, X$_4$ = ^{t}Bu
NOTA ^{t}Bu$_3$-(Mal)$_2$: X$_1$, X$_2$ = R, X$_3$ = H, X$_4$ = ^{t}Bu
NOTA ^{t}Bu$_3$-(Mal)$_3$: X$_1$, X$_2$, X$_3$ = R, X$_4$ = ^{t}Bu

PBS | HS·Cys-EM2198

R: EM2198

R=   S·Cys-EM2198

NOTA ^{t}Bu$_3$-EM2198:   X$_1$ = R, X$_2$, X$_3$ = H, X$_4$ = ^{t}Bu
NOTA ^{t}Bu$_3$-(EM2198)$_2$: X$_1$, X$_2$ = R, X$_3$ = H, X$_4$ = ^{t}Bu
NOTA ^{t}Bu$_3$-(EM2198)$_3$: X$_1$, X$_2$, X$_3$ = R, X$_4$ = ^{t}Bu

TFA

NOTA-1A-EM2198:   X$_1$ = R, X$_2$, X$_3$ = H, X$_4$ = H
NOTA-2A-(EM2198)$_2$: X$_1$, X$_2$ = R, X$_3$ = H, X$_4$ = H
NOTA-3A-(EM2198)$_3$: X$_1$, X$_2$, X$_3$ = R, X$_4$ = H

A1.7.3.1 NOTA ^{t}Bu$_3$-Mal

To a mixture of NOTA tBu3-COOH (5.0 mg, 9.1 µmol) ethylaminomaleimide (25.0 mg, 10.0 mmol) and 1-Ethyl-3-(3-dimethylaminopropyl)carbodiimide (EDC, 5.0 mg, 15.0 µmol) in 500 µL of dry DMF was added N, N-diisopropylethylamine (DIPEA, 100 µL), resulting solution was stirred under N2 for 24 h. Solvents were removed, and the crude product was purified by semi-preparative reverse-phase HPLC. The collected fractions from multiple runs were pooled and

lyophilized to give NOTA tBu3-Mal as a white solid (3.7 mg; yield: 61%). MALDI-TOF/MS: found: 666.7 [M+H]$^+$.

A1.7.3.2 NOTA ^{t}Bu$_3$-(Mal)$_2$

To a mixture of NOTA ^{t}Bu$_3$-(COOH)$_2$ (5.0 mg, 8.1 µmol) ethylaminomaleimide (25.0 mg, 10.0 mmol) and 1-Ethyl-3-(3-dimethylaminopropyl)carbodiimide (EDC, 5.0 mg, 15.0 µmol) in 500 µL of dry DMF was added N, N-diisopropylethylamine (DIPEA, 100 µL), resulting solution was stirred under N$_2$ for 24 h. Solvents were removed, and the crude product was purified by semi-preparative reverse-phase HPLC. The collected fractions from multiple runs were pooled and lyophilized to give NOTA ^{t}Bu$_3$-(Mal)$_2$ as a white solid (3.1 mg; yield: 45%). MALDI-TOF/MS: found: 860.7 [M+H]$^+$.

A1.7.3.3 NOTA ^{t}Bu$_3$-(Mal)$_3$

To a mixture of NOTA ^{t}Bu$_3$-(COOH)$_3$ (5.0 mg, 7.2 µmol) ethylaminomaleimide (25.0 mg, 10.0 mmol) and 1-Ethyl-3-(3-dimethylaminopropyl)carbodiimide (EDC, 5.0 mg, 15.0 µmol) in 500 µL of dry DMF was added N, N-diisopropylethylamine (DIPEA, 100 µL), resulting solution was stirred under N$_2$ for 24 h. Solvents were removed, and the crude product was purified by semi-preparative reverse-phase HPLC. The collected fractions from multiple runs were pooled and lyophilized to give NOTA ^{t}Bu$_3$-(Mal)$_3$ as a white solid (2.5 mg; yield: 33%). MALDI-TOF/MS: found: 1054.4 [M+H]$^+$.

A1.7.3.4 NOTA (^{t}Bu)$_3$-EM2198

NOTA (^{t}Bu)$_3$-Mal (1.0 mg, 1.5 µmol) was dissolved in 1:1 solution of 10 mM PBS solution containing 10 mM EDTA (250 µL, pH = 7.0) and ACN (250 µL). A 30 µL of the resulting solution was added to a solution of EM2198 (0.25 mg, 0.07 µmol) in 10 mM PBS solution containing 10 mM EDTA (100 µL, pH = 7.0). The reaction mixture was stirred at room temperature for 12 h under N$_2$. The reaction mixture was purified by semi-preparative reverse-phase HPLC. The collected fractions from multiple runs were pooled and lyophilized to give protected NOTA (^{t}Bu)$_3$-EM2198 as white solid. MALDI-TOF/MS: found: 4339 [M+H]$^+$.

A1.7.3.5 NOTA (^{t}Bu)$_3$-(EM2198)$_2$

NOTA (^{t}Bu)$_3$-(Mal)$_2$ (2.0 mg, 2.9 µmol) was dissolved in 1:1 solution of 10 mM PBS solution containing 10 mM EDTA (250 µL, pH = 7.0) and ACN (250 µL). A 5.0 µL of the resulting solution was added to a solution of EM2198 peptide (0.25 mg, 0.07 µmol) in 10 mM PBS solution containing 10 mM EDTA (100 µL, pH = 7.0). The reaction mixture was stirred at room temperature for 12 h under N$_2$. The reaction mixture was purified by semi-preparative reverse-phase HPLC. The collected fractions from multiple runs were pooled and lyophilized to give protected NOTA (^{t}Bu)$_3$-(EM2198)$_2$ as white solid. MALDI-TOF/MS: found: 8153 [M+H]$^+$.

A1.7.3.6 NOTA (^{t}Bu)$_3$-(EM2198)$_3$

NOTA (^{t}Bu)$_3$-(Mal)$_3$ (1.5 mg, 1.4 µmol) was dissolved in 1:1 solution of 10 mM PBS solution containing 10 mM EDTA (250 µL, pH = 7.0) and ACN (250 µL). A 6.5 µL of the resulting solution was added to a solution of EM2198 peptide (0.25 mg, 0.07 µmol) in 10 mM PBS solution containing 10 mM EDTA (100 µL, pH = 7.0). The reaction mixture was stirred at room

temperature for 12 h under N_2. The reaction mixture was purified by semi-preparative reverse-phase HPLC. The collected fractions from multiple runs were pooled and lyophilized to give protected NOTA (^{t}Bu)$_3$-(EM2198)$_3$ as white solid. MALDI-TOF/MS: found 11995 [M+H]$^+$.

A1.7.3.7 Deprotection

The protected conjugates, NOTA (^{t}Bu)$_3$-EM2198, NOTA (^{t}Bu)$_3$-(EM2198)$_2$, and NOTA (^{t}Bu)$_3$-(EM2198)$_3$ were dissolved in TFA and stirred at room temperature for 12 h. Solvent was evaporated and the residue was purified by semi-preparative reverse-phase HPLC. The collected fraction of multiple runs were pooled and lyophilized to afford product as white solid. MALDI-TOF/MS: NOTA (^{t}Bu)$_3$-EM2198: found 4206 [M+H]$^+$, NOTA (^{t}Bu)$_3$-(EM2198)$_2$: found: 7801 [M+H]$^+$, and NOTA (^{t}Bu)$_3$-(EM2198)$_3$ found: 11995

A1.8 Radiochemistry

A1.8.1 Radiolabeling ^{64}Cu

For ^{64}Cu-DOTA-EM2198 radiosynthesis, 10 μg of the DOTA-EM2198 conjugate was reconstituted with 100 μL of 0.1 M ammonium acetate (pH 6.5) solution and added with 1.5-2.3 mCi of ^{64}CuCl$_2$ in 0.05 N HCl. The reaction mixture was incubated at 80 ^{o}C for 30 min in a thermomixer with constant shaking at 900 rpm. After 30 min of incubation, DTPA was added to remove the non-specifically bound or free ^{64}Cu from mixture. Purification of ^{64}Cu labeled conjugate was achieved by passing the mixture through a preconditioned C-18 cartridge (C-18 Sep-Pak light, Waters). The cartridge was then washed with 5 mL of H$_2$O (Milli-Q). The ^{64}Cu

labeled conjugate was eluted with 80% ethanol in PBS and the radiochemical purity was confirmed by radio-HPLC analysis.

A1.8.2 Radiolabeling of ^{68}Ga

^{68}GaCl$_3$ was eluted from a ^{68}Ge/^{68}Ga generator with 0.6 N HCl and the pH was adjusted to 3-4 with 1M HEPES (4-(2-hydroxyethyl)-1-piperazineethanesulfonic acid). The ^{68}GaCl$_3$ solution (1 mL, 10 mCi) was then mixed with 10 µg of NOTA-EM2198 and the mixture was incubated at 75°C for 15 min with constant shaking (900 rpm). Preconditioned C-18 Sep-Pak cartridge was used to separate the free ^{68}Ga ion from the reaction mixture. After passing the reaction mixture through the Sep-Pak cartridge, the cartridge was then washed with 5 mL of H$_2$O (Milli-Q) and ^{68}Ga radiolabeled NOTA-EM2198 was eluted by 500µl of 80% ethanol in PBS. Radiochemical yield and purity of ^{68}Ga-NOTA-EM2198 were evaluated using radio-HPLC. Excess ethanol was removed by nitrogen flow for the *in vivo* study.

A1.9 *In vivo* evaluations

A1.9.1 Pharmacokinetic study

A single dose of ^{67}Ga-NOTA-EM2198 (10 µCi) was administered in the tail vein. Blood samples were taken *via* retro-orbital sinus under anesthesia with isoflurane at 0, 2, 5, 15, 30, 60, 90, 120, 240 min as well as 24 h after dose administration. At each time point the blood of three mice was collected and weighted. Radioactivity was measured by a gamma counter (n=3).

A1.9.2. Biodistribution

Each mouse was weighed and i.v. injected with 10 μCi of ^{64}Cu-labeled NOTA-L-GLP-1 or EM2198. The mice were anesthetized and sacrificed at 1 h p.i. (n =4). Blood, lung, liver, spleen, kidney, muscle, fat, heart, stomach, intestines, and pancreas were collected, weighed, and counted by a γ-counter. The percentage of injected dose per gram (%ID/g) for each sample and the standard de*via*tion (SD) for each group of the organ were determined by comparing the standards (n = 3) prepared along with the injection doses.

A1.9.3 *Ex vivo* blood stability studies

Normal mice were injected with 50-100 μCi of the ^{64}Cu labeled DOTA-conjugated-D-GLP-1 or EM2198 *via* the tail vein. At 1 and 4 h p.i., the mice were euthanized and sacrificed. The blood and kidneys were collected in 80% ethanol (2 mL) in ice bath. All samples were centrifuged at 2,000g for 5 min, followed by filtration of the supernatant. The supernatant was analyzed by HPLC.

A1.10 Molecular imaging techniques
A1.10.1 L-lysine administration for reducing renal uptake

L-lysine solution was used to reduce the renal uptake in order to reduce the background or nonspecific activity from kidneys. L-lysine solution was prepared by dissolving 2.5g L-lysine with 50ml of PBS and adjusting pH level to 7.4 by HCl. The animal was i.p. injected twice with 400 mg/kg of L-lysine with a 30 min interval prior to PET/CT imaging study.

A1.10.2 Barium sulfate administration for pancreas

Clinically used BaSO$_4$solution (Readi-CAT® 2, Ez EM, Lake Success, NY) was used to enhance the gastrointestinal tract (GI tract) in order to assist the identification of pancreas in mouse. The animal was orally administration 500 µl of BaSO$_4$ with a 30 min interval prior to PET/CT imaging study.

A1.10.3 Small animal PET/CT imaging

The PET/CT imaging studies were performed on a Siemens Inveon Multimodality PET/CT system (Siemens Medical Solutions Inc., Knoxville, TN, USA). Ten minutes prior to imaging, the animals were anesthetized using 3% isofluorane at room temperature until stable vitals were established. Once the animal was sedated, the animal was placed onto the imaging bed under 2% Isofluorane anesthesia for the duration of the imaging. The CT imaging was acquired at 80 kV and 500 µA with a focal spot of 58µm. The total rotation of the gantry was 360° rotation, 360 rotation steps were obtained at an exposure time of approximately 145 ms/frame. The images were acquired using a charge-coupled device (CCD) readout of 4,096 × 3,968 binning of 4 and an average frame of 1. Under low magnification, the effective pixel size was 102.10 µm. The CT scan time was approximately 6 min. CT image was reconstructed by a down sample factor of 2, using Cobra Reconstruction Software. The PET imaging was acquired directly following the acquisition of CT data. Each animal was injected with 100 - 150 µCi of a ^{68}Ga- or ^{64}Cu-labeled GLP-1 analog in 150 µL of saline *via* tail vein. *In vivo* imaging was performed 45 min p.i. whereas *ex vivo* imaging was 1 h p.i.. Fifteen minutes static PET imaging data were reconstructed into single frame (15 min average image). PET images were reconstructed using Fourier

Rebinning and Ordered Subsets Expectation Maximization 2D (OSEM2D) algorithm. Reconstructed CT and PET images were fused and analyzed using Inveon Research Workplace (IRW) software. For quantification, regions of interest were guided by visual inspection of CT images. Pancreas area was identified by CT-highlighted GI tract and kidney (**Fig. 59**). The resulting quantitative data were expressed in %ID/g.
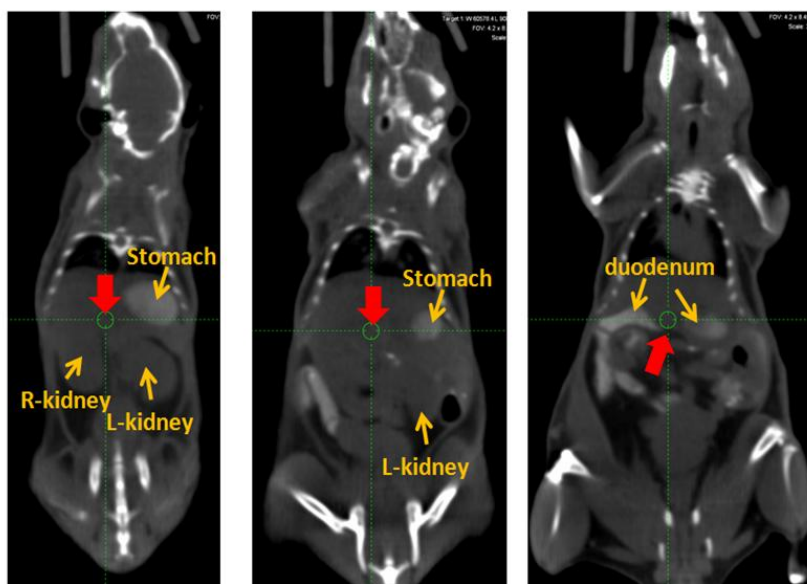
Figure 59. BaSO$_4$-enhanced CT for identification of pancreas area.

A1.10.4 Small animal Magnetic Resonance Imaging (MRI)

MR imaging was conducted using a 7-T small animal MR system (Varian, Inc, Palo Alto, CA) with a 40 mm internal diameter (I.D.) Horizontal Millipede™ Coil. All animals were anesthetized with 1-2% isoflurane (AERRANE, Baxter Healthcare Corporation, IL) mixed with 100% oxygen and placed in an animal bed, head first with the abdomen centered with respect to the center of the RF coil in the supine position with a respiratory sensor. In the beginning, low-

resolution multi-slice imaging was performed on the abdominal region to confirm the location of the pancreas in which the kidneys and spleen could be the anatomical markers. Based on this image, proton density (PD)-T1-mixed weighted multi-slice images encompassing the entire pancreas were obtained with a respiratory-gated fast spin-echo sequence in the axial plane (repetition time / echo time, 1450/10.21 msec; 17 slices; field of view, 30×30 mm; matrix, 256×256 matrix; slice thickness, 0.5 mm; gapless; number of excitations, 8). The imaging was repeated twice without gap between two scans (total of 17x2=34 slices) in order to cover enough craniocaudal length. These imaging parameters afforded 117 µm in-plane resolutions and a total scan time of 10 to 12 minutes per scan (20-25 minutes per animal) as the actual repetition time depends upon respiratory rate in a respiratory gated MR scan. The pancreas area was identified by locating the reference tissues such as kidneys, spleen, and liver through MRI imaging without fat saturation (**Fig. 60**). After the MR imaging session, the animals were carried on the positioning device and subjected to the PET scan.
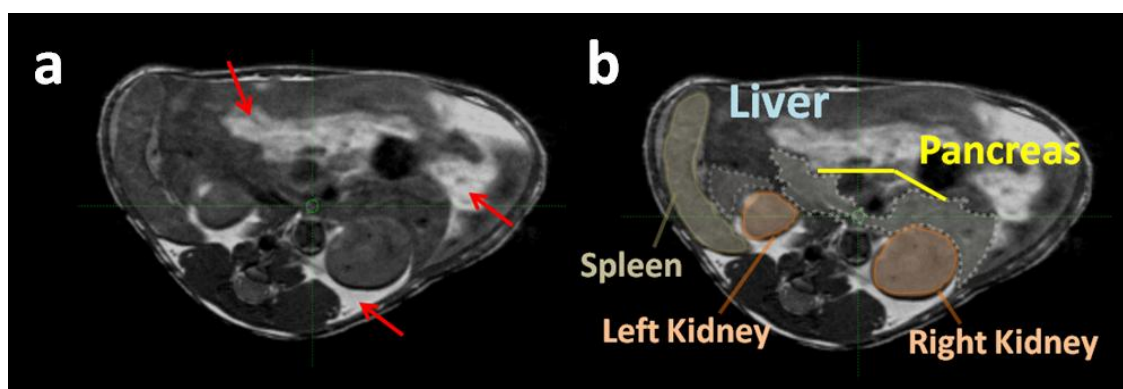

Figure 60. Typical axial MR images of mice pancreas without fat suppression obtained in the same slab (0.5 mm). (a) Red arrows indicate the fat content. (b) The edge of the pancreas was distinguished by the contrast of fat, liver, spleen, and kidneys.

A1.11 *Ex vivo* PET/CT imaging for flatten pancreas sample

Pancreas were removed intact with adjacent organs such as spleen, stomach, and duodenum and placed on a 2"x3" glass slide. The pancreas orientation was marked and the surrounding organs were removed. The pancreas was flattened by overlaying a cover slide under and applying weight for 10 min. The flatten pancreas with cover slide was placed at the center of field of view (FOV) in the PET/CT scanner. CT imaging was performed and followed by PET imaging. Imaging was reconstructed with OSEM2D. Data was analyzed using the Siemens Inveon Research Workplace (IRW 4.0) software. The region of interest (ROI) was manually drawn to encircle a whole pancreas based on the CT image. By selecting the whole pancreas ROI as the source, the segmentation of the whole uptake level (0-1.6 %ID/g) was performed. Data was analyzed by gating the PET intensity with 0.1 %ID/g interval.

A1.12 Imaging reproducibility

Thirteen mice were used to evaluate the reproducibility of the imaging method ($BaSO_4$-enhanced PET/CT imaging with ^{68}Ga-NOTA-EM2198). To each mouse, 100 μCi of ^{68}Ga-NOTA-EM2198 was i.v. injected. PET imaging was performed at 45 min p.i. with 15 min static scan. Three out of thirteen mice were used to perform test-re-test method (TR). For the TR method, the same mice were scanned twice within a 3 day interval.

A1.13 Histology

A1.13.1 Quantification of pancreatic islet by H/E stain

Experimental procedure is illustrated in **Figure 61.** Three mice were selected for histological studies before and after 6, 9, 15, 18, 35 days after STZ-treatment. Animals were anesthetized with inhaling 3% isoflurane. After the animal established a consistent breathing pattern, it was perfused with 10 mM of PBS (50 ml) followed by ice-cold 4% (w/v) paraformaldehyde in 0.1 M phosphate buffer (pH 7.4) (50 ml)(Sigma). Pancreas was collected and fixed in 4% formalin saline solution for 24 h before transferring into PBS for the embedding process. Tissue specimens were embedded in paraffin in a Hypercenter 3000 tissue preparation machine (Leica Meyer Instruments, Houston, TX). Embedded pancreas was sliced with 5 µm thick and prepared sequentially from three sections (front, middle, and the end) with 0.5 mm interval between the sections on a Leica RM 2165 microtome (Leica, Copenhagen, Denmark). Specimens were stained with hematoxylin and eosin (H/E) to visualize pancreatic islets. Histology samples preparation and H/E staining were performed by the Histology core lab at UT Southwestern Medical Center at Dallas. The islet counting of pancreas specimens were performed by visual counting using digital images of the slices which were obtained by an ArtixScan 4000H scanner (Microtec).
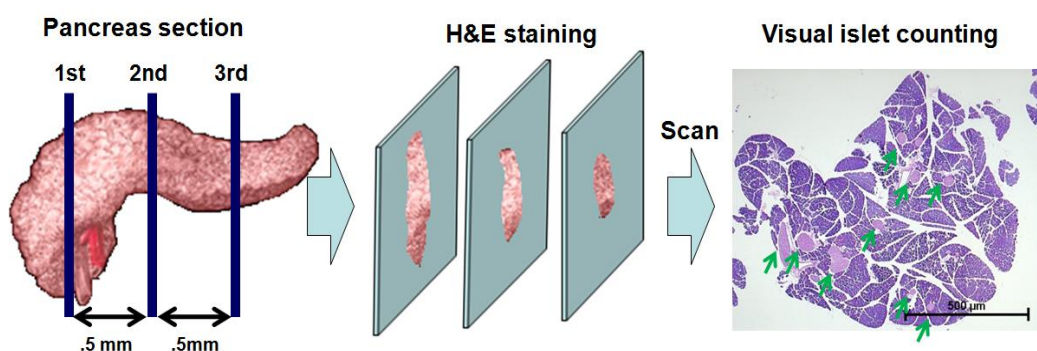
Figure 61. Procedure of histology sample preparation for islet number counting

A1.13.2 Quantification of islet number by H/E stain on an entire pancreas

Normal and STZ-induced diabetic mice were used for correlation the *ex vivo* PET imaging and histological examination of islet. Animals were i.v. injected (100 μCi) with ^{68}Ga-NOTA-EM2198. After 1 h p.i., animals were sacrificed and pancreas was collected. Excised pancreas was placed in between of two 2' x 3' cover slides and weight was applied to flatten the pancreas (**Fig. 62**). The flatten pancreas was subjected for PET/CT imaging. After PET/CT scan, the pancreas was fixed in 4% formalin saline solution for 24 h before transferring into PBS for the embedding process. Tissue specimens were embedded in a mega cassette and paraffin fixation was performed in a Hypercenter 3000 tissue preparation machine (Leica Meyer Instruments, Houston, TX). Embedded pancreas was sliced with 5 μm thick and prepared sequentially from seven slices on a Leica RM 2165 microtome (Leica, Copenhagen, Denmark). Specimens were stained with hematoxylin and eosin to visualize pancreatic islets. Histology samples preparation, H/E staining, imaging acquisition were performed by the Histology core lab at UT Southwestern Medical Center.
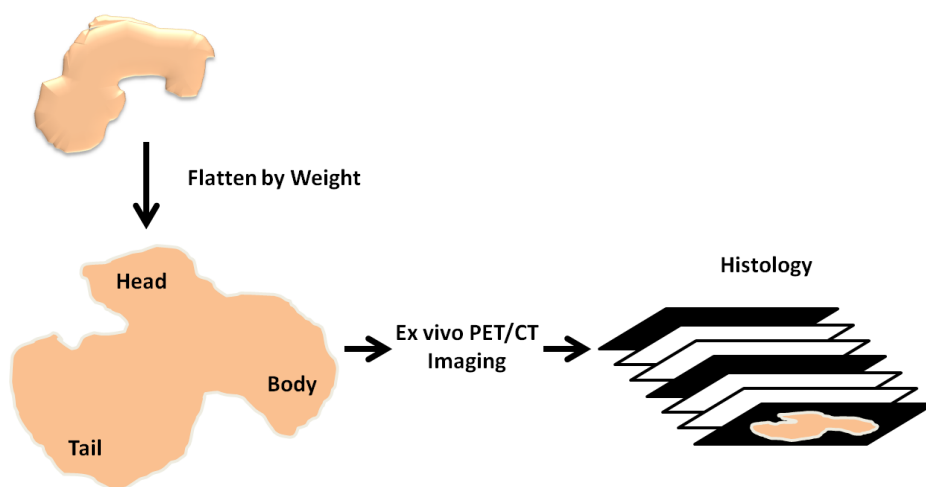
Figure 62. Procedure of sample preparation of flatten pancreas specimen for *ex vivo* PET/CT imaging and histology examination

A1.13.3 Immunohistochemistry and immunofluorescence staining

Pancreas from three mice was collected before and after 6, 9, 15, 18, and 35 days after STZ-treatment, they were fixed in paraformaldehyde in 0.1 M phosphate buffer (pH7.4) and sectioned into 3 levels at intervals of 0.5 mm and thickness of 5 μm. Sections were deparaffinized in EZ-DewaxTM (BioGenex) tissue deparaffinization solution. Antigen retrieval was performed with Tris-buffered saline (TBS)(100 mM Tris pH7.4, 138 mM NaCl, 27mM KCl) containing 1% SDS at R.T. for 5 min, followed by washing three-times with TBS. Sections were then blocked with TBS containing 10 % of donkey serum (Abcam) for 1 h. For immunohistochemistry (IHC) experiments, tissue sections were incubated at R.T. for 1 h with either polyclonal anti-GLP-1R from goat (1:5, sc-34637, Santa Cruz Biotechnology, Santa Cruz, CA), polyclonal anti-insulin from rabbit (1:200, ab63820, Abcam, Cambridge, MA), or monoclonal anti-glucagon from mouse (1: 1000, ab10988, Abcam) followed by washing 3-times with TBS. Specimens were then incubated either with Horse Radish Peroxidase (HRP)-conjugated donkey anti-goat (1:200, ab97120, Abcam), donkey anti-rabbit (1:50, ab7083, Abcam) or donkey anti-mouse (1:100, ab98799, Abcam) secondary antibodies. Immunohistochemical staining was performed by developing tissue with DAB (3,3'-diaminobenzidin) substrate (Abcam). For immunoflorescence staining, primary antibodies were used with same dilution ratio as IHC. Secondary antibodies such as DyLight-488 conjugated donkey polyclonal anti-goat (1:50, ab96935, Abcam), DyLight-594 conjugated donkey polyclonal anti-rabbit (1:50, ab96921, Abcam), and DyLight-649 conjugated donkey polyclonal anti-mouse (1:50, ab96878, Abcam) were used for to fluorescently image the primary antibodies. Control experiments were performed by incubation of specimens with normal goat, rabbit, or mouse serum. Immunohistochemistry (IHC) data was collected using a Nikon microscope and immunofluorescence (IF) was examined by a Nikon Eclipse Ti inverted

microscope with 200x magnification. All sections were mounted with Dapi-Fluoromount-G™ (SouthernBiotech). ImageJ was used for analyzing the positive areas of insulin, glucagon, and GLP-1R from IF data.

A1.14 Western blots for GLP-1 expression

Samples of cell lysates or pancreas homogenates was resolved by10% SDS-PAGE and transferred to a PVDF membrane. The membrane was probed with rabbit-anti-mouse anti-GLP-1R antibody (1:1000, Abcam) overnight at 4°C and detected using HRP-conjugated secondary antibodies (1:2000, Abcam) and visualized by enhanced DAB staining (Abcam).

A1.15. Pig imaging study

For the initial baseline scans, castrated male Ossabaw pigs were used for repeated PET/CT imaging. Two scans were performed within 8 days. For the first scan, 10.04 mCi (specific activity: 29.5 GBq/μmole) of dose was injected through the ear vein. For the second scan, 9.58 mCi (specific activity: 112.9 GBq/μmole) of dose was injected into the femoral vein. A femoral vein catheter was ultilized for blood draws during imaging. Imaging was performed using a Siemens Biograph TruePoint™ 64-slice PET/CT system (Siemens Medical Solutions, Knoxville, TN). Dynamic PET scanning was performed over the abdomen for 60 or 90 minutes immediately after dose injection. Blood was drawn prior to and intermittently during each scan for insulin analysis (Mercodia, Uppsala, Sweden), tracer activity, and blood glucose determination (Accu-Chek glucometer, Roche Diagnostics). The LIST mode PET imaging data was reconstructed into 42 and 51 frames of progressively increasing length. CT guided regions of interest (ROIs) were

generated for the pancreas, kidney, liver, muscle, and abdominal artery. To determine the inter-observer variation in measurements of pancreatic activity, 9 independent ROIs were generated and compared for consistency. The time activity curves (TAC) were generated using the Siemens Inveon Research Workplace (IRW) kinetic analysis toolbox. Kinetic modeling was performed using the Logan reference tissue model with muscle as the reference, and the blood input Logan model with an image derived input function.

A1.16. Statistical Analysis

Pearson correlation analysis was performed for the correlation study. Mann-Whitney test has been used for analyzing the differences between two groups. The Kruskal-Wallis test has been used to compare the means of three or more unmatched groups. In 95% confident level, P values less than 0.05 were considered statistically significant. All statistical analysis was performed on GraphPad Prism 5.0 Software (GraphPad, La Jolla, CA)

BIBLIOGRAPHY

1.   Zimmet, P. Globalization, coca-colonization and the chronic disease epidemic: can the Doomsday scenario be averted? *Journal of internal medicine* **247**, 301-310 (2000).

2.   Wild, S., Roglic, G., Green, A., Sicree, R. & King, H. Global prevalence of diabetes: estimates for the year 2000 and projections for 2030. *Diabetes care* **27**, 1047-1053 (2004).

3.   Ginter, E. & Simko, V. Global prevalence and future of diabetes mellitus. *Advances in experimental medicine and biology* **771**, 35-41 (2012).

4.   Amos, A.F., McCarty, D.J. & Zimmet, P. The rising global burden of diabetes and its complications: estimates and projections to the year 2010. *Diabetic medicine : a journal of the British Diabetic Association* **14 Suppl 5**, S1-85 (1997).

5.   Shaw, J.E., Sicree, R.A. & Zimmet, P.Z. Global estimates of the prevalence of diabetes for 2010 and 2030. *Diabetes research and clinical practice* **87**, 4-14 (2010).

6.   Garber, A.J. Clinical perspectives on type 2 diabetes in North America. *Diabetes/metabolism reviews* **11 Suppl 1**, S81-86 (1995).

7.   Sarwar, N. et al. Diabetes mellitus, fasting blood glucose concentration, and risk of vascular disease: a collaborative meta-analysis of 102 prospective studies. *Lancet* **375**, 2215-2222 (2010).

8.   Boussageon, R. et al. Effect of intensive glucose lowering treatment on all cause mortality, cardiovascular death, and microvascular events in type 2 diabetes: meta-analysis of randomised controlled trials. *BMJ* **343**, d4169 (2011).

9.   Zhang, P. et al. Global healthcare expenditure on diabetes for 2010 and 2030. *Diabetes research and clinical practice* **87**, 293-301 (2010).

10. Alberti, K.G. & Zimmet, P.Z. Definition, diagnosis and classification of diabetes mellitus and its complications. Part 1: diagnosis and classification of diabetes mellitus provisional report of a WHO consultation. *Diabetic medicine : a journal of the British Diabetic Association* **15**, 539-553 (1998).

11. Zimmet, P.Z. et al. Latent autoimmune diabetes mellitus in adults (LADA): the role of antibodies to glutamic acid decarboxylase in diagnosis and prediction of insulin dependency. *Diabetic medicine : a journal of the British Diabetic Association* **11**, 299-303 (1994).

12. Verge, C.F. et al. Prediction of type I diabetes in first-degree relatives using a combination of insulin, GAD, and ICA512bdc/IA-2 autoantibodies. *Diabetes* **45**, 926-933 (1996).

13. Humphrey, A.R. et al. Autoantibodies to glutamic acid decarboxylase and phenotypic features associated with early insulin treatment in individuals with adult-onset diabetes mellitus. *Diabetic medicine : a journal of the British Diabetic Association* **15**, 113-119 (1998).

14.   van Belle, T.L., Coppieters, K.T. & von Herrath, M.G. Type 1 diabetes: etiology, immunology, and therapeutic strategies. *Physiological reviews* **91**, 79-118 (2011).

15.   Valdes, A.M., Varney, M.D., Erlich, H.A. & Noble, J.A. Receiver Operating Characteristic Analysis of HLA, CTLA4, and Insulin Genotypes for Type 1 Diabetes. *Diabetes care* (2013).

16.   Black, M.H. et al. HLA-associated phenotypes in youth with autoimmune diabetes. *Pediatric diabetes* **14**, 121-128 (2013).

17.   Steck, A.K. et al. Association of the PTPN22/LYP gene with type 1 diabetes. *Pediatric diabetes* **7**, 274-278 (2006).

18.   Cosentino, A., Gambelunghe, G., Tortoioli, C. & Falorni, A. CTLA-4 gene polymorphism contributes to the genetic risk for latent autoimmune diabetes in adults. *Annals of the New York Academy of Sciences* **958**, 337-340 (2002).

19.   Jun, H.S. & Yoon, J.W. A new look at viruses in type 1 diabetes. *Diabetes/metabolism research and reviews* **19**, 8-31 (2003).

20.   Knip, M. et al. Environmental triggers and determinants of type 1 diabetes. *Diabetes* **54 Suppl 2**, S125-136 (2005).

21.   Riley, W.J. et al. A prospective study of the development of diabetes in relatives of patients with insulin-dependent diabetes. *The New England journal of medicine* **323**, 1167-1172 (1990).

22.   Kahn, C.R. Banting Lecture. Insulin action, diabetogenes, and the cause of type II diabetes. *Diabetes* **43**, 1066-1084 (1994).

23.   Barnett, A.H., Eff, C., Leslie, R.D. & Pyke, D.A. Diabetes in identical twins. A study of 200 pairs. *Diabetologia* **20**, 87-93 (1981).

24.   Rich, S.S. Mapping genes in diabetes. Genetic epidemiological perspective. *Diabetes* **39**, 1315-1319 (1990).

25.   Haffner, S.M., Stern, M.P., Mitchell, B.D., Hazuda, H.P. & Patterson, J.K. Incidence of type II diabetes in Mexican Americans predicted by fasting insulin and glucose levels, obesity, and body-fat distribution. *Diabetes* **39**, 283-288 (1990).

26.   Holliday, E.G. Hints of unique genetic effects for type 2 diabetes in India. *Diabetes* **62**, 1369-1370 (2013).

27.   Herder, C. & Roden, M. Genetics of type 2 diabetes: pathophysiologic and clinical relevance. *European journal of clinical investigation* **41**, 679-692 (2011).

28.   Chisholm, D.J., Campbell, L.V. & Kraegen, E.W. Pathogenesis of the insulin resistance syndrome (syndrome X). *Clinical and experimental pharmacology & physiology* **24**, 782-784 (1997).

29.   Metzger, B.E. 1990 overview of GDM. Accomplishments of the last decade--challenges for the future. *Diabetes* **40 Suppl 2**, 1-2 (1991).

30.   Gabbe, S.G. Management of diabetes mellitus in pregnancy. *American journal of obstetrics and gynecology* **153**, 824-828 (1985).

31.   Dabelea, D. et al. Increasing prevalence of gestational diabetes mellitus (GDM) over time and by birth cohort: Kaiser Permanente of Colorado GDM Screening Program. *Diabetes care* **28**, 579-584 (2005).

32. Kjos, S.L. et al. Gestational diabetes mellitus: the prevalence of glucose intolerance and diabetes mellitus in the first two months post partum. *American journal of obstetrics and gynecology* **163**, 93-98 (1990).

33. Kim, C., Newton, K.M. & Knopp, R.H. Gestational diabetes and the incidence of type 2 diabetes: a systematic review. *Diabetes care* **25**, 1862-1868 (2002).

34. Tisch, R. & McDevitt, H. Insulin-dependent diabetes mellitus. *Cell* **85**, 291-297 (1996).

35. von Herrath, M.G., Homann, D., Gairin, J.E. & Oldstone, M.B. Pathogenesis and treatment of virus-induced autoimmune diabetes: novel insights gained from the RIP-LCMV transgenic mouse model. *Biochem Soc Trans* **25**, 630-635 (1997).

36. Coppieters, K. & von Herrath, M. Taking a closer look at the pancreas. *Diabetologia* **51**, 2145-2147 (2008).

37. Classification and diagnosis of diabetes mellitus and other categories of glucose intolerance. National Diabetes Data Group. *Diabetes* **28**, 1039-1057 (1979).

38. Meier, J.J., Bhushan, A., Butler, A.E., Rizza, R.A. & Butler, P.C. Sustained beta cell apoptosis in patients with long-standing type 1 diabetes: indirect evidence for islet regeneration? *Diabetologia* **48**, 2221-2228 (2005).

39. Butler, A.E. et al. Beta-cell deficit and increased beta-cell apoptosis in humans with type 2 diabetes. *Diabetes* **52**, 102-110 (2003).

40. Meier, J.J. Beta cell mass in diabetes: a realistic therapeutic target? *Diabetologia* **51**, 703-713 (2008).

41. Souza, F. et al. Current progress in non-invasive imaging of beta cell mass of the endocrine pancreas. *Current medicinal chemistry* **13**, 2761-2773 (2006).

42. Kjems, L.L. et al. Decrease in beta-cell mass leads to impaired pulsatile insulin secretion, reduced postprandial hepatic insulin clearance, and relative hyperglucagonemia in the minipig. *Diabetes* **50**, 2001-2012 (2001).

43. Matveyenko, A.V. & Butler, P.C. Relationship between beta-cell mass and diabetes onset. *Diabetes, obesity & metabolism* **10 Suppl 4**, 23-31 (2008).

44. Ritzel, R.A., Butler, A.E., Rizza, R.A., Veldhuis, J.D. & Butler, P.C. Relationship between beta-cell mass and fasting blood glucose concentration in humans. *Diabetes care* **29**, 717-718 (2006).

45. Kim, M.S. & Polychronakos, C. Immunogenetics of type 1 diabetes. *Hormone research* **64**, 180-188 (2005).

46. Mandrup-Poulsen, T. et al. Lack of predictive value of islet cell antibodies, insulin antibodies, and HLA-DR phenotype for remission in cyclosporin-treated IDDM patients. The Canadian-European Randomized Control Trial Group. *Diabetes* **39**, 204-210 (1990).

47. Sweet, I.R., Cook, D.L., Lernmark, A., Greenbaum, C.J. & Krohn, K.A. Non-invasive imaging of beta cell mass: a quantitative analysis. *Diabetes technology & therapeutics* **6**, 652-659 (2004).

48. Normandin, M.D. et al. In vivo imaging of endogenous pancreatic beta-cell mass in healthy and type 1 diabetic subjects using 18F-fluoropropyl-

dihydrotetrabenazine and PET. *Journal of nuclear medicine : official publication, Society of Nuclear Medicine* **53**, 908-916 (2012).

49. Saudek, F., Brogren, C.H. & Manohar, S. Imaging the Beta-cell mass: why and how. *The review of diabetic studies : RDS* **5**, 6-12 (2008).

50. Lu, Y. et al. Noninvasive imaging of islet grafts using positron-emission tomography. *Proceedings of the National Academy of Sciences of the United States of America* **103**, 11294-11299 (2006).

51. Lu, Y. et al. Long-term monitoring of transplanted islets using positron emission tomography. *Molecular therapy : the journal of the American Society of Gene Therapy* **14**, 851-856 (2006).

52. Massoud, T.F. & Gambhir, S.S. Molecular imaging in living subjects: seeing fundamental biological processes in a new light. *Genes & development* **17**, 545-580 (2003).

53. Weissleder, R. & Pittet, M.J. Imaging in the era of molecular oncology. *Nature* **452**, 580-589 (2008).

54. Lide, D.R. Handbook of Chemistry and Physic. (CRC Press, 2005).

55. Okudan, B. & Smitherman, T.C. The value and throughput of rest Thallium-201/stress Technetium -99m sestamibi dual-isotope myocardial SPECT. *Anadolu kardiyoloji dergisi : AKD = the Anatolian journal of cardiology* **4**, 161-168 (2004).

56. Berman, D.S. et al. Dual-isotope myocardial perfusion SPECT with rest thallium-201 and stress Tc-99m sestamibi. *Cardiology clinics* **12**, 261-270 (1994).

57. James, M.L. & Gambhir, S.S. A molecular imaging primer: modalities, imaging agents, and applications. *Physiological reviews* **92**, 897-965 (2012).

58. Luboldt, W., Weber, R., Seemann, M., Desantis, M. & Reiser, M. Influence of helical CT parameters on spatial resolution in CT angiography performed with a subsecond scanner. *Invest Radiol* **34**, 421-426 (1999).

59. Contag, C.H. et al. Photonic detection of bacterial pathogens in living hosts. *Molecular microbiology* **18**, 593-603 (1995).

60. Bosco, D. et al. Unique arrangement of alpha- and beta-cells in human islets of Langerhans. *Diabetes* **59**, 1202-1210 (2010).

61. Cabrera, O. et al. The unique cytoarchitecture of human pancreatic islets has implications for islet cell function. *Proceedings of the National Academy of Sciences of the United States of America* **103**, 2334-2339 (2006).

62. Brissova, M. et al. Assessment of human pancreatic islet architecture and composition by laser scanning confocal microscopy. *The journal of histochemistry and cytochemistry : official journal of the Histochemistry Society* **53**, 1087-1097 (2005).

63. Steiner, D.J., Kim, A., Miller, K. & Hara, M. Pancreatic islet plasticity: interspecies comparison of islet architecture and composition. *Islets* **2**, 135-145 (2010).

64. Goke, B. What are the potential benefits of clinical beta-cell imaging in diabetes mellitus? *Current pharmaceutical design* **16**, 1547-1549 (2010).

65. Andralojc, K. et al. Obstacles on the way to the clinical visualisation of beta cells: looking for the Aeneas of molecular imaging to navigate between Scylla and Charybdis. *Diabetologia* **55**, 1247-1257 (2012).

66. Kessler, R.M., Ellis, J.R., Jr. & Eden, M. Analysis of emission tomographic scan data: limitations imposed by resolution and background. *Journal of computer assisted tomography* **8**, 514-522 (1984).

67. Woods, M., Zhang, S. & Sherry, A.D. Toward the Design of MR Agents for Imaging beta-Cell Function. *Current medicinal chemistry. Immunology, endocrine & metabolic agents* **4**, 349-369 (2004).

68. Jung, M.J. et al. MRI of transplanted surface-labeled pancreatic islets with heparinized superparamagnetic iron oxide nanoparticles. *Biomaterials* **32**, 9391-9400 (2011).

69. Lee, N. et al. Magnetosome-like ferrimagnetic iron oxide nanocubes for highly sensitive MRI of single cells and transplanted pancreatic islets. *Proceedings of the National Academy of Sciences of the United States of America* **108**, 2662-2667 (2011).

70. Marzola, P. et al. In vivo visualization of transplanted pancreatic islets by MRI: comparison between in vivo, histological and electron microscopy findings. *Contrast media & molecular imaging* **4**, 135-142 (2009).

71. Jirak, D. et al. MRI of transplanted pancreatic islets. *Magnetic resonance in medicine : official journal of the Society of Magnetic Resonance in Medicine / Society of Magnetic Resonance in Medicine* **52**, 1228-1233 (2004).

72. Dodson, G. & Steiner, D. The role of assembly in insulin's biosynthesis. *Current opinion in structural biology* **8**, 189-194 (1998).

73. Satin, L.S. Localized calcium influx in pancreatic beta-cells: its significance for Ca2+-dependent insulin secretion from the islets of Langerhans. *Endocrine* **13**, 251-262 (2000).

74. Lubag, A.J., De Leon-Rodriguez, L.M., Burgess, S.C. & Sherry, A.D. Noninvasive MRI of beta-cell function using a Zn2+-responsive contrast agent. *Proceedings of the National Academy of Sciences of the United States of America* **108**, 18400-18405 (2011).

75. Gimi, B. et al. Functional MR microimaging of pancreatic beta-cell activation. *Cell transplantation* **15**, 195-203 (2006).

76. Singhal, T. et al. Pancreatic Beta Cell Mass PET Imaging and Quantification with [(11)C]DTBZ and [(18)F]FP-(+)-DTBZ in Rodent Models of Diabetes. *Mol Imaging Biol* (2010).

77. Singhal, T. et al. Pancreatic beta cell mass PET imaging and quantification with [11C]DTBZ and [18F]FP-(+)-DTBZ in rodent models of diabetes. *Molecular imaging and biology : MIB : the official publication of the Academy of Molecular Imaging* **13**, 973-984 (2011).

78. Fagerholm, V. et al. Assessment of islet specificity of dihydrotetrabenazine radiotracer binding in rat pancreas and human pancreas. *Journal of nuclear*

medicine : official publication, Society of Nuclear Medicine **51**, 1439-1446 (2010).

79. Wu, Z. & Kandeel, F. Radionuclide probes for molecular imaging of pancreatic beta-cells. *Advanced drug delivery reviews* **62**, 1125-1138 (2010).

80. Young, A.A. et al. Evidence for release of free glucose from muscle during amylin-induced glycogenolysis in rats. *FEBS letters* **334**, 317-321 (1993).

81. Malaisse, W.J., Damhaut, P., Ladriere, L. & Goldman, S. Fate of 2-deoxy-2-[18F]fluoro-D-glucose in hyperglycemic rats. *International journal of molecular medicine* **6**, 549-552 (2000).

82. Malaisse, W.J. On the track to the beta-cell. *Diabetologia* **44**, 393-406 (2001).

83. Sener, A. et al. Uptake of 1-deoxy-1-[125I]iodo-D-mannoheptulose by different cell types: in vitro and in vivo experiments. *International journal of molecular medicine* **7**, 495-500 (2001).

84. Campbell, J.D., Sansom, M.S. & Ashcroft, F.M. Potassium channel regulation. *EMBO reports* **4**, 1038-1042 (2003).

85. Minami, K., Miki, T., Kadowaki, T. & Seino, S. Roles of ATP-sensitive K+ channels as metabolic sensors: studies of Kir6.x null mice. *Diabetes* **53 Suppl 3**, S176-180 (2004).

86. Ashcroft, F.M. & Rorsman, P. Electrophysiology of the pancreatic beta-cell. *Progress in biophysics and molecular biology* **54**, 87-143 (1989).

87. Meyer, M., Chudziak, F., Schwanstecher, C., Schwanstecher, M. & Panten, U. Structural requirements of sulphonylureas and analogues for interaction with sulphonylurea receptor subtypes. *British journal of pharmacology* **128**, 27-34 (1999).

88. Giannaccini, G. et al. Characterization of sulfonylurea receptors in isolated human pancreatic islets. *Journal of cellular biochemistry* **71**, 182-188 (1998).

89. Gaines, K.L., Hamilton, S. & Boyd, A.E., 3rd Characterization of the sulfonylurea receptor on beta cell membranes. *The Journal of biological chemistry* **263**, 2589-2592 (1988).

90. Schmitz, A. et al. Synthesis and evaluation of fluorine-18 labeled glyburide analogs as beta-cell imaging agents. *Nuclear medicine and biology* **31**, 483-491 (2004).

91. Suzuki, M. et al. Immuno-localization of sulphonylurea receptor 1 in rat pancreas. *Diabetologia* **42**, 1204-1211 (1999).

92. Chutkow, W.A., Simon, M.C., Le Beau, M.M. & Burant, C.F. Cloning, tissue expression, and chromosomal localization of SUR2, the putative drug-binding subunit of cardiac, skeletal muscle, and vascular KATP channels. *Diabetes* **45**, 1439-1445 (1996).

93. Wangler, B. et al. Synthesis and evaluation of (S)-2-(2-[18F]fluoroethoxy)-4-([3-methyl-1-(2-piperidin-1-yl-phenyl)-butyl-carbam   oyl]-methyl)-benzoic   acid ([18F]repaglinide): a promising radioligand for quantification of pancreatic beta-cell mass with positron emission tomography (PET). *Nucl Med Biol* **31**, 639-647 (2004).

94. Konidaris, C., Simonson, W., Michelsen, B. & Papadopoulos, G.K. Specific monoclonal antibodies against the surface of rat islet beta cells. *Cell biology international* **26**, 817-828 (2002).

95. Moore, A., Bonner-Weir, S. & Weissleder, R. Noninvasive in vivo measurement of beta-cell mass in mouse model of diabetes. *Diabetes* **50**, 2231-2236 (2001).

96. Hampe, C.S., Wallen, A.R., Schlosser, M., Ziegler, M. & Sweet, I.R. Quantitative evaluation of a monoclonal antibody and its fragment as potential markers for pancreatic beta cell mass. *Experimental and clinical endocrinology & diabetes : official journal, German Society of Endocrinology [and] German Diabetes Association* **113**, 381-387 (2005).

97. Atouf, F., Czernichow, P. & Scharfmann, R. Expression of neuronal traits in pancreatic beta cells. Implication of neuron-restrictive silencing factor/repressor element silencing transcription factor, a neuron-restrictive silencer. *The Journal of biological chemistry* **272**, 1929-1934 (1997).

98. Watanabe, T. & Nagatsu, I. Immunohistochemical colocalization of insulin, aromatic L-amino acid decarboxylase and dopamine beta-hydroxylase in islet B cells of chicken pancreas. *Cell and tissue research* **263**, 131-136 (1991).

99. Gonoi, T. et al. Functional neuronal ionotropic glutamate receptors are expressed in the non-neuronal cell line MIN6. *The Journal of biological chemistry* **269**, 16989-16992 (1994).

100. Baekkeskov, S. et al. Identification of the 64K autoantigen in insulin-dependent diabetes as the GABA-synthesizing enzyme glutamic acid decarboxylase. *Nature* **347**, 151-156 (1990).

101. Teitelman, G. & Lee, J.K. Cell lineage analysis of pancreatic islet development: glucagon and insulin cells arise from catecholaminergic precursors present in the pancreatic duct. *Developmental biology* **121**, 454-466 (1987).

102. Philipson, L.H., Kusnetsov, A., Larson, T., Zeng, Y. & Westermark, G. Human, rodent, and canine pancreatic beta-cells express a sodium channel alpha 1-subunit related to a fetal brain isoform. *Diabetes* **42**, 1372-1377 (1993).

103. Teitelman, G. Insulin cells of pancreas extend neurites but do not arise from the neuroectoderm. *Developmental biology* **142**, 368-379 (1990).

104. Polak, M. et al. Nerve growth factor induces neuron-like differentiation of an insulin-secreting pancreatic beta cell line. *Proceedings of the National Academy of Sciences of the United States of America* **90**, 5781-5785 (1993).

105. Martino, E., Seo, H., Lernmark, A. & Refetoff, S. Ontogenetic patterns of thyrotropin-releasing hormone-like material in rat hypothalamus, pancreas, and retina: selective effect of light deprivation. *Proceedings of the National Academy of Sciences of the United States of America* **77**, 4345-4348 (1980).

106. Rubi, B. et al. Dopamine D2-like receptors are expressed in pancreatic beta cells and mediate inhibition of insulin secretion. *The Journal of biological chemistry* **280**, 36824-36832 (2005).

107. Schafer, M.K. et al. Species-specific vesicular monoamine transporter 2 (VMAT2) expression in mammalian pancreatic beta cells: implications for

optimising radioligand-based human beta cell mass (BCM) imaging in animal models. *Diabetologia* **56**, 1047-1056 (2013).

108. Saisho, Y. et al. Relationship between pancreatic vesicular monoamine transporter 2 (VMAT2) and insulin expression in human pancreas. *Journal of molecular histology* **39**, 543-551 (2008).

109. Anlauf, M. et al. Expression of the two isoforms of the vesicular monoamine transporter (VMAT1 and VMAT2) in the endocrine pancreas and pancreatic endocrine tumors. *The journal of histochemistry and cytochemistry : official journal of the Histochemistry Society* **51**, 1027-1040 (2003).

110. Gilon, P. & Henquin, J.C. Mechanisms and physiological significance of the cholinergic control of pancreatic beta-cell function. *Endocrine reviews* **22**, 565-604 (2001).

111. Bernal-Mizrachi, E., Cras-Meneur, C., Ohsugi, M. & Permutt, M.A. Gene expression profiling in islet biology and diabetes research. *Diabetes/metabolism research and reviews* **19**, 32-42 (2003).

112. Borelli, M.I., Villar, M.J., Orezzoli, A. & Gagliardino, J.J. Presence of DOPA decarboxylase and its localisation in adult rat pancreatic islet cells. *Diabetes & metabolism* **23**, 161-163 (1997).

113. Ericson, L.E., Hakanson, R. & Lundquist, I. Accumulation of dopamine in mouse pancreatic B-cells following injection of L-DOPA. Localization to secretory granules and inhibition of insulin secretion. *Diabetologia* **13**, 117-124 (1977).

114. Ismail, D. & Hussain, K. Role of 18F-DOPA PET/CT imaging in congenital hyperinsulinism. *Reviews in endocrine & metabolic disorders* **11**, 165-169 (2010).

115. Garcia, A. et al. 18F-Fallypride PET of pancreatic islets: in vitro and in vivo rodent studies. *Journal of nuclear medicine : official publication, Society of Nuclear Medicine* **52**, 1125-1132 (2011).

116. Rodriguez-Diaz, R. et al. Alpha cells secrete acetylcholine as a non-neuronal paracrine signal priming beta cell function in humans. *Nature medicine* **17**, 888-892 (2011).

117. Clark, P.B. et al. Neurofunctional imaging of the pancreas utilizing the cholinergic PET radioligand [18F]4-fluorobenzyltrozamicol. *European journal of nuclear medicine and molecular imaging* **31**, 258-260 (2004).

118. Koeppe, R.A. et al. 11C-DTBZ and 18F-FDG PET measures in differentiating dementias. *Journal of nuclear medicine : official publication, Society of Nuclear Medicine* **46**, 936-944 (2005).

119. Kumar, A. et al. [11C]DTBZ-PET correlates of levodopa responses in asymmetric Parkinson's disease. *Brain : a journal of neurology* **126**, 2648-2655 (2003).

120. Chan, G.L. et al. Reproducibility studies with 11C-DTBZ, a monoamine vesicular transporter inhibitor in healthy human subjects. *Journal of nuclear medicine : official publication, Society of Nuclear Medicine* **40**, 283-289 (1999).

121. Goland, R. et al. 11C-dihydrotetrabenazine PET of the pancreas in subjects with long-standing type 1 diabetes and in healthy controls. *Journal of nuclear medicine : official publication, Society of Nuclear Medicine* **50**, 382-389 (2009).

122. Simpson, N.R. et al. Visualizing pancreatic beta-cell mass with [11C]DTBZ. *Nucl Med Biol* **33**, 855-864 (2006).
123. Kung, M.P. et al. In vivo imaging of beta-cell mass in rats using 18F-FP-(+)-DTBZ: a potential PET ligand for studying diabetes mellitus. *Journal of nuclear medicine : official publication, Society of Nuclear Medicine* **49**, 1171-1176 (2008).
124. Tsao, H.H. et al. Binding characteristics of 9-fluoropropyl-(+)-dihydrotetrabenzazine (AV-133) to the vesicular monoamine transporter type 2 in rats. *Nuclear medicine and biology* **37**, 413-419.
125. Souza, F. et al. Longitudinal noninvasive PET-based beta cell mass estimates in a spontaneous diabetes rat model. *The Journal of clinical investigation* **116**, 1506-1513 (2006).
126. Rahier, J. et al. The pancreatic polypeptide cells in the human pancreas: the effects of age and diabetes. *J Clin Endocrinol Metab* **56**, 441-444 (1983).
127. Eriksson, O. et al. In vivo and in vitro characterization of [18F]-FE-(+)-DTBZ as a tracer for beta-cell mass. *Nucl Med Biol* **37**, 357-363 (2010).
128. Virostko, J. et al. Multimodal image coregistration and inducible selective cell ablation to evaluate imaging ligands. *Proceedings of the National Academy of Sciences of the United States of America* **108**, 20719-20724 (2011).
129. Erickson, J.D., Schafer, M.K., Bonner, T.I., Eiden, L.E. & Weihe, E. Distinct pharmacological properties and distribution in neurons and endocrine cells of two isoforms of the human vesicular monoamine transporter. *Proceedings of the National Academy of Sciences of the United States of America* **93**, 5166-5171 (1996).
130. Xu, G. et al. Downregulation of GLP-1 and GIP receptor expression by hyperglycemia: possible contribution to impaired incretin effects in diabetes. *Diabetes* **56**, 1551-1558 (2007).
131. Kieffer, T.J., McIntosh, C.H. & Pederson, R.A. Degradation of glucose-dependent insulinotropic polypeptide and truncated glucagon-like peptide 1 in vitro and in vivo by dipeptidyl peptidase IV. *Endocrinology* **136**, 3585-3596 (1995).
132. Edwards, C.M. et al. Exendin-4 reduces fasting and postprandial glucose and decreases energy intake in healthy volunteers. *American journal of physiology. Endocrinology and metabolism* **281**, E155-161 (2001).
133. Wucherpfennig, K.W. & Eisenbarth, G.S. Type 1 diabetes. *Nat Immunol* **2**, 767-768 (2001).
134. Wu, Z. et al. In Vivo Imaging of Transplanted Islets with (64)Cu-DO3A-VS-Cys(40)-Exendin-4 by Targeting GLP-1 Receptor. *Bioconjug Chem* (2011).
135. Wild, D. et al. Exendin-4-based radiopharmaceuticals for glucagonlike peptide-1 receptor PET/CT and SPECT/CT. *Journal of nuclear medicine : official publication, Society of Nuclear Medicine* **51**, 1059-1067 (2010).
136. Gotthardt, M. et al. Use of the incretin hormone glucagon-like peptide-1 (GLP-1) for the detection of insulinomas: initial experimental results. *European journal of nuclear medicine and molecular imaging* **29**, 597-606 (2002).

137. Gotthardt, M. et al. A new technique for in vivo imaging of specific GLP-1 binding sites: first results in small rodents. *Regulatory peptides* **137**, 162-167 (2006).

138. Wang, Y. et al. Synthesis and evaluation of [18F]exendin (9-39) as a potential biomarker to measure pancreatic beta-cell mass. *Nucl Med Biol* **39**, 167-176 (2012).

139. Tornehave, D., Kristensen, P., Romer, J., Knudsen, L.B. & Heller, R.S. Expression of the GLP-1 receptor in mouse, rat, and human pancreas. *The journal of histochemistry and cytochemistry : official journal of the Histochemistry Society* **56**, 841-851 (2008).

140. Chopra, A. in Molecular Imaging and Contrast Agent Database (MICAD)Bethesda (MD); 2004).

141. Leung, K. in Molecular Imaging and Contrast Agent Database (MICAD)Bethesda (MD); 2004).

142. Leung, K. in Molecular Imaging and Contrast Agent Database (MICAD)Bethesda (MD); 2004).

143. Pach, D. et al. Glucagon-Like Peptide-1 Receptor Imaging with [Lys (40) (Ahx-HYNIC- (99 m) Tc/EDDA)NH 2]-Exendin-4 for the Diagnosis of Recurrence or Dissemination of Medullary Thyroid Cancer: A Preliminary Report. *International journal of endocrinology* **2013**, 384508 (2013).

144. Sowa-Staszczak, A. et al. Glucagon-like peptide-1 receptor imaging with [Lys40(Ahx-HYNIC- 99mTc/EDDA)NH2]-exendin-4 for the detection of insulinoma. *European journal of nuclear medicine and molecular imaging* **40**, 524-531 (2013).

145. Reubi, J.C., Lamberts, S.J. & Krenning, E.P. Receptor imaging of human diseases using radiolabeled peptides. *Journal of receptor and signal transduction research* **15**, 379-392 (1995).

146. Dijkgraaf, I., Boerman, O.C., Oyen, W.J., Corstens, F.H. & Gotthardt, M. Development and application of peptide-based radiopharmaceuticals. *Anti-cancer agents in medicinal chemistry* **7**, 543-551 (2007).

147. Okarvi, S.M. Peptide-based radiopharmaceuticals: future tools for diagnostic imaging of cancers and other diseases. *Medicinal research reviews* **24**, 357-397 (2004).

148. Reubi, J.C. Peptide receptors as molecular targets for cancer diagnosis and therapy. *Endocrine reviews* **24**, 389-427 (2003).

149. Vaidyanathan, G. & Zalutsky, M.R. Synthesis of N-succinimidyl 4-[18F]fluorobenzoate, an agent for labeling proteins and peptides with 18F. *Nature protocols* **1**, 1655-1661 (2006).

150. Schottelius, M. et al. First (18)F-labeled tracer suitable for routine clinical imaging of sst receptor-expressing tumors using positron emission tomography. *Clinical cancer research : an official journal of the American Association for Cancer Research* **10**, 3593-3606 (2004).

151. Gao, H. et al. PET of insulinoma using (1)(8)F-FBEM-EM3106B, a new GLP-1 analogue. *Molecular pharmaceutics* **8**, 1775-1782 (2011).

152. Glaser, M. & Arstad, E. "Click labeling" with 2-[18f]fluoroethylazide for positron emission tomography. *Bioconjugate chemistry* **18**, 989-993 (2007).

153. Ting, R., Adam, M.J., Ruth, T.J. & Perrin, D.M. Arylfluoroborates and alkylfluorosilicates as potential PET imaging agents: high-yielding aqueous biomolecular 18F-labeling. *Journal of the American Chemical Society* **127**, 13094-13095 (2005).

154. Ting, R. et al. Toward [18F]-labeled aryltrifluoroborate radiotracers: in vivo positron emission tomography imaging of stable aryltrifluoroborate clearance in mice. *Journal of the American Chemical Society* **130**, 12045-12055 (2008).

155. D'Souza, C.A., McBride, W.J., Sharkey, R.M., Todaro, L.J. & Goldenberg, D.M. High-yielding aqueous 18F-labeling of peptides via Al18F chelation. *Bioconjugate chemistry* **22**, 1793-1803 (2011).

156. McBride, W.J. et al. A novel method of 18F radiolabeling for PET. *Journal of nuclear medicine : official publication, Society of Nuclear Medicine* **50**, 991-998 (2009).

157. Molek, P., Strukelj, B. & Bratkovic, T. Peptide phage display as a tool for drug discovery: targeting membrane receptors. *Molecules* **16**, 857-887 (2011).

158. Nock, B. et al. [99mTc]Demobesin 1, a novel potent bombesin analogue for GRP receptor-targeted tumour imaging. *European journal of nuclear medicine and molecular imaging* **30**, 247-258 (2003).

159. Nock, B.A. et al. Potent bombesin-like peptides for GRP-receptor targeting of tumors with 99mTc: a preclinical study. *Journal of medicinal chemistry* **48**, 100-110 (2005).

160. Abiraj, K. et al. Tetraamine-derived bifunctional chelators for technetium-99m labelling: synthesis, bioconjugation and evaluation as targeted SPECT imaging probes for GRP-receptor-positive tumours. *Chemistry* **16**, 2115-2124 (2010).

161. Niu, N., Mao, X., Jing, H. & Li, F. Parathyroid hyperplasia shown on (99m)Tc-HYNIC-TOC scan. *Clin Nucl Med* **38**, 294-296 (2013).

162. Kabachnik, M.I. et al. SYNTHESIS AND STUDY OF A NEW COMPLEXONE - N,N',N''-TRIS-(DIHYDROXYPHOSPHORYLMETHYL)-1,4,7-TRIAZACYCLONONANE. *Bulletin of the Academy of Sciences of the Ussr Division of Chemical Science* **33**, 769-777 (1984).

163. Hanaoka, H. et al. Evaluation of Cu-64-labeled DOTA-d-Phe(1)-Tyr(3)-octreotide (Cu-64-DOTA-TOC) for imaging somatostatin receptor-expressing tumors. *Annals of Nuclear Medicine* **23**, 559-567 (2009).

164. Chen, K. et al. Evaluation of Cu-64 Labeled GX1: A Phage Display Peptide Probe for PET Imaging of Tumor Vasculature. *Molecular Imaging and Biology* **14**, 96-105 (2012).

165. Boswell, C.A. et al. Comparative in vivo stability of copper-64-labeled cross-bridged and conventional tetraazamacrocyclic complexes. *Journal of medicinal chemistry* **47**, 1465-1474 (2004).

166. Wadas, T.J., Wong, E.H., Weisman, G.R. & Anderson, C.J. Coordinating radiometals of copper, gallium, indium, yttrium, and zirconium for PET and SPECT imaging of disease. *Chem Rev* **110**, 2858-2902 (2010).

167. Hausner, S.H. et al. Evaluation of [64Cu]Cu-DOTA and [64Cu]Cu-CB-TE2A chelates for targeted positron emission tomography with an alphavbeta6-specific peptide. *Mol Imaging* **8**, 111-121 (2009).

168. Wadas, T.J. & Anderson, C.J. Radiolabeling of TETA- and CB-TE2A-conjugated peptides with copper-64. *Nature protocols* **1**, 3062-3068 (2006).

169. Sun, Y. et al. Indium (III) and gallium (III) complexes of bis(aminoethanethiol) ligands with different denticities: stabilities, molecular modeling, and in vivo behavior. *Journal of medicinal chemistry* **39**, 458-470 (1996).

170. Clarke, E.T. & Martell, A.E. STABILITIES OF THE FE(III), GA(III) AND IN(III) CHELATES OF N,N',N"-TRIAZACYCLONONANETRIACETIC ACID. *Inorg. Chim. Acta* **181**, 273-280 (1991).

171. Like, A.A. & Rossini, A.A. Streptozotocin-induced pancreatic insulitis: new model of diabetes mellitus. *Science* **193**, 415-417 (1976).

172. Szkudelski, T. The mechanism of alloxan and streptozotocin action in B cells of the rat pancreas. *Physiol. Res.* **50**, 537-546 (2001).

173. Rabinovitch, A. An update on cytokines in the pathogenesis of insulin-dependent diabetes mellitus. *Diabetes-Metabolism Reviews* **14**, 129-151 (1998).

174. Rabinovitch, A. & Suarez-Pinzon, W.L. Cytokines and their roles in pancreatic islet beta-cell destruction and insulin-dependent diabetes mellitus. *Biochemical pharmacology* **55**, 1139-1149 (1998).

175. West, I.C. Radicals and oxidative stress in diabetes. *Diabetic Medicine* **17**, 171-180 (2000).

176. Liu, K. et al. Streptozotocin, an O-GlcNAcase inhibitor, blunts insulin and growth hormone secretion. *Molecular and cellular endocrinology* **194**, 135-146 (2002).

177. Delaney, C.A. et al. Comparison of inhibition of glucose-stimulated insulin secretion in rat islets of Langerhans by streptozotocin and methyl and ethyl nitrosoureas and methanesulphonates. Lack of correlation with nitric oxide-releasing or O6-alkylating ability. *Biochemical pharmacology* **50**, 2015-2020 (1995).

178. Elsner, M., Guldbakke, B., Tiedge, M., Munday, R. & Lenzen, S. Relative importance of transport and alkylation for pancreatic beta-cell toxicity of streptozotocin. *Diabetologia* **43**, 1528-1533 (2000).

179. Sandler, S. & Swenne, I. Streptozotocin, but not alloxan, induces DNA repair synthesis in mouse pancreatic islets in vitro. *Diabetologia* **25**, 444-447 (1983).

180. Heller, B. et al. Analysis of oxygen radical toxicity in pancreatic islets at the single cell level. *Biological chemistry Hoppe-Seyler* **375**, 597-602 (1994).

181. Nukatsuka, M., Yoshimura, Y., Nishida, M. & Kawada, J. Allopurinol protects pancreatic beta cells from the cytotoxic effect of streptozotocin: in vitro study. *Journal of pharmacobio-dynamics* **13**, 259-262 (1990).

182. Chang, K.C. et al. Possible superoxide radical-induced alteration of vascular reactivity in aortas from streptozotocin-treated rats. *The Journal of pharmacology and experimental therapeutics* **266**, 992-1000 (1993).

183. Loven, D.P. et al. Superoxide dismutase activity in the intestine of the streptozotocin-diabetic rat. *Endocrinology* **111**, 737-742 (1982).

184. Maritim, A.C., Sanders, R.A. & Watkins, J.B. Diabetes, oxidative stress, and antioxidants: A review. *Journal of biochemical and molecular toxicology* **17**, 24-38 (2003).

185. Drucker, D.J. Enhancing incretin action for the treatment of type 2 diabetes. *Diabetes care* **26**, 2929-2940 (2003).

186. Seino, Y. Understanding the incretin effect. *The Journal of clinical endocrinology and metabolism* **96**, 934-935 (2011).

187. Nauck, M., Stockmann, F., Ebert, R. & Creutzfeldt, W. Reduced incretin effect in type 2 (non-insulin-dependent) diabetes. *Diabetologia* **29**, 46-52 (1986).

188. Mentlein, R., Gallwitz, B. & Schmidt, W.E. Dipeptidylpeptidase-Iv Hydrolyzes Gastric-Inhibitory Polypeptide, Glucagon-Like Peptide-1(7-36)Amide, Peptide Histidine Methionine and Is Responsible for Their Degradation in Human Serum. *Eur. J. Biochem.* **214**, 829-835 (1993).

189. Deacon, C.F., Carr, R.D. & Holst, J.J. DPP-4 inhibitor therapy: new directions in the treatment of type 2 diabetes. *Front. Biosci.* **13**, 1780-1794 (2008).

190. Hupe-Sodmann, K. et al. Characterisation of the processing by human neutral endopeptidase 24.11 of GLP-1(7-36) amide and comparison of the substrate specificity of the enzyme for other glucagon-like peptides. *Regul Pept* **58**, 149-156 (1995).

191. Mentlein, R., Gallwitz, B. & Schmidt, W.E. Dipeptidyl-peptidase IV hydrolyses gastric inhibitory polypeptide, glucagon-like peptide-1(7-36)amide, peptide histidine methionine and is responsible for their degradation in human serum. *European journal of biochemistry / FEBS* **214**, 829-835 (1993).

192. Thum, A. et al. Endoproteolysis by isolated membrane peptidases reveal metabolic stability of glucagon-like peptide-1 analogs, exendins-3 and -4. *Exp Clin Endocrinol Diabetes* **110**, 113-118 (2002).

193. Deacon, C.F., Johnsen, A.H. & Holst, J.J. Degradation of glucagon-like peptide-1 by human plasma in vitro yields an N-terminally truncated peptide that is a major endogenous metabolite in vivo. *The Journal of clinical endocrinology and metabolism* **80**, 952-957 (1995).

194. Mentlein, R. Proline residues in the maturation and degradation of peptide hormones and neuropeptides. *FEBS letters* **234**, 251-256 (1988).

195. Madsbad, S. Exenatide and liraglutide: different approaches to develop GLP-1 receptor agonists (incretin mimetics)--preclinical and clinical results. *Best practice & research. Clinical endocrinology & metabolism* **23**, 463-477 (2009).

196. Rosenstock, J. et al. Potential of albiglutide, a long-acting GLP-1 receptor agonist, in type 2 diabetes: a randomized controlled trial exploring weekly, biweekly, and monthly dosing. *Diabetes care* **32**, 1880-1886 (2009).

197. Ueda, T. et al. Chemoenzymatic synthesis of glycosylated glucagon-like peptide 1: effect of glycosylation on proteolytic resistance and in vivo blood glucose-lowering activity. *Journal of the American Chemical Society* **131**, 6237-6245 (2009).

198. Turner, A.J., Isaac, R.E. & Coates, D. The neprilysin (NEP) family of zinc metalloendopeptidases: genomics and function. *BioEssays : news and reviews in molecular, cellular and developmental biology* **23**, 261-269 (2001).

199. Gee, N.S., Bowes, M.A., Buck, P. & Kenny, A.J. An immunoradiometric assay for endopeptidase-24.11 shows it to be a widely distributed enzyme in pig tissues. *The Biochemical journal* **228**, 119-126 (1985).

200. Hupe-Sodmann, K. et al. Endoproteolysis of glucagon-like peptide (GLP)-1 (7-36) amide by ectopeptidases in RINm5F cells. *Peptides* **18**, 625-632 (1997).

201. Murage, E.N., Gao, G., Bisello, A. & Ahn, J.M. Development of potent glucagon-like peptide-1 agonists with high enzyme stability via introduction of multiple lactam bridges. *Journal of medicinal chemistry* **53**, 6412-6420 (2010).

202. Liu, H.K. et al. N-acetyl-GLP-1: a DPP IV-resistant analogue of glucagon-like peptide-1 (GLP-1) with improved effects on pancreatic beta-cell-associated gene expression. *Cell biology international* **28**, 69-73 (2004).

203. Sebokova, E. et al. Taspoglutide, an analog of human glucagon-like Peptide-1 with enhanced stability and in vivo potency. *Endocrinology* **151**, 2474-2482 (2010).

204. Adelhorst, K., Hedegaard, B.B., Knudsen, L.B. & Kirk, O. Structure-activity studies of glucagon-like peptide-1. *The Journal of biological chemistry* **269**, 6275-6278 (1994).

205. Wilkinson, M., Jacobson, W. & Wilkinson, D.A. Brain slices in radioligand binding assays: quantification of opiate, benzodiazepines and beta-adrenergic ([3H] CGP-12177) receptors. *Progress in neuro-psychopharmacology & biological psychiatry* **8**, 621-626 (1984).

206. Casal-Dominguez, J.J., Clark, M., Traynor, J.R., Husbands, S.M. & Bailey, S.J. In vivo and in vitro characterization of naltrindole-derived ligands at the kappa-opioid receptor. *Journal of psychopharmacology* **27**, 192-202 (2013).

207. Zhang, X.X. et al. Comparison of F-labeled CXCR4 antagonist peptides for PET imaging of CXCR4 expression. *Molecular imaging and biology : MIB : the official publication of the Academy of Molecular Imaging* (2013).

208. Fernandez-Duenas, V. et al. Dopamine D receptor-mediated modulation of adenosine A receptor agonist binding within the AR/DR oligomer framework. *Neurochemistry international* (2013).

209. Masur, K., Tibaduiza, E.C., Chen, C., Ligon, B. & Beinborn, M. Basal receptor activation by locally produced glucagon-like peptide-1 contributes to maintaining beta-cell function. *Molecular endocrinology* **19**, 1373-1382 (2005).

210. Mann, R.J., Nasr, N.E., Sinfield, J.K., Paci, E. & Donnelly, D. The major determinant of exendin-4/glucagon-like peptide 1 differential affinity at the rat

glucagon-like peptide 1 receptor N-terminal domain is a hydrogen bond from SER-32 of exendin-4. *British journal of pharmacology* **160**, 1973-1984 (2010).

211. Trivedi, D. et al. Design and synthesis of conformationally constrained glucagon analogues. *Journal of medicinal chemistry* **43**, 1714-1722 (2000).

212. Miranda, L.P. et al. Design and synthesis of conformationally constrained glucagon-like peptide-1 derivatives with increased plasma stability and prolonged in vivo activity. *Journal of medicinal chemistry* **51**, 2758-2765 (2008).

213. Syme, C.A., Zhang, L. & Bisello, A. Caveolin-1 regulates cellular trafficking and function of the glucagon-like Peptide 1 receptor. *Molecular endocrinology* **20**, 3400-3411 (2006).

214. Salomon, Y., Londos, C. & Rodbell, M. A highly sensitive adenylate cyclase assay. *Analytical biochemistry* **58**, 541-548 (1974).

215. Deyev, S.M. & Lebedenko, E.N. Multivalency: the hallmark of antibodies used for optimization of tumor targeting by design. *BioEssays : news and reviews in molecular, cellular and developmental biology* **30**, 904-918 (2008).

216. Singh, A.N. et al. Multivalent bifunctional chelator scaffolds for gallium-68 based positron emission tomography imaging probe design: signal amplification via multivalency. *Bioconjugate chemistry* **22**, 1650-1662 (2011).

217. Singh, A.N. et al. Multivalent Bifunctional Chelator Scaffolds for Gallium-68 Based Positron Emission Tomography Imaging Probe Design: Signal Amplification via Multivalency. *Bioconjugate Chemistry* **22**, 1650-1662.

218. Adam-Rebeles, R., Van den Winkel, P. & De Vis, L. Optimization of production yields, radionuclidic purity and hotcell shielding of SPECT and PET radionuclides produced by proton irradiation in variable energy 30 MeV cyclotrons--Part 67Ga. *Applied radiation and isotopes : including data, instrumentation and methods for use in agriculture, industry and medicine* **65**, 995-1013 (2007).

219. Tornesello, A.L. et al. Gastrin and cholecystokinin peptide-based radiopharmaceuticals: an in vivo and in vitro comparison. *Journal of peptide science : an official publication of the European Peptide Society* **17**, 405-412 (2011).

220. Kwekkeboom, D.J. et al. Overview of results of peptide receptor radionuclide therapy with 3 radiolabeled somatostatin analogs. *Journal of nuclear medicine : official publication, Society of Nuclear Medicine* **46 Suppl 1**, 62S-66S (2005).

221. Vegt, E. et al. Renal uptake of radiolabeled octreotide in human subjects is efficiently inhibited by succinylated gelatin. *Journal of nuclear medicine : official publication, Society of Nuclear Medicine* **47**, 432-436 (2006).

222. Behr, T.M. et al. Reduction of the renal uptake of radiolabeled monoclonal antibody fragments by cationic amino acids and their derivatives. *Cancer research* **55**, 3825-3834 (1995).

223. Vegt, E. et al. Reducing renal uptake of radiolabeled peptides using albumin fragments. *Journal of nuclear medicine : official publication, Society of Nuclear Medicine* **49**, 1506-1511 (2008).

224. Gotthardt, M. et al. Indication for different mechanisms of kidney uptake of radiolabeled peptides. *Journal of nuclear medicine : official publication, Society of Nuclear Medicine* **48**, 596-601 (2007).

225. Melis, M. et al. Dose-response effect of Gelofusine on renal uptake and retention of radiolabelled octreotate in rats with CA20948 tumours. *European journal of nuclear medicine and molecular imaging* **36**, 1968-1976 (2009).

226. Zager, R.A. Amino acid hyperalimentation in acute renal failure: a potential therapeutic paradox. *Kidney international. Supplement* **22**, S72-75 (1987).

227. Grimm, J., Potthast, A., Wunder, A. & Moore, A. Magnetic resonance imaging of the pancreas and pancreatic tumors in a mouse orthotopic model of human cancer. *Int J Cancer* **106**, 806-811 (2003).

228. Nachnani, J.S. et al. Biochemical and histological effects of exendin-4 (exenatide) on the rat pancreas. *Diabetologia* **53**, 153-159 (2010).

229. Kendall, D.M. et al. Effects of exenatide (exendin-4) on glycemic control over 30 weeks in patients with type 2 diabetes treated with metformin and a sulfonylurea. *Diabetes care* **28**, 1083-1091 (2005).

230. Dunphy, J.L., Taylor, R.G. & Fuller, P.J. Tissue distribution of rat glucagon receptor and GLP-1 receptor gene expression. *Mol Cell Endocrinol* **141**, 179-186 (1998).

231. Hara, M. et al. Imaging pancreatic beta-cells in the intact pancreas. *American journal of physiology. Endocrinology and metabolism* **290**, E1041-1047 (2006).

232. Dandekar, M., Tseng, J.R. & Gambhir, S.S. Reproducibility of 18F-FDG microPET studies in mouse tumor xenografts. *Journal of nuclear medicine : official publication, Society of Nuclear Medicine* **48**, 602-607 (2007).

233. Kloppel, G., Drenck, C.R., Oberholzer, M. & Heitz, P.U. Morphometric evidence for a striking B-cell reduction at the clinical onset of type 1 diabetes. *Virchows Archiv. A, Pathological anatomy and histopathology* **403**, 441-452 (1984).

234. Lernmark, A. et al. Heterogeneity of islet pathology in two infants with recent onset diabetes mellitus. *Virchows Archiv : an international journal of pathology* **425**, 631-640 (1995).

235. Junker, K., Egeberg, J., Kromann, H. & Nerup, J. An autopsy study of the islets of Langerhans in acute-onset juvenile diabetes mellitus. *Acta pathologica et microbiologica Scandinavica. Section A, Pathology* **85**, 699-706 (1977).

236. Gepts, W. Pathologic anatomy of the pancreas in juvenile diabetes mellitus. *Diabetes* **14**, 619-633 (1965).

237. Sherry, N.A., Tsai, E.B. & Herold, K.C. Natural history of beta-cell function in type 1 diabetes. *Diabetes* **54 Suppl 2**, S32-39 (2005).

238. Prentki, M. & Nolan, C.J. Islet beta cell failure in type 2 diabetes. *The Journal of clinical investigation* **116**, 1802-1812 (2006).

239. Harris, M.I. Epidemiologic studies on the pathogenesis of non-insulin-dependent diabetes mellitus (NIDDM). *Clinical and investigative medicine. Medecine clinique et experimentale* **18**, 231-239 (1995).

240. Chen, C., Hosokawa, H., Bumbalo, L.M. & Leahy, J.L. Mechanism of compensatory hyperinsulinemia in normoglycemic insulin-resistant spontaneously hypertensive rats. Augmented enzymatic activity of glucokinase in beta-cells. *The Journal of clinical investigation* **94**, 399-404 (1994).

241. Srinivasan, S., Bernal-Mizrachi, E., Ohsugi, M. & Permutt, M.A. Glucose promotes pancreatic islet beta-cell survival through a PI 3-kinase/Akt-signaling pathway. *American journal of physiology. Endocrinology and metabolism* **283**, E784-793 (2002).

242. Efrat, S. Prospects for treatment of type 2 diabetes by expansion of the beta-cell mass. *Diabetes* **50 Suppl 1**, S189-190 (2001).

243. Kloppel, G., Lohr, M., Habich, K., Oberholzer, M. & Heitz, P.U. Islet pathology and the pathogenesis of type 1 and type 2 diabetes mellitus revisited. *Survey and synthesis of pathology research* **4**, 110-125 (1985).

244. Yoon, K.H. et al. Selective beta-cell loss and alpha-cell expansion in patients with type 2 diabetes mellitus in Korea. *The Journal of clinical endocrinology and metabolism* **88**, 2300-2308 (2003).

245. Hardy, O.T. et al. Accuracy of [18F]fluorodopa positron emission tomography for diagnosing and localizing focal congenital hyperinsulinism. *J Clin Endocrinol Metab* **92**, 4706-4711 (2007).

246. Schneider, S. et al. In vitro and in vivo evaluation of novel glibenclamide derivatives as imaging agents for the non-invasive assessment of the pancreatic islet cell mass in animals and humans. *Exp Clin Endocrinol Diabetes* **113**, 388-395 (2005).

247. Herrera, P.L., Nepote, V. & Delacour, A. Pancreatic cell lineage analyses in mice. *Endocrine* **19**, 267-278 (2002).

248. Ichise, M. & Harris, P.E. Imaging of beta-cell mass and function. *Journal of nuclear medicine : official publication, Society of Nuclear Medicine* **51**, 1001-1004 (2010).

249. Drucker, D.J. Glucagon-like peptides. *Diabetes* **47**, 159-169 (1998).

250. Wicki, A. et al. [Lys40(Ahx-DTPA-111In)NH2]-Exendin-4 is a highly efficient radiotherapeutic for glucagon-like peptide-1 receptor-targeted therapy for insulinoma. *Clinical cancer research : an official journal of the American Association for Cancer Research* **13**, 3696-3705 (2007).

251. Wild, D. et al. [Lys40(Ahx-DTPA-111In)NH2]exendin-4, a very promising ligand for glucagon-like peptide-1 (GLP-1) receptor targeting. *Journal of nuclear medicine : official publication, Society of Nuclear Medicine* **47**, 2025-2033 (2006).

252. Christ, E. et al. Glucagon-like peptide-1 receptor imaging for localization of insulinomas. *The Journal of clinical endocrinology and metabolism* **94**, 4398-4405 (2009).

253. Waser, B. & Reubi, J.C. Value of the radiolabelled GLP-1 receptor antagonist exendin(9-39) for targeting of GLP-1 receptor-expressing pancreatic tissues in

mice and humans. *European journal of nuclear medicine and molecular imaging* **38**, 1054-1058 (2011).

254.   Mukai, E. et al. GLP-1 receptor antagonist as a potential probe for pancreatic beta-cell imaging. *Biochemical and biophysical research communications* **389**, 523-526 (2009).

255.   Brom, M., Oyen, W.J., Joosten, L., Gotthardt, M. & Boerman, O.C. 68Ga-labelled exendin-3, a new agent for the detection of insulinomas with PET. *European journal of nuclear medicine and molecular imaging* **37**, 1345-1355 (2010).

256.   Young, A.A. et al. Glucose-lowering and insulin-sensitizing actions of exendin-4: studies in obese diabetic (ob/ob, db/db) mice, diabetic fatty Zucker rats, and diabetic rhesus monkeys (Macaca mulatta). *Diabetes* **48**, 1026-1034 (1999).

257.   Thornton, K. & Gorenstein, D.G. Structure of glucagon-like peptide (7-36) amide in a dodecylphosphocholine micelle as determined by 2D NMR. *Biochemistry* **33**, 3532-3539 (1994).

258.   Chang, X., Keller, D., O'Donoghue, S.I. & Led, J.J. NMR studies of the aggregation of glucagon-like peptide-1: formation of a symmetric helical dimer. *FEBS letters* **515**, 165-170 (2002).

259.   De Filippis, V., De Antoni, F., Frigo, M., Polverino de Laureto, P. & Fontana, A. Enhanced Protein Thermostability by Ala --> Aib Replacement. *Biochemistry* **37**, 1686-1696 (1998).

260.   Murage, E.N., Schroeder, J.C., Beinborn, M. & Ahn, J.M. Search for alpha-helical propensity in the receptor-bound conformation of glucagon-like peptide-1. *Bioorg Med Chem* **16**, 10106-10112 (2008).

261.   Kodama, M., Takeshita, F., Kanegasaki, S., Ochiya, T. & Quinn, G. Pancreatic endocrine and exocrine cell ontogeny from renal capsule transplanted embryonic stem cells in streptozocin-injured mice. *The journal of histochemistry and cytochemistry : official journal of the Histochemistry Society* **56**, 33-44 (2008).

262.   Mason, C.C., Hanson, R.L. & Knowler, W.C. Progression to type 2 diabetes characterized by moderate then rapid glucose increases. *Diabetes* **56**, 2054-2061 (2007).

263.   Wang, X. et al. Quantitative analysis of pancreatic polypeptide cell distribution in the human pancreas. *PloS one* **8**, e55501 (2013).

264.   Gan, Z., Ram, S., Ober, R.J. & Ward, E.S. Using multifocal plane microscopy to reveal novel trafficking processes in the recycling pathway. *Journal of cell science* **126**, 1176-1188 (2013).

265.   Li, D. et al. Imaging dynamic insulin release using a fluorescent zinc indicator for monitoring induced exocytotic release (ZIMIR). *Proceedings of the National Academy of Sciences of the United States of America* **108**, 21063-21068 (2011).

266.   Gunn, R.N. et al. A general method to correct PET data for tissue metabolites using a dual-scan approach. *Journal of nuclear medicine : official publication, Society of Nuclear Medicine* **41**, 706-711 (2000).

267. Nakao, R. & Halldin, C. "Mixed" anionic and non-ionic micellar liquid chromatography for high-speed radiometabolite analysis of positron emission tomography radioligands. *Journal of chromatography. A* **1281**, 54-59 (2013).

268. Bi, H. et al. Optimization of harvesting, extraction, and analytical protocols for UPLC-ESI-MS-based metabolomic analysis of adherent mammalian cancer cells. *Analytical and bioanalytical chemistry* **405**, 5279-5289 (2013).

269. Dettmer, K. et al. Metabolite extraction from adherently growing mammalian cells for metabolomics studies: optimization of harvesting and extraction protocols. *Analytical and bioanalytical chemistry* **399**, 1127-1139 (2011).

270. Wang, Z.V. et al. PANIC-ATTAC: a mouse model for inducible and reversible beta-cell ablation. *Diabetes* **57**, 2137-2148 (2008).

271. Muzio, M., Stockwell, B.R., Stennicke, H.R., Salvesen, G.S. & Dixit, V.M. An induced proximity model for caspase-8 activation. *The Journal of biological chemistry* **273**, 2926-2930 (1998).

272. Soret, M., Bacharach, S.L. & Buvat, I. Partial-volume effect in PET tumor imaging. *Journal of nuclear medicine : official publication, Society of Nuclear Medicine* **48**, 932-945 (2007).

273. Mannheim, J.G. et al. Quantification accuracy and partial volume effect in dependence of the attenuation correction of a state-of-the-art small animal PET scanner. *Physics in medicine and biology* **57**, 3981-3993 (2012).

274. Martin, R.J., Gobble, J.L., Hartsock, T.H., Graves, H.B. & Ziegler, J.H. Characterization of an obese syndrome in the pig. *Proceedings of the Society for Experimental Biology and Medicine. Society for Experimental Biology and Medicine* **143**, 198-203 (1973).

275. Dyson, M.C., Alloosh, M., Vuchetich, J.P., Mokelke, E.A. & Sturek, M. Components of metabolic syndrome and coronary artery disease in female Ossabaw swine fed excess atherogenic diet. *Comparative medicine* **56**, 35-45 (2006).

276. Jahan, M. et al. Decreased defluorination using the novel beta-cell imaging agent [18F]FE-DTBZ-d4 in pigs examined by PET. *EJNMMI research* **1**, 33 (2011).

277. Winter, W.E., Harris, N. & Schatz, D. Type 1 diabetes islet autoantibody markers. *Diabetes technology & therapeutics* **4**, 817-839 (2002).

278. Bernard-Kargar, C. & Ktorza, A. Endocrine pancreas plasticity under physiological and pathological conditions. *Diabetes* **50 Suppl 1**, S30-35 (2001).

279. Bock, T., Pakkenberg, B. & Buschard, K. Increased islet volume but unchanged islet number in ob/ob mice. *Diabetes* **52**, 1716-1722 (2003).

280. Bonner-Weir, S. beta-cell turnover: its assessment and implications. *Diabetes* **50 Suppl 1**, S20-24 (2001).

281. Dorrell, C. et al. Isolation of mouse pancreatic alpha, beta, duct and acinar populations with cell surface markers. *Molecular and cellular endocrinology* **339**, 144-150 (2011).

282. Hanley, S.C. et al. {beta}-Cell mass dynamics and islet cell plasticity in human type 2 diabetes. *Endocrinology* **151**, 1462-1472 (2010).

283. Montanya, E., Nacher, V., Biarnes, M. & Soler, J. Linear correlation between beta-cell mass and body weight throughout the lifespan in Lewis rats: role of beta-cell hyperplasia and hypertrophy. *Diabetes* **49**, 1341-1346 (2000).

284. Motyl, K. & McCabe, L.R. Streptozotocin, type I diabetes severity and bone. *Biological procedures online* **11**, 296-315 (2009).

285. Kaiser, E., Colescot, R.l., Bossinge, C.D. & Cook, P.I. Color Test for Detection of Free Terminal Amino Groups in Solid-Phase Synthesis of Peptides. *Anal. Biochem.* **34**, 595-598 (1970).

286. Hancock, W.S., Battersby, J.E. & Harding, D.R.K. Use of Picric Acid as a Simple Monitoring Procedure for Automated Peptide-Synthesis. *Anal Biochem* **69**, 497-503 (1975).

287. Hancock, W.S. & Battersby, J.E. New Micro-Test for Detection of Incomplete Coupling Reactions in Solid-Phase Peptide-Synthesis Using 2,4,6-Trinitrobenzene-Sulphonic Acid. *Anal. Biochem.* **71**, 260-264 (1976).

288. Salomon, Y., Londos, C. & Rodbell, M. Highly Sensitive Adenylate Cyclase Assay. *Anal Biochem* **58**, 541-548 (1974).